Design and Development of a High-Reliability Electronic Power System for Lunar Zebro Rover Operations

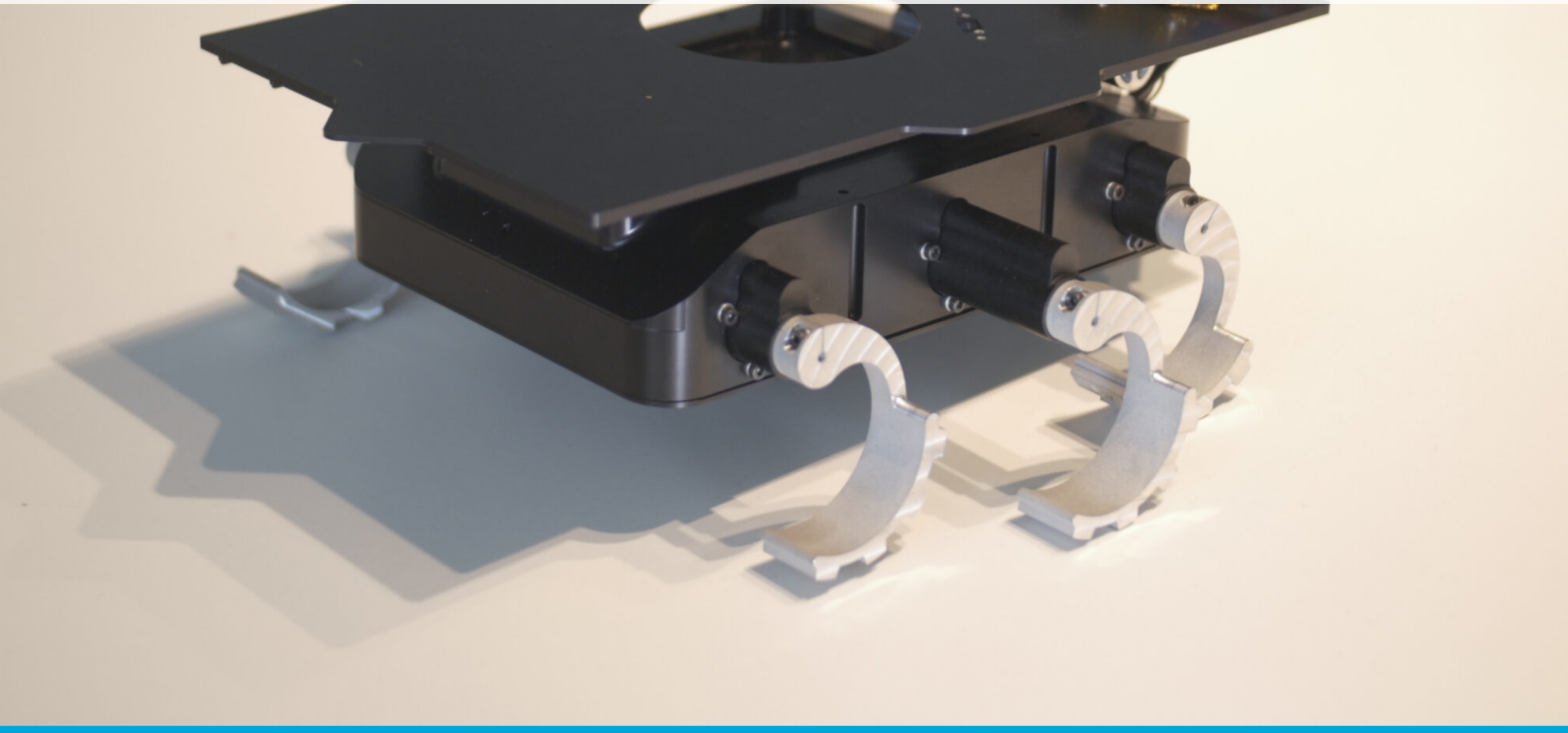

MSc. Thesis
Melle Minten

TU Delft Delft University of Technology

Design and Development of a High-Reliability Electronic Power System for Lunar Zebro Rover Operations

by

Melle Minten

to obtain the degree of
Master of Science
at the Delft University of Technology

to be defended publicly on
Tuesday February 10, 2026
at 01:30 PM

Student number: 4909526
Thesis committee:
Dr.ir. C.J.M. Verhoeven, TU Delft, Chair
Dr.ir. G. Gaydadjiev, TU Delft, Core Member
Dr. A. Noroozi, Advisor

Abstract

The Lunar Zebro team creates a rover that will be deployed on the lunar surface. The rover consists of multiple subsystems, each with its own power requirements. To ensure reliable operation, the rover is equipped with another subsystem, the Electrical Power System (EPS). This system distributes electrical power throughout the rover, continuously monitors the remaining energy stored in the battery pack, and manages the charging and discharging processes. The EPS also consists of a Battery management system (BMS) which monitors the batteries and keep them within a save voltage and current range.

This thesis presents the design, implementation, and validation of a battery management system and battery pack for integration into the Lunar Zebro EPS. A conceptual EPS design with BMS and battery pack is created using energy budget estimation and power modeling. A simulation tool is developed to evaluate the charging and discharging behaviour during walking and charging scenarios of the rover throughout the mission. Based on these simulations, a suitable battery type is selected with focus on temperature tolerance, charging behaviour and reliable operation.

The Battery Management System developed in this work is designed and tested for its protective features, including overvoltage (OV) protection, undervoltage (UV) protection, overcurrent discharge (OCD) protection, and short-circuit discharge (SCD) protection. The BMS operates using I^2C communication with an additional CRC bit to protect against bit errors. This work builds on earlier iterations of the existing EPS.

The BMS is built as a modular unit that can be integrated into the EPS. The bidirectional converter is also taken and redesigned as a separate module to improve accessibility and simplify debugging. This modular design improves development and testing at the cost of reduced compactness.

Finally, the battery pack, the individual cells, and the BMS are tested to gain a clear understanding of the system behaviour in the rover. The results show that the BMS and the battery pack behave well and operate as intended. The integration of the bidirectional converter is shown to work conceptually. Some issues remain in the current physical board, which could not be resolved within the scope of this thesis and are left for future work.

Acknowledgements

This thesis would not have been possible without the support and guidance of many people. I would first like to express my sincere appreciation to my supervisors, Dr.ir. Chris Verhoeven and Dr. Arash Noroozi. They were always approachable, supportive, and willing to think along with me when exploring new ideas or perspectives. Their involvement and guidance were essential throughout the process, and without their input, this thesis would not have progressed to the level it ultimately reached.

I would also like to thank the Lunar Zebro team for providing a welcoming working environment and access to the tools and facilities needed to carry out this research. In particular, I would like to thank the chief engineer, Dani van den Akker, who was always quick to help when I needed to locate data or files. I am also grateful to Dr.ir. Aditya Shekhar for his help in understanding and iterating on the design of the existing EPS. Furthermore, I would like to thank Dr.ir. Georgi Gaydadjiev for being a member of my thesis committee.

Finally, I would like to thank my roommates, Chris Haaring and Demi Schrauwen, for their support during this period. They cooked many much-needed dinners while I was still working in the labs and helped create moments of relaxation, most notably during our now well-known movie nights with friends. The fact that time seemed to pass so quickly while working on this thesis is a clear sign of how much I enjoyed the process.

Melle Minten
Delft, The Netherlands
04/02/2026

Contents

List of Figures

List of Tables

List of Abbreviations

ADC	Analog-to-Digital Converter
BMS	Battery Management System
CCM	Continuous Conduction Mode
CRC	Cyclic Redundancy Check
DC/DC	Direct Current to Direct Current Converter
ECC	Error-Correcting Code
EPS	Electrical Power System
HAL	Hardware Abstraction Layer
I2C	Inter-Integrated Circuit
IV	Current-Voltage
MPP	Maximum Power Point
MPPT	Maximum Power Point Tracking
OV	Overvoltage
PCB	Printed Circuit Board
PWM	Pulse Width Modulation
SOC	State of Charge
SOH	State of Health
SCD	Short Circuit Detection
SPPT	Selective Power Point Tracking
OCD	Overcurrent Detection
TCS	Thermal Control System
UV	Undervoltage
UART	Universal Asynchronous Receiver-Transmitter

Chapter 1

Introduction and Background

1.1 Background on lunar rovers and Lunar Zebro

In recent years, international attention to the Moon has increased. The Chang'e 6, developed by the Chinese National Space Agency (CNSA) in 2024, brought the first samples from the far side of the Moon to Earth [11]. This mission demonstrates that the international space race is ongoing and that the Moon remains as fascinating as ever. Likewise, NASA is working on its Artemis programme [15], which once again demonstrates the relevance of the Moon.

As the Chang'e 6 mission shows, not all Moon missions need to be done by humans. Robots can go to the Moon collecting data instead of astronauts. An advantage of sending a robot to the Moon is that it can take more risks. Still, losing a robot by driving it too far into a cave or crater would be very expensive and could delay scientific data collection. For example, while navigating Mars, the Spirit Rover ended its mission in loose soil, where it got stuck [9]. Although its operators constantly made educated choices about whether to proceed or which path to take, this minimized the risks of losing the rover.

Lunar Zebro could be a solution for this. Lunar Zebro aims to develop multiple, cheaper, and smaller rovers that can be deployed simultaneously. An advantage of having more rovers is that these simple robots can work together to perform a complicated task [21]. Having more, smaller rovers also means that individual rovers can take more risks, so more inaccessible places on outer planets and moons can be explored. There are even possibilities that when a rover gets stuck, other rovers might be able to help. Working as a swarm instead of individually has positive effects for every individual. Furthermore, the Lunar Zebro rovers will be designed to be modular, so different rovers can carry different tools or instruments with them.

1.2 Mission context and challenges

Mission statement: The long-term vision of the project is to provide infrastructure and a means of exploration, implementing a self-repairing swarm and scalable, adaptable, and disposable agents. This vision is defined by the Lunar Zebro management.

First Mission Statement: To realize a Lunar rover mission that survives, communicates, senses the radiation environment, navigates semi-autonomously, and captures images to support Lunar exploration.

1.3 Lunar environment

For this thesis, it is suitable to introduce the lunar environment that influences the design of the Lunar Zebro rover. The surface of the Moon has harsher and different conditions compared to the Earth's surface. First, the Moon's gravity is weaker than that of Earth [17]. The gravity of the Moon is only one-sixth of Earth's gravity. This influences some of the mechanical systems of the rover, especially

walking. A more significant impact is the absence of a true atmosphere [17]. The Moon has an exosphere; this layer around the Moon is extremely thin. This exosphere does not protect the surface from cosmic and solar radiation as the Earth's atmosphere does. Particles from outer space can cause damage to the rover, resulting in failures in sensitive digital subsystems.

Another harsh environmental factor is the large temperature differences on the Moon. During the lunar day, the surface can reach around 127°C, while at night it can fall to approximately −173°C [17]. Near the poles, in some permanently shadowed craters, temperatures can even drop down to −240°C. The lunar environment creates major challenges to design for. During this thesis, some tests are defined but not executed due to the required equipment not being available in the laboratory.

1.4 Problem statement and Research questions

The Lunar Zebro Team develops the Lunar Rover at Delft University of Technology. The team consists of 37 members, supported by a large group of alumni. The team structure organizes the team members over several departments. The contents of this thesis are part of the electronics department, which is responsible for the development of all electronic subsystems. Subsystems that fall under this department are, for example, motor control, sensors, and power electronics. Within these subsystems, the electrical power system (EPS) plays a critical role, as it is responsible for the power of the rover. The EPS must ensure that energy is stored, managed, and delivered in a safe way. Building on previous work within the team, there is an existing EPS for the rover, but this lacks a dedicated battery management system (BMS) and a validated battery pack. A battery management system is essential to protect the battery pack against potentially mission-ending faults such as overvoltage, undervoltage, and overcurrent conditions. These faults cannot be mitigated once the rover is deployed on the Moon, making robust protection mechanisms mandatory. The focus of this thesis is therefore to design a reliable BMS with a validated battery pack that can be modularly integrated into the Lunar Zebro electrical power system and to verify this design using a prototype. This leads to the first research question:

1. How can a reliable battery management system be designed and validated for the Lunar Zebro rover operating in the lunar environment?

In addition to the BMS, the battery cells themselves need to be investigated, as they must show predictable behavior and survive the entire mission. The cells exhibit long-term behavior that depends on the applied charging and discharging currents. To understand what can be expected from the battery pack during the mission, a complete picture of the cell behavior needs to be established. To increase the activity of the rover during the first mission, charging currents exceeding the manufacturer's recommendations are also investigated. This introduces a trade-off between charging speed and battery lifetime, which must be evaluated. This results in the second research question:

2. How does the battery pack behave under different operating conditions over the full duration of the first Lunar Zebro mission?

To integrate the newly designed BMS and battery pack, modifications to the existing EPS are required. Parts of the EPS are therefore redesigned, including the bidirectional converter, resulting in a more modular and extensible power architecture. This leads to the third research question:

3. How can the newly designed BMS and validated battery pack be integrated into the existing EPS of the Lunar Zebro rover?

This thesis focuses on the design, implementation, and validation of the battery management system and battery pack, as well as their integration into the EPS. Mechanical design, navigation, and higher-level mission planning are outside the scope of this work.

Chapter 2

System Requirements and Constraints

This chapter defines the system requirements and constraints for the Electrical Power System (EPS) of the Lunar Zebro rover. It describes the functional requirements and provides an overview of the system architecture, followed by subsystem-specific requirements for the batteries, battery management system, microcontroller, solar panels, and power converters. These requirements form the basis for the design and evaluation of the EPS presented in the following chapters.

2.1 Functional Requirements

When designing the Electrical Power System (EPS) of the rover, some system engineering is required. To make unambiguous and testable statements, the Requirements specification writing is used.

1. The EPS shall monitor the State of Health (SOH) and State of Charge (SOC) of each cell.
2. The EPS shall perform cell balancing to maintain voltage uniformity among cells.
3. The EPS shall withstand the temperature difference in outer space.
4. The EPS shall withstand the radiation in outer space [3].
5. The EPS shall provide enough power to let the rover walk.
6. The EPS shall charge the battery pack from the 12V bus.
7. The EPS shall discharge the battery pack to supply voltage on the 12V bus.
8. The EPS shall provide 12V, 5V and 3.3V to the other subsystems.

2.2 Systems Overview

The current Electrical Power System (EPS) is based on the design developed by Hubers et al. [5]. Figure 2.1 shows the new system overview. In this version, a Battery Management System (BMS) is connected between the battery pack and the bidirectional converter. The BMS protects the batteries electrically and monitors important parameters such as the State of Health (SOH), State of Charge (SOC), and temperature. It also prevents short circuits, reverse polarity, and over- or undercharging.

The BMS communicates with a microcontroller through an I^2C connection. The microcontroller collects data and sends control commands to the BMS, for example, to enable charging or discharging. In the test setup, this microcontroller is connected to a computer via UART for debugging and data logging. On the rover. In the final design of the rover, it will most likely be connected to the main motherboard.

The battery pack delivers a voltage that varies depending on its charge level. To provide a stable power output, a bidirectional DC/DC converter regulates this to a constant 12 V bus. From there, the setup is largely the same as in the previous design. The 12 V bus feeds several smaller DC/DC converters, which supply the required voltages to other subsystems. A dedicated boost converter is also included to handle the input from the solar panels. The next sections describe the different parts of the system in more detail. Note that these are the requirements for the final mission. The design philosophy is that first the system should be working, and then be made suitable for the Lunar surface. This approach is taken because the system is first developed under limited resources and constraints. Otherwise, the costs will greatly increase without knowing if the design is functional. For that reason, in this thesis, not all requirements are met yet, the goal is to make it functional with as many mitigations taken within the budget and time.

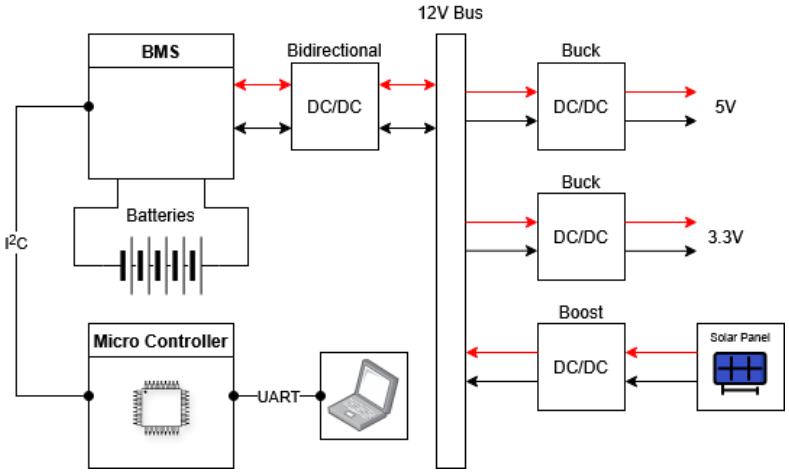

Figure 2.1: Electrical Power System (EPS) overview based on the previously designed power bus.

2.3 Environmental and Operational Requirements

2.3.1 Batteries

The batteries form the primary energy storage unit of the rover's Electrical Power System (EPS). Their main function is to hold power that is retrieved by the solar panels and provide this to all other subsystems of the rover. To meet the mission objectives, the batteries must satisfy specific requirements.

1. **The batteries shall be able to operate in the extreme temperatures in the rover.** According to the TCS department, the maximum and minimum temperature difference within the rover is $-40°C$ up to $80°C$. The batteries should be capable of handling this.

2. **The batteries shall be able to be repeatedly charged and discharged for one lunar day.** The current mission is for the rover to survive one lunar day, approximately 14 Earth days. The batteries should keep the rover functional for this period.

3. **The batteries shall deliver peak discharge currents so that the rover can walk using its motors.** All systems on the rover are estimated not to have high peak currents, except for the motors driving the legs of the rover.

2.3.2 Battery Management System

The Battery Management System (BMS) is responsible for ensuring that the batteries are used safely and reliably. The BMS monitors each cell, charges and discharges the batteries controlled and protects the pack with several safety measures.

1. **The BMS shall monitor the pack and individual cell voltages**.

2. **The BMS shall implement hardware protection features**, like overcurrent protection, short circuit protection, overvoltage (OV) and undervoltage (UV).

3. **The BMS shall provide integrated cell balancing**, this is because individual cells can be overcharged when stacked in a pack due to the slight differences in capacity, internal resistance, or chemistry.

4. **The BMS shall provide alert and communication features**, data should be monitored by an onboard microcontroller. The BMS and microcontroller should be able to communicate.

2.3.3 Microcontroller

The microcontroller is the thinking part of the EPS. Where the BMS gathers data, the microcontroller processes it. The requirements for the microcontroller are:

1. **The microcontroller shall be able to operate in the extreme temperatures in the rover.** Like the other blocks, the microcontroller should handle the temperature differences from $-40°C$ up to $80°C$.

2. **The microcontroller shall be able to communicate with the BMS.** This is to send and retrieve data.

2.3.4 Solar Panel

The solar panel is already chosen for the project. The panels that are going to be used are the TJ Solar Cell 3G30A [2]. The requirements for the solar panel are:

1. **The solar panel shall withstand the harsh environment of the moon.** The panel should withstand radiation, great temperature differences, vacuum and the dust on the moon.

2. **The solar panel shall provide enough power to charge the batteries at maximum charging power.**

2.3.5 DC/DC Converters

There are several DC/DC converters used in the original design. This design was earlier designed and built by Hubers et al. [5]. As said before, the newly designed BMS is connected between the bidirectional converter and the batteries. The requirements for the bidirectional converter are:

1. **The bidirectional converter shall withstand the harsh environment of the moon.** The bidirectional converter should withstand radiation, great temperature differences and vacuum.

2. **The bidirectional converter shall convert the fluctuating voltages of the battery to a steady 12V output.**

3. **The bidirectional converter shall power the batteries.** When excess power is on the 12V bus due to solar power, the bidirectional converter would change from providing power to consuming power from the 12V bus, to charge the battery.

Another DC/DC converter used it the boost converter from the solar panel. The requirements for this converter are:

1. **The boost converter shall withstand the harsh environment of the moon.** The bidirectional converter should withstand radiation, great temperature differences and vacuum.

2. **The boost converter shall convert the fluctuating voltages of the solar panel to a steady 12V output.**

The last two converters in the design are the two buck converters. These converters are responsible to step down the 12v to 5V and 3.3V. The requirements for these converters are:

1. **The buck converters shall withstand the harsh environment of the moon.** The bidirectional converter should withstand radiation, great temperature differences and vacuum.

As said before, these connectors are previously designed. However, the existing design may require minor adjustments to ensure proper integration with the newly incorporated battery management system (BMS).

Chapter 3

Conceptional Design and System Dimensioning

At the current state of the project, many on-board systems are not yet finished or fully worked out. As a result, many boundaries of the project are still unknown. Parameters such as peak power consumption, total energy budget and available space for the battery cells are not yet defined. In this chapter, a first rough design of the Electrical Power System (EPS) is established. These first-order choices are needed to assess whether the system is feasible at all. From this initial design, other concepts can be explored and more detailed design choices can be made in later stages of the project. This chapter focuses on establishing initial values and making early design decisions. The emphasis lies on determining orders of magnitude rather than exact values, providing a foundation for component selection and overall system architecture.

3.1 Energy Budget Estimation

One of the most important parameters is the Energy budget of the rover. This is because the energy budget drives constraints to the rest of the design. Establishing the energy budget is crucial for the design of the battery pack and BMS. The power consumption of the rover is unknown, as it is not yet fully operational. The power consumption of some systems can be roughly established. This is because some subsystems have a significantly higher power consumption than that of other subsystems. It can be said that most likely the majority of the system's power is consumed by the motors. This is evident from the fact that motor power requirements are in the watt range, while the other electronic subsystems (such as sensors and controllers) typically consume only milliwatts or less. Reasoning like this can help to determine the order of magnitude of most of the subsystems.

3.2 Motor Power Estimation

The exact power consumption of the motors is unknown, but can be estimated from the datasheet [1] for the 170 RPM Econ Gear Motor. With the rover mass of 2.5 kg, rover legs of around 7 cm, the torque stall of 22.04 kgf-cm and current stall at 3.8 A, the power can be calculated by first determining the gravitational force of the rover.

$$F_{g,rover} = m \cdot g = 2.5 \times 9.81 = 24.525 \text{ N} \tag{3.1}$$

Note that Earth's gravitational acceleration (g) is used, as the rover is expected to perform the same manoeuvres on Earth, during testing, as it will on the Moon. Then the torque stall is converted to $N \cdot m$.

$$\tau_{\text{stall}} = 22.04 \text{ kgf·cm} \tag{3.2}$$

$$1 \text{ kgf·cm} = 0.0981 \text{ N·m} \tag{3.3}$$

$$\tau_{\text{stall}} = 22.04 \times 0.0981 = 2.16 \text{ N·m} \tag{3.4}$$

Then, with the converted torque value, the torque constant formula is used. which results in 1 A of current drawn.

$$K_t = \frac{\tau_{\text{stall}}}{I_{\text{stall}}} = \frac{2.16}{3.8} = 0.568 \ \frac{\text{N·m}}{\text{A}} \tag{3.5}$$

$$\tau_{\text{totaal}} = \frac{F \cdot r}{\#_{\text{motors}}} \ = \ \frac{24.525 \times 0.07}{3} \ = \ 0.572\text{N} \cdot \text{m}. \tag{3.6}$$

$$I = \frac{\tau}{K_T} = \frac{0.572}{0.568} = 1.0\text{A} \tag{3.7}$$

With 1A of current, it can be established that 12 W of power is used per motor. This value is established based on the locomotion principle of the rover, three out of the six motors are active at any given time during walking. Considering this operational mode and the requirement for the rover to sustain continuous walking for several minutes, the first set of power and energy requirements can be established and the first steps of the energy budget of the rover can be made.

3.3 PV Panel Selection

As previously mentioned, the solar panels used for the rover have been predetermined. The chosen panels are the TJ Solar Cell 3G30A [2]. Each PV panel exhibits a characteristic current-voltage (IV) curve, meaning that for each voltage level, only a specific maximum current can be supplied. Consequently, there exists a unique voltage-current combination at which the panel delivers its highest possible power output, referred to as the maximum power point (MPP).

From the datasheet of the TJ Solar Cell 3G30A [2], it is possible to extract the values for this point. The maximum voltage, V_{mpp}, and maximum current, I_{mpp}, are listed as 2.5 V and 0.5 A, respectively. Using these values, the maximum power output of a single panel can be calculated as follows:

$$P_{\text{mpp}} = V_{\text{mpp}} \cdot I_{\text{mpp}} = 2.5 \times 0.5 = 1.25 \text{ W}. \tag{3.8}$$

This value represents the peak power that each panel can deliver under ideal conditions. In the context of the rover's energy system, this information provides a first-order estimate of the total power that can be provided by the solar panels.

3.4 Battery Selection

Commercially available batteries are used in this project. Developing in-house battery cells is beyond the scope of the work, and several studies [12] [24] show that battery technology is rapidly improving in terms of energy density, cycle life, and cost. This supports the decision to use state-of-the-art commercial cells rather than designing our own. A few batteries were considered during the selection process: Nitecore's NL1835LTHP cells, several TADIRAN models, and the INR21700M50T, which has already been used in previous Lunar Zebro projects.

The INR21700M50T batteries may outperform the other candidates in terms of energy density and discharge capability, but they do not offer a significant advantage overall. The Tadiran and Nitecore cells are designed to handle more extreme temperature variations. Since temperature tolerance is a key requirement for lunar operations, this factor has a major impact on system reliability. Therefore, if the rover can still meet its performance requirements using the more temperature-resistant options, batteries from one of these suppliers are likely the better choice.

3.5 Microcontroller Selection

For the EPS a microcontroller is needed, which gathers data from the BMS and the bidirectional converter. Based on the collected data, the microcontroller is programmed to make decisions so that the EPS remains functional and stable. Many different microcontrollers could be suitable for this project. In this work, discussed with the thesis supervisors, controllers with existing development experience were considered.

ESP32 First, the ESP32-series came to mind. However, after doing some research, the ESP32 is not suited for space. The ESP32 is treated more as an advanced hobby microcontroller than a serious candidate for space. No suitable reports or papers have been written on the behaviour of the ESP32 in space. It can be concluded that the ESP32 is not a good candidate.

STM32H7-series The STM32H7 is promising. Several reports have been written on its behavior in space. The Open Source Satellite performed a radiation test [13], with positive results. The radiation mitigation is not in its external design, but it uses Error-Correcting Code (ECC) memory. This means that when a bit is flipped unintentionally, this can be observed by the use of a correction bit. The data can then be restored. The STM32H7 is a well-capable microcontroller; it maybe even be overqualified for the ESP task.

STM32F4-series The STM32F4 also proves to be worthy of space missions. Many CubeSat projects [4] [14] use the STM32F4 chip as their controller. The difference with the STM32H7 is that the STM32F4 is more suited for simpler tasks. Whether the EPS project of the lunar zebro is simple enough has yet to be determined.

The first design of the EPS will be implemented using an STM32F4 microcontroller. If this controller proves to be insufficient, an upgrade to the STM32H7 can be made with minimal changes. For this reason, STM32F4 Nucleo boards are used [19], allowing the microcontroller to remain modular and easily replaceable, with the flexibility to change pin assignments if needed.

3.6 Battery Management System Architecture

The Battery Management System (BMS) of the rover could be designed in several ways. For many reasons, it was decided to use BQ7692003PW [7]. First, this chip suits the characteristics of the battery that is used and has a lot of built-in mitigations for some of the established requirements. Due to its coulomb counting, the SOH and the SOC can be determined. The second reason is that it communicates over I^2C, which is a widely used protocol that the microcontroller understands. The BQ7692003PW communicates with an extra CRC Byte, which will prevent bit errors if one were to unintentionally flip. A third reason is that the BQ7692003PW is rated for tempratures ranging from -40 °C up to 85 °C. With is within the range established by the Temperature Control System (TCS) department of Lunar Zebro.

The first BMS is made as a prototype board. In the final setup, the BQ7692003PW chip should be connected on board with a microprocessor, the stm32 chip. To easily be able to debug the chip, it is not placed on the same PCB board as the microcontroller. The prototype is kept modular. A big advantage of this setup is that in the case of a misstep, only part of the project needs to be resoldered or redesigned instead of the whole project. Another reason to make it modular is that it is easier to detach and attach certain parts to one another for debugging. The datasheet of the BQ7692003PW presents a proposed system architecture around the chip. This architecture is closely followed and adapted where needed.

3.7 Voltage Bus Architecture

In the article of Hubers et al. a power bus is designed [5] for the Lunar Zebro Rover. Two different system configurations were analyzed. One uses a 12 V bus and one uses a 24 V bus. The author

concludes that the 12 V setup is preferable, because operating the DC/DC converters with a 12 V bus results in lower total power losses compared to the 24 V configuration. Specifically, when the converters operate in Continuous Conduction Mode (CCM), the 12 V bus consistently achieves higher efficiency. Additionally, the average power loss over a full operational cycle of the rover is lower for the 12 V bus (1.47 W) than for the 24 V bus (1.50 W), which directly translates to improved overall energy efficiency and longer rover operation time. For these reasons, the paper concludes that the 12 V bus configuration is the optimal choice for the Lunar Zebro rover's power electronic system.

In the work of Hubers [6], a complete EPS bus for the Lunar Zebro rover was designed and implemented. However, similar to most first iterations, the initial version was not fully finalized. This thesis builds upon many of the concepts and design choices presented by Hubers, using them as a foundation to further refine and develop the EPS for the current project. The fully developed PCB of Hubers' EPS design serves as a starting point. From here, the BMS and batterypack is added to the whole EPS.

3.8 Bidirectional Converter Architecture

The bidirectional converter implemented in this project is based on the design by Hubers [6]. Hubers' design provides a compact and efficient power bus. However, it was not intended to be modular or easily integrated with other subsystems. The original PCB lacks debug interfaces and is highly condensed, which complicates the connection of additional components such as the BMS and battery pack.

Given the scope of this thesis, which focuses on battery research and the BMS, it was decided to isolate and adapt only the bidirectional converter from Hubers' design. This approach allows testing and verification of the converter before future integration with the complete EPS. While the full system integration could not be finalized within the timeframe of this work, adapting the bidirectional converter provides a practical basis for subsequent integration and system expansion.

The architecture of the bidirectional converter is based on Hubers' compact PCB, which is fully extracted and adapted to create a modular board. Several modifications are made to separate the converter from the original dense layout and ensure proper operation as an independent component. With the battery pack, BMS and bidirectional converter all implemented as modular subsystems, the system safely charges and discharges the battery pack while maintaining a stable 12 V bus through the bidirectional converter.

Chapter 4

Design Validation and Simulation

In this chapter, the preliminary system design presented in Chapter 3 is further developed and refined. The main objective is to validate the design and assess its overall feasibility. A particular focus is placed on evaluating the energy feasibility of the system, which is one of the most critical and complex aspects to verify. To do this, simulations are created based on the rough values determined in the previous chapter. These initial estimates serve as a starting point to explore whether the selected components can work together to make the rover operate as intended.

4.1 Power and Energie Budget Simulator

One of the main challenges in validating the system design is ensuring that the rover has sufficient energy to operate all of its subsystems. While the EPS, BMS and batteries form the core of the power system, the rover also includes several additional subsystems that are still under development. Even though these components are not yet finalized, their expected power demands must be accounted for when assessing the overall feasibility of the design.

To address this, a dedicated power budget simulator was developed. This Python-based tool models the energy behavior of the rover by combining the characteristics of the battery pack with the expected power consumption of all subsystems. It evaluates how long the rover can operate, how long it takes to recharge, and how individual components contribute to the energy budget. Beyond verifying current designs, the simulator also provides a flexible framework for testing how adding new systems affects the rover's overall energy performance. The tool can be used by other members of the Lunar Zebro team to see the impact of their subsystem on the whole energy budget. A screenshot of the tool can be seen in Figure 4.1.

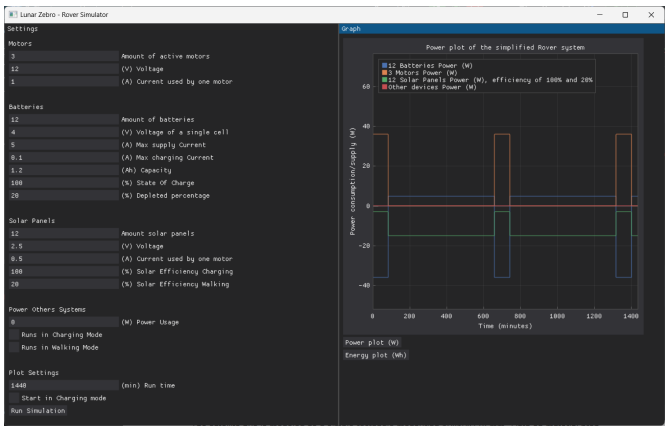

Figure 4.1: Software developed in this thesis and currently used by the team to simulate the rover energy budget.

The simulator takes datasheet values of the components planned for the rover as input and calculates the energy budget for both charging and discharging phases. The output is presented in two complementary plots: the first shows, in detail, which components consume or supply power during each phase, while the second illustrates the total energy consumption/delivery of individual subsystems over time.

Together, these visualizations provide a clear representation of system behavior and allow the evaluation of the charge-to-walk ratio. For the example shown in Figures 4.2a and 4.2b, the rover can walk for 83 minutes, while a full recharge takes 576 minutes. This results in a charge-to-walk ratio of approximately 6.94:1, meaning that for approximately every minute of walking, seven minutes of charging is required. By adjusting design parameters within the simulator, desired charge-to-walk ratios can be explored and optimized to guide system-level decisions.

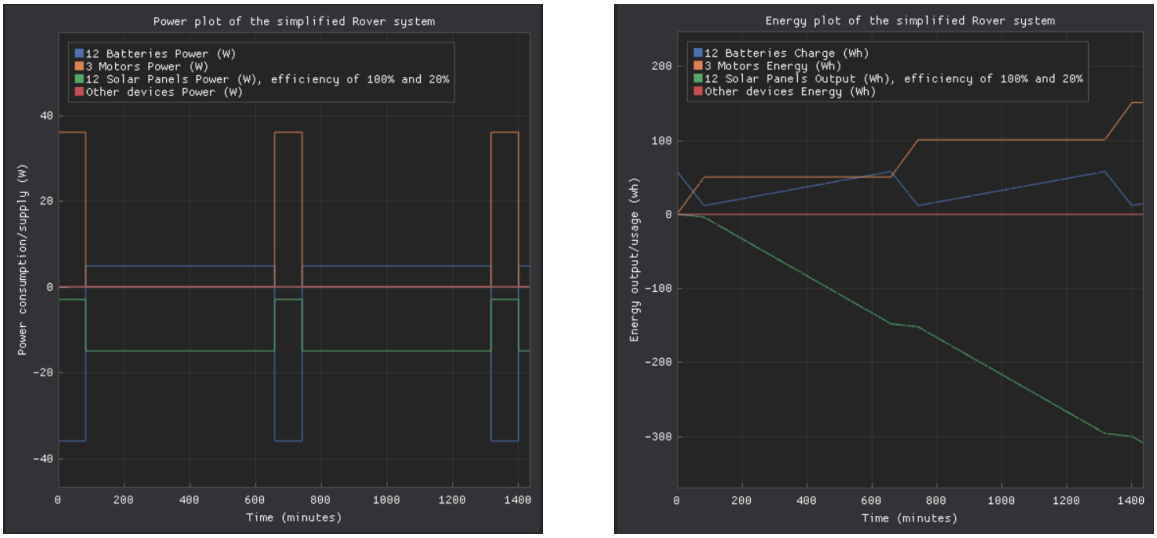

(a) (b)

Figure 4.2: (a.) Simulation showing which components consume or deliver power during each phase. (b.) Simulation illustrating the energy consumption and energy delivery of individual rover subsystems.

The program is written in Python and maintained in the Lunar Zebro team Git repository. This ensures that newly designed components can be added easily, allowing the energy budget to be continuously updated. As the design evolves, the simulator provides an increasingly accurate overview of the rover's power and energy behavior, supporting informed design decisions throughout the project.

4.2 Battery Definitive Selection

The solar panels and motors have already been predetermined, as discussed in Chapter 3. However, the battery selection has not yet been finalized, since the overall power budget of the rover is still uncertain. Once the power budget has been estimated, suitable battery options can be selected accordingly. The selection process was carried out by modeling the different batteries in a simple virtual rover. The modeling and simulation framework developed in Chapter 3 was used to evaluate several commercially available battery options.

From here, the Nitecore batteries and the Tadiran batteries were a suitable option. However, the Nitecore cells were not considered a valid option, as the manufacturer does not provide a detailed datasheet to support the claimed extreme-temperature performance and their power at these temperatures. The Tadiran batteries are supported by a more detailed datasheet [20]. Several different battery options were simulated, of which the TLI1550ES was selected. This choice was made because these cells provide the highest capacity while remaining relatively compact. Another important parameter is that these cells allow for comparatively high charging currents. The importance of this characteristic is discussed

in more detail in the previous Section 4.1.

In addition to standard batteries, another alternative was briefly considered: the use of supercapacitors. Supercapacitors can deliver very high currents over short periods, making them suitable for situations that require quick bursts of power. The original idea was to use them as an auxiliary energy source. The capacitors would slowly charge and then provide an additional power boost during the rover's walking phases.

However, after simulation and analysis, this approach turned out to be unnecessary. The results showed that battery discharge capability was not the main limitation in the rover's operation. Instead, the real constraint lies in the available charging time and the amount of energy that can be replenished during idle phases. Since supercapacitors do not solve this problem, their inclusion would only add extra complexity and mass without offering a clear performance benefit.

With the power and energy budget simulator discussed in Section 4.1, the different batteries from Tadiran can be simulated in combination with the PV panel and the motors. In this section, only the power plots are shown. In Appendix A.1, the corresponding energy plots can be seen. The batteries considered for the rover are:

- TLI-1550ES
- TLI-1550A
- TLI-1550HT
- TLI-1530A
- TLI-1520A
- TLI-1020A

The first battery considered is the TLI-1550ES. This battery seems the most promising due to its having the highest capacity and charging current of all batteries in the list. The result is that for every minute of walking, five and a half minutes of charging is required. Due to the high capacitance of cells, long charge cycles and discharge cycles are possible, see Figure 4.3a. In comparison with the other evaluated cells, this cell demonstrates superior performance and therefore stands out as the best selection.

The TLI-1550A and TLI-1550HT the have similar specs except for the capacity. As a result, its charge-to-walk ratio is nearly identical. However, the reduced capacity offers no additional advantages and may ultimately constrain the system's performance. Figure 4.3b shows the power plot of the TLI-1550A and Figure 4.4a the TLI-1550HT plot.

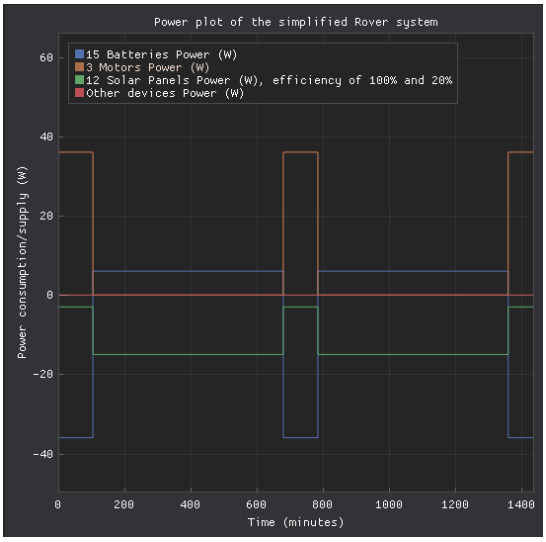

(a)

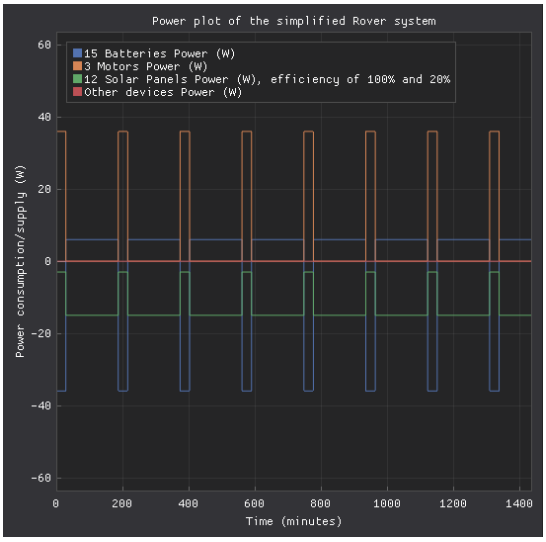

(b)

Figure 4.3: (a.) 15 TLI-1550ES batteries in the power budget simulator showing a charge-to-walk ratio of 5.50 minutes to 1 minute. (b.) 15 TLI-1550A batteries in the power budget simulator showing a charge-to-walk ratio of 5.50 minutes to 1 minute.

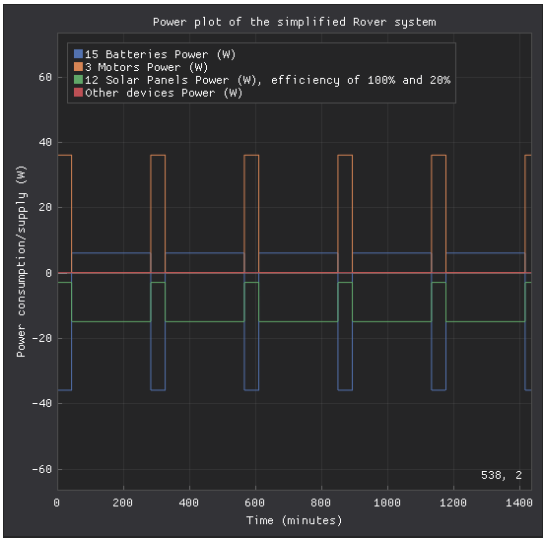

(a)

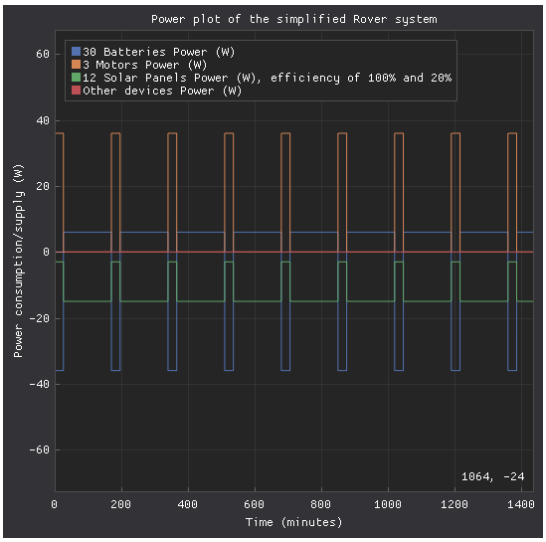

(b)

Figure 4.4: (a.) 15 TLI-1550HT batteries in the power budget simulator showing a charge-to-walk ratio of 5.50 minutes to 1 minute. (b.) 30 TLI-1530A batteries in the power budget simulator showing a charge-to-walk ratio of 5.50 minutes to 1 minute.

The TLI-1530A are smaller than an AA size battery. These batteries are a little bit higher than half a TLI-1550ES battery. Therefore this time instead of 15 cells 30 cells are used in the design. The charge-to-walk ratio keeps therefor very similar. However due to the batteries a little bit bigger than half a aa battery these cells take in more room on the rover, without an improvement in capacity or charge-to-walk ratio. Figure 4.4b shows the power simulated behaviour.

Then the TLI-1520 is considered. In figure 4.5a it can be seen that the charge-to-walk ratio is performing better than the TLI-1550ES. However it can be seen that the powerdensity of these cells is significantly lower than that of the TLI-1550ES. Therefor it decided that the small improvement of charge-to-walk does not weigh against the loss of capacity.

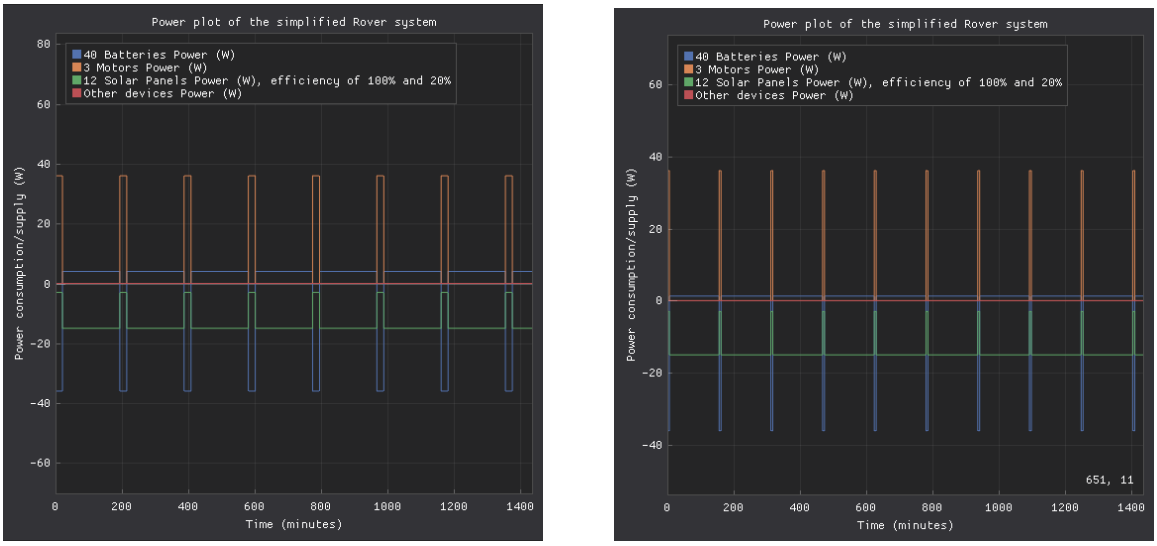

(a) (b)

Figure 4.5: (a.) 40 TLI-1550A batteries in the power budget simulator showing a charge-to-walk ratio of 4.12 minutes to 1 minute. (b.) 40 TLI-1020A batteries in the power budget simulator showing a charge-to-walk ratio of 25.93 minutes to 1 minute.

In figure 4.5b, the TLI-1020A series can be seen. The specs of this battery can be read from the Tadiran datasheet [20]. The TLI-1020A is one of the smallest rechargeable batteries that Tadiran delivers. This comes at a cost of low capacitance and even a lower charging current of 8mA. In Figure 4.5b, it can be seen that 40 of these cells still charge 150.4 minutes for a 5.8-minute walk. the limited factor is the amount of charging current allowed. Compensating for its size with more batteries than using a bigger battery does not compensate enough to make up for the low charging currents.

In all simulations there are some standard values, The motors draw 1 W of power and the solar panels proved 1.25W of power. These values were already established in Chapter 3. Now with the batteries known the conceptional design is finished and can worked further out in detail.

Chapter 5

Detailed System Design and Manufacturing

In this chapter, the detailed design of the Electrical Power System is presented. Building on the conceptual design established earlier, the development is worked out step by step. The chapter begins with the in-depth design of the battery management system, followed by a detailed examination of the bidirectional converter. After this, the integration of these subsystems into the existing power bus is discussed. The chapter concludes with an overview of the manufacturing process of the designed PCBs.

5.1 BMS Implementation

5.1.1 I^2C

The protocol that is used to communicate between the chip and the microcontroller is I^2C. Most I^2C protocols are plug and play. However, the BQ7692003PW chip does not start up its I^2C protocol immediately. The BQ7692003PW has different modes. The chip starts up in ship mode. This is a low-powered state. In this state the the I^2C is turned off. After turning the chip to normal mode, the connection could be established. According to the Datasheet [7]. The following registers have the following information.

Function	**Registers (Hex)**	**Description / Formula**
System Status	0x00	Fault flags (UV, OV, OCD, SCD, etc.)
Cell Balancing Control	0x01	Bitmask for enabling balance on each cell
System Control 1, System Control 2	0x04–0x05	Configurable flags to control the IC, allow charging/discharging, shut down, sleep
Protection Config	0x06–0x08	Configures the SCD/OCD delay & thresholds, UV/OV delays
Thresholds	0x09–0x0A	OV_TRIP, UV_TRIP settings
Coulomb Counter Config	0x0B	Must be set to 0x19 for normal operation
Cell Voltage Reading	0x0C–0x15	The cell voltages of individual cells can be read from these registers.
Battery Voltage and Temperature Data	0x2A–0x2D	The voltage of the battery and the battery temperature.
Coulomb Counting	0x32–0x33	The Coulomb counting data.
ADC Offset, ADC Gain	0x50–0x51, 0x59	The per-chip unique offset and gain of the ADC.

Table 5.1: Summary of BQ76920 Control and Configuration Registers

5.1.2 Cyclic Redundancy Check (CRC)

Like many electronic systems, communication errors can occasionally occur. One possible source of such errors is bit flips caused by ionizing radiation [3]. According to the system requirements defined in Section 2.1, the rover should be designed to withstand the effects of radiation from outer space. One of the reasons the BQ7692003PW was chosen over other variants is its implementation of a cyclic redundancy check (CRC), which provides a method to detect errors during data transmission.

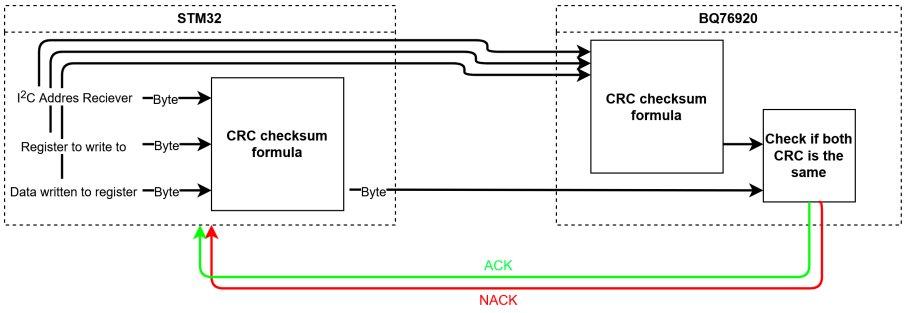

Figure 5.1: Block diagram of the CRC process.

The CRC is calculated by performing a standard checksum formula. This can be done normally by using the HAL_CRC_Calculate fucntion. However, this function does not operate well with the BQ7692003PW. For an unknown reason, the output has the wrong CRC byte. Therefor a new CRC calculation function was made. The code for this calculation can be found in the Git repository or in Appendix B.1. The inputs for the checksum are the I^2C address of the BQ7692003PW IC, one of the registers listed in Table 5.1 that the microcontroller wants to write to, and the data byte that is to be written. These three bytes are used to calculate the CRC, which is then sent along with the data over the I^2C bus. The slave device, in this case the BQ7692003PW, performs the same checksum internally. If both CRC values match, the data is written to the register and the BQ7692003PW acknowledges to the microcontroller that the write instruction was successful. This process is shown as a block diagram in Figure 5.1.

When using the STM32 as the microcontroller together with its HAL_I2C standard libraries for I^2C communication, an unexpected behavior occurs. The library allows multiple bytes to be requested at once, which is useful, for example, when reading the voltage of cell 1 from registers 0x0C and 0x0D simultaneously. The HAL library can read both registers at once and return their combined value. However, the library does not account for CRC checking. Normally, this would not be a problem if the number of requested bytes were doubled, since each data byte would be followed by its CRC byte. Unfortunately, this is not what happens. The output instead becomes two data bytes followed by two CRC bytes. The exact reason for this behavior is unclear, but it can be avoided by reading each data byte individually.

5.1.3 Battery Cell Monitoring

The BMS is able to read individual cell voltages. The BQ7692003PW chip does this internally, but the data can also be read over the I^2C by the microcontroller. The cell voltages are read by the onboard ADC of the BQ7692003PW chip. Knowing the individual cell voltages comes in handy during the debug phase. It also proves to be important for cell balancing.

The BQ7692003PW is able to bleed batteries. This cell balancing is used while charging when a battery's voltage is higher than that of the other batteries. The difference is there because no two cells are identical. Also, small inconsistencies in the battery grow over time. The capacity of a battery can degrade over time or due to environmental impacts, like temperature. Without cell balancing useful capacity of the battery pack is left unused.

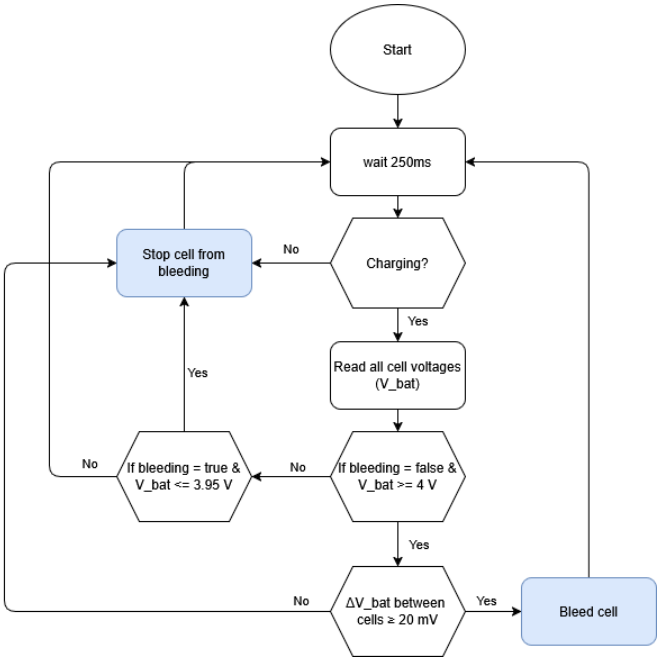

Figure 5.2: State machine of the passive top-balancing algorithm

The cell balancing, or bleeding, algorithm implemented in the BMS is shown in Figure 5.2. The algorithm is executed every 250 ms and first checks whether the BMS is in charging mode. If the system is not charging, bleeding is disabled for all cells.

This behavior is chosen for two reasons. First, bleeding while not charging would cause unnecessary energy loss from the battery pack. Second, continuous bleeding without charging could deeply discharge a cell. This would result in a large voltage difference between cells. When charging resumes, multiple cells would then need to bleed, leading to excessive energy dissipation and reduced efficiency of the solar charging system. It is therefore important that bleeding is only activated when the BMS is in charging mode.

When the BMS is in charging mode, the voltage of each cell is measured. A cell starts bleeding if its voltage exceeds 4 V and differs by more than 20 mV from the lowest cell voltage in the pack. This allows the remaining cells to catch up, improving the overall voltage balance of the battery pack. When a cell is set to bleeding, it stops bleeding when its voltage drops below 3.95 V or when the cell's voltage difference to the lowest cell is lower than 20 mV. This passive top-balancing algorithm is very common with rechargeable cells.

5.1.4 Current Control

On the BMS board in series with the cells, a shunt resistor is placed. The BQ7692003PW is able to read the voltage over this shunt resistor. The value of the shunt resistor is known and predetermined, so the desired voltage can be read as accurately as possible. In the case of this design, a maximum of 5 A of current is expected in most cases. 5 A is the maximum discharge rate, and 0.1A is the maximum charge rate of the Tadiran batteries, which can be seen in the Datasheet [20]. In the current testing setup, five of these cells are placed in series. This means that the voltage of the pack is increased to 20 V, but when another pack is created in the final design, the maximum charge and discharge current of the pack can change. Therefore, different shunt resistor can be soldered to the board to match the battery pack. The calculation of the current should be changed in the code of the microcontroller as well.

$$I_{\text{shunt}} = \frac{V_{\text{shunt}}}{R_{\text{shunt}}} \tag{5.1}$$

From Table 5.1, it can be derived that I^2C registers *0x32-0x33* have the coulomb counting data.

These two bytes contain data that represents the voltage over the shunt resistor. According to the Datasheet [7], the full scale range of this measured voltage is ± 270 mV, which means a LSB of 8.44 μV. The current through the shunt resistor can be calculated with Equation 5.2, where CC_{raw} is the signed combined 16-bit Coulomb Counter register value (CC_HI and CC_LO).

$$I_{\text{shunt}} = \frac{8.44\mu V \times \text{CC}_{\text{raw}}}{R_{\text{shunt}}} \tag{5.2}$$

In Table 5.1, it can be seen that I^{2}C registers *0x06-0x08* are used to configure the SCD and OCD Delays and threshold voltages. An ADC combined with a shunt resistor manages these SCD and OCD protection. In this design, a shunt resistor of 4 mΩ is chosen. More about the design choice of this particular shunt resistor in Subsection 5.1.5.

However, after testing these values, the results are presented more in Chapter 7. It can be seen that this equation does not represent the correct current data. During testing, it was observed that the measured value V_{meas} included a constant offset V_{offset}. It also became apparent that, in addition to the nominal shunt resistance R_{shunt}, parasitic resistance $R_{\text{parasitic}}$ needed to be taken into account.

$$V_{\text{meas}} = V_{\text{offset}} + I \cdot (R_{\text{shunt}} + R_{\text{parasitic}}) \tag{5.3}$$

$$I_{\text{shunt}} = \frac{V_{\text{meas}} - V_{\text{offset}}}{R_{\text{shunt}} + R_{\text{parasitic}}} \tag{5.4}$$

From testing, the values of these introduced offsets were determined. The voltage offset V_{offset} was found to be 0.5828 mV, and the parasitic resistance $R_{\text{parasitic}}$ was found to be 0.592 mΩ. Substituting these values into Equation 5.4 yields the corrected expression used to compute the current on this board. The full design schematic of this board can be found in Appendix E.1.

5.1.5 Battery Protection

As mentioned earlier, the I^{2}C registers *0x06–0x08* are used to configure the SCD and OCD delays and their corresponding threshold voltages. A shunt resistor of 4 mΩ is chosen, and in I^{2}C register *0x06* the short-circuit threshold voltage across this resistor can be set. This means that, in combination with the correct shunt resistor and configuration, almost any desired trip setup can be created. With a shunt resistor of 4 mΩ, different trip currents ranging from 5.5 A up to 500 A can be selected. Therefore, if different batteries are chosen in the final design, adjusting the register values allows a new trip current to be configured.

In the current design, a trip voltage of 44 mV is selected, which should result in a short-circuit detection threshold of 11 A. However, due to the parasitic resistances discussed previously in Subsection 5.1.4, this value is no longer accurate. Using the corrected shunt resistor model, a trip voltage of 44 mV instead results in a short-circuit detection threshold of 9.58 A, which is still an appropriate current limit for detecting short circuits.

Besides short-circuit detection, an overcurrent protection mechanism is also implemented. The main difference between short-circuit protection and overcurrent protection lies in their trip thresholds and response times. Short-circuit protection is characterized by a higher trip current and a very short trip delay, while overcurrent protection uses a lower trip current combined with a longer trip delay. Both mechanisms are necessary, as they protect against different fault conditions.

A short circuit is an electrical fault in which the current follows an unintended, very low-resistance path. This results in a sudden and extremely high current. To protect the batteries and other system components, such events must be detected and mitigated within microseconds.

Overcurrent conditions are different in nature. In this case, the load demands more current from the batteries than their rated continuous current limit. Temporary current peaks can occur during normal operation, for example, when charging an empty capacitor. These current spikes are typically short in duration and quickly settle to a safe operating level. Overcurrent protection is therefore designed to

tolerate brief current peaks while preventing sustained currents that exceed the allowable limits. Overcurrent faults are detected within milliseconds.

For this system, an OCD trip voltage of 25 mV is selected. Using the parasitic shunt resistor model, this corresponds to a threshold current of 5.4 A. This value is approximately 0.4 A above the specified continuous discharge current limit of the Tadiran batteries, providing protection while still allowing short-duration current transients.

Besides current protection, voltage protection is also required. When a battery is either undercharged or overcharged, irreversible damage can occur [18]. For safe operation, a battery must therefore be kept within the voltage limits specified by the manufacturer. These limits differ between battery types. For the Tadiran batteries used in this design, the allowable voltage range is from 2.0 V to 4.2 V.

As explained in Subsection 5.1.3, the voltage of each cell is continuously monitored using the onboard ADC of the BQ7692003PW [7]. The overvoltage (OV) and undervoltage (UV) trip thresholds can be configured via the I^2C registers *0x09–0x0A*, allowing the system to disconnect the battery when the voltage limits are exceeded.

5.2 PV panel Implementation

As mentioned earlier, the solar panels used on the rover are predetermined. The selected panels are the TJ Solar Cell 3G30A [2]. All PV panels have a characteristic IV-curve, meaning that for every voltage level, the panel can only deliver a certain maximum current. This also implies that there is a specific voltage/current point at which the delivered power is at its maximum, known as the maximum power point. Almost all PV panels use a Maximum Power Point Tracker (MPPT) to ensure that the system operates at this point. Initially, it was assumed that this approach would also apply to the Lunar Zebro rover. However, further investigation indicated that a Selective Power Point Tracker (SPPT) would be more suitable. This discussion is included in the Appendix A.2, as it was determined during the course of the thesis that implementing the SPPT would exceed the scope of the work.

5.3 Bidirectional Converter Implementation

The physical EPS PCB developed by Hubers is functional, but its compact layout provides almost no test or debug pins. This makes it impractical to integrate the new BMS directly onto the existing board. Combined with the need to redesign the startup circuitry, this led to the decision to rebuild certain parts of the EPS in a more modular way, while still basing the design on Hubers' original work.

Integrating the BMS demonstrated that adding a new subsystem to the rover inevitably requires modifications to the current architecture. For this reason, the BMS was designed as a separate module. After discussing the integration challenges with the thesis supervisors, it was decided to rebuild only the bidirectional converter at this stage. Once the solar panel system is introduced in the next development step, additional changes to other EPS components are expected. Redesigning all modules now, without knowing the final characteristics of the solar panel, would likely lead to unnecessary rework. Therefore, only the essential subsystem has been rebuilt for the moment. Which means that the modular bidirectional converter and startup circuit are redesigned. The design can be found in the Appendix E.2.

5.3.1 Half Bridge Bidirectional DC/DC Converter

The redesigned bidirectional converter is placed between the 12 V power bus and the BMS PCB, which is discussed in more detail in Section 5.4. As mentioned earlier, the design closely follows the concept presented by Hubers [5]. The overall architecture of the bidirectional converter is shown in Figure 5.3. In practice, the final implementation is interleaved. However, a non-interleaved configuration is shown in the figure. An interleaved converter consists of two identical converter stages operated with a phase shift, which improves efficiency and reduces current ripple.

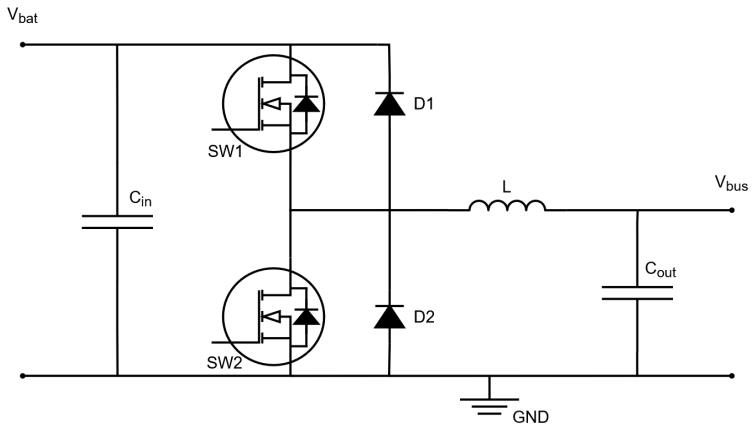

Figure 5.3: schematic of the half bridge bidirectional DC/DC converter.

The bidirectional converter has two switches, $SW1$ and $SW2$, which control the direction of energy flow. The inductor L serves as the energy storage component, while the input and output capacitors, C_{in} and C_{out}, smooth the voltage by filtering high-frequency ripple. This two-switch bidirectional converter operates in three distinct modes.

Before discussing these operating modes, the voltage/current relationship of the inductor must be introduced. The fundamental behavior of an inductor is given by Equation 5.5, which shows that a change in current over time induces a voltage across the inductor. This is exploited in the bidirectional converter to either increase or decrease the voltage level.

$$v_L(t) = L\frac{di_L(t)}{dt}. \tag{5.5}$$

The switching times of transistors $SW1$ and $SW2$ are defined by the duty cycle D. During operation, the transistors are never turned on simultaneously. Instead, they operate in a complementary manner. For example, with a duty cycle of 60%, one transistor is conducting for 60% of the switching period, while the other conducts for the remaining 40%. In practice, complementary switching requires the introduction of a dead time between the switching transitions. This ensures that there is a short interval during which neither transistor is conducting, preventing both switches from being on simultaneously. By adjusting the duty cycle D, different voltage levels can be obtained in the various operating modes of the converter. The operating modes are Buck mode, Boost mode and Buck-Boost mode. The latter mode will not be used in this bidirectional converter. This mode is still explained in the Appendix B.2.

5.3.2 Buck Mode $V_{\text{bat}} > V_{\text{bus}}$

The first operating mode is the buck mode, which occurs when $V_{\text{bat}} > V_{\text{bus}}$. In this mode, energy is transferred from the battery pack to the power bus. Voltage step-down is achieved through two switching phases. During the first phase ($0 \leq t < DT_s$), $SW1$ is closed while $SW2$ remains open, allowing current to flow through the inductor. The resulting inductor voltage is

$$v_L = V_{\text{bat}} - V_{\text{bus}}, \qquad 0 \leq t < DT_s. \tag{5.6}$$

By substituting this expression into Equation 5.5, the slope of the inductor current can be derived. Since $V_{\text{bat}} > V_{\text{bus}}$, the resulting voltage across the inductor is positive, causing the inductor current to increase over time.

$$\frac{di_L}{dt} = \frac{V_{\text{bat}} - V_{\text{bus}}}{L}. \tag{5.7}$$

In the second phase ($DT_s \leq t < T_s$), $SW1$ is opened and $SW2$ is closed, which changes the voltage across the inductor to

$$v_L = -V_{\text{bus}}, \qquad DT_s \leq t < T_s. \tag{5.8}$$

Substituting this voltage into Equation 5.5 again shows that the inductor current now has a negative slope. As a result, the current decreases over time during this phase.

$$\frac{di_L}{dt} = \frac{-V_{\text{bus}}}{L}. \tag{5.9}$$

Over one switching period T_s, the average voltage across the inductor must be zero. Otherwise, the inductor current would continuously increase or decrease from cycle to cycle. This can be expressed as

$$DV_{\text{bus}} + (D-1)(V_{\text{bus}} - V_{\text{bat}}) = 0. \tag{5.10}$$

By simplifying this expression, the relationship between the bus voltage and the battery voltage is obtained. The resulting equation shows how the duty cycle D determines the output voltage:

$$V_{\text{bus}} = V_{\text{bat}} \cdot D. \tag{5.11}$$

5.3.3 Boost Mode $V_{\text{bat}} > V_{\text{bus}}$

The second operating mode is the boost mode, in which energy is transferred from the 12 V bus to the battery pack. In this mode, the converter increases the voltage level by appropriately switching transistors $SW1$ and $SW2$.

During the first phase ($0 \leq t < DT_s$), transistor $SW2$ is closed while $SW1$ remains open. As a result, current builds up in the inductor and the voltage across the inductor is given by

$$v_L = V_{\text{bus}}, \qquad 0 \leq t < DT_s. \tag{5.12}$$

Substituting this expression into Equation 5.5 shows that the magnitude of the inductor current increases over time. Due to the chosen reference direction, this current flows from right to left in Figure 5.3, resulting in

$$\frac{di_L}{dt} = \frac{V_{\text{bus}}}{L}. \tag{5.13}$$

This indicates that the inductor stores energy while the current through it increases in the opposite direction compared to buck operation.

In the second phase ($DT_s \leq t < T_s$), $SW2$ is opened and $SW1$ is closed. Since the battery voltage exceeds the bus voltage, the voltage across the inductor changes to

$$v_L = V_{\text{bus}} - V_{\text{bat}}, \qquad DT_s \leq t < T_s. \tag{5.14}$$

Because $V_{\text{bat}} > V_{\text{bus}}$, the resulting inductor voltage is negative, causing the inductor current to decrease. During this phase, the energy stored in the inductor is transferred to the battery pack. Over one switching period the average inductor voltage must be zero, otherwise the average current slope $\frac{di_L}{dt} \neq 0$. therefore

$$D(V_{\text{bat}} - V_{\text{bus}}) + (D-1)(-V_{\text{bus}}) = 0. \tag{5.15}$$

After simplifying this expression, a direct relation between the bus voltage and the battery voltage is obtained. This relation shows how the duty cycle $\frac{1}{1-D}$ sets the resulting output voltage:

$$V_{\text{bat}} = \frac{V_{\text{bus}}}{1-D} \tag{5.16}$$

5.4 Integration in the Pre-Designed Bus

The bus is already designed and built by Hubers. This physical EPS PCB design could immediately be used in the project. During testing, it could be concluded that the original design of Hubers did not account for a BMS systems connected between the EPS PCB and the battery. The first problem lies in the startup circuit and the bidirectional converter. The circuit of Hubers is correct and functional without the use of BMS, see Figure 5.4a.

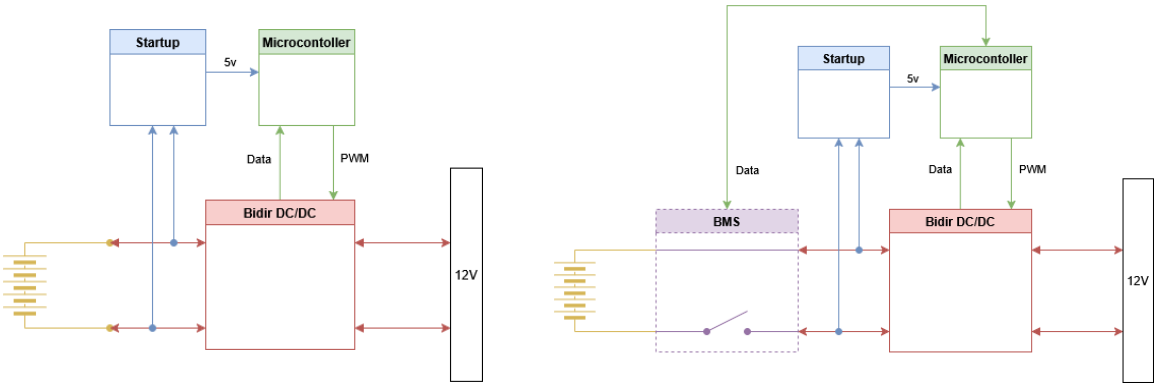

Figure 5.4: (a.) Startup circuit and bidirectional converter as designed by Hubers (b.) BMS placed before startup circuit and bidirectional converter as designed by Hubers.

Figure 5.4b shows the setup with the BMS directly connected to the design of Hubers. The first problem lies in the protection circuit of the BMS. As mentioned before in Subsection 5.1.4, the BMS includes an overcurrent protection, which is represented as a switch in Figure 5.4b. However, this switch is never meant to open during normal operation. If it does open, the current protection is activated, and the node after the switch, where the startup circuit is connected, loses its power supply.

At the same time, there is no power available from the bidirectional converter, because the microcontroller is required to operate it. The microcontroller is also needed to close the switch again. This means that once the switch opens, it cannot be closed again, resulting in the batteries being permanently disconnected from the circuit. To solve this, some adjustments are made to the circuit of Hubers, see Figure 5.5.

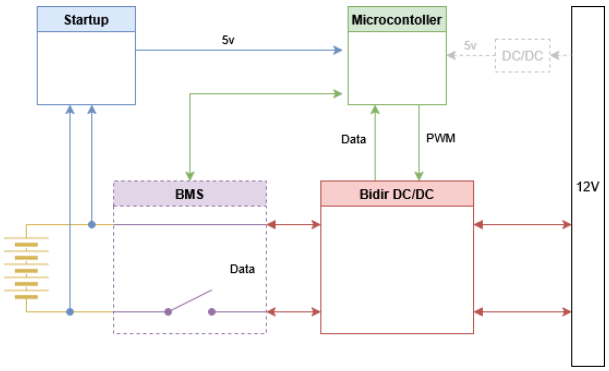

Figure 5.5: BMS placed before altered circuit inspired by the design of Hubers.

The adjustment made compared to the previous design is that the startup circuit is now again connected to the battery directly. A fuse will be used to protect the batteries and the circuit. Also, through a DC/DC converter, the microcontroller is powered by the 12V Bus. There are two main reasons for changing this design. The first reason is that there is no scenario in which the BMS permanently disconnects itself. Since there is always 12V available on the bus, provided either by the batteries or by the solar panel, this means that the startup circuit can always turn on.

The second advantage of this design is that when the batteries are completely depleted, for example during a lunar night, the system can recover automatically. As soon as the sun reaches the solar panels and they start supplying 12V, the bidirectional converter becomes operational again and can recharge the fully depleted batteries.

Notice that this setup is an improvement on the previously designed bidirectional converter. However, it is suspected that when the solar panels are integrated into this system, new challenges will occur and the design will once again be improved.

5.5 Manufactered Boards

The Electrical Power System (EPS) consists of a Battery Management System (BMS) PCB, an STM32 Nucleo development board, a solar panel, and several DC/DC converters. The BMS PCB and the Bidirectional Converter PCB are designed in Altium Designer and manufactured by Eurocircuits. All components were sourced from Mouser Electronics and assembled in Lunar Zebro's laboratory.

5.5.1 Battery Management System PCB

The manufacturing process of the BMS PCB includes several steps. First, solder paste is applied using a top stencil. The PCB is fixed to the workbench, as shown in Figure 5.6a, and the metal stencil is placed on top so that its openings align with the SMD pads on the board, see Figure 5.6b. The solder paste is then spread across the stencil with a scraper, filling the openings and transferring paste onto the pads below.

As shown in Figure 5.6c, the stencil contained a small manufacturing error: some holes were not fully cut out. Because of this, solder paste had to be applied manually to those pads using tweezers. Although this method was less precise, it was expected that the solder would flow evenly during reflow and form proper electrical connections. The result of this step is shown in Figure 5.6d. The pads for R4, C3, and C4 were manually adjusted, which explains their slightly less clean appearance

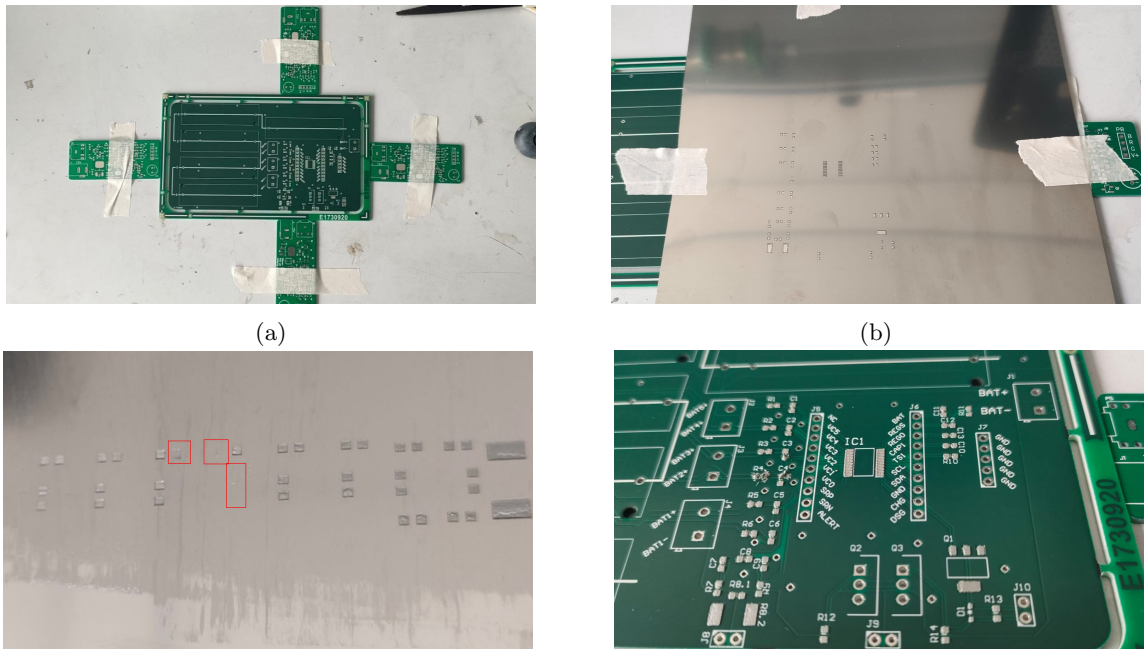

(a) (b)

(c) (d)

Figure 5.6: (a.) Clamping the PCB to the table. (b.) Aligning the top stencil on top of the pcb. (c.) Red markings show the fabrication Error in the top stencil. (d.) Solder paste result after using the top stencil and tweezers.

After the paste was applied, all SMD components were carefully placed onto the board using tweezers. The PCB was then placed in a reflow oven to solder the components. Visual inspection confirmed that all parts were properly connected, and this was verified with a multimeter. Any detected short circuits

were corrected. Finally, the through-hole components were soldered to complete the assembly. The finished PCB is shown in Figure 5.7.

Figure 5.7: Finished BMS PCB with clean connections.

5.5.2 Bidirectional Converter PCB

The manufacturing process of the bidirectional converter PCB is largely identical to that of the BMS PCB. The PCB is mounted to the workbench, as shown in Figure 5.8a. The top stencil, which this time did not contain fabrication errors, is then placed on top of the board (Figure 5.8b). A scraper is used to evenly apply solder paste across the stencil openings. After removing the stencil, the PCB is uniformly covered with solder paste, as shown in Figure 5.9.

(a) (b)

Figure 5.8: (a.) Clamping the bidirectional converter PCB to the table. (b.) Aligning the top stencil on top of the pcb.

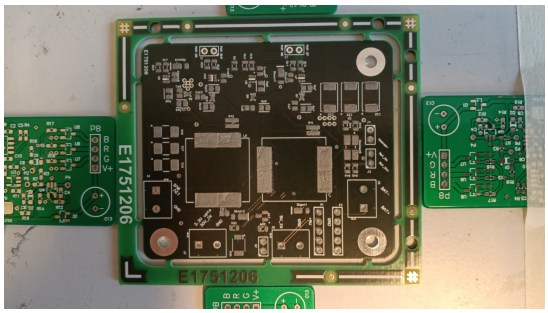

Figure 5.9: Solder paste result after using the top stencil.

Although the overall process does not differ significantly from the manufacturing of the BMS PCB, several short circuits were observed after assembly. Further inspection showed that most of these shorts occurred around the gate driver (1EDN7146UXTSA1) and the power transistor (EPC2014C). The stencil

openings for these components allowed too much solder paste to pass through, which caused solder bridges to form underneath the components during reflow. The short circuits were removed using tweezers and a heat gun. The affected components were desoldered and reassembled by hand using a reduced amount of solder paste. After this rework process, the short circuits were no longer present.

Chapter 6

Testing And Verification

In this chapter, the test and verification procedures are defined to assess whether the EPS and its subsystems behave as intended. The chapter starts with the development of test procedures for the Tadiran TLI-1550ES batteries. These tests are designed in accordance with USAF SMC standards [22, 23] and are tailored to the mission requirements. Subsequently, the manufactured Battery Management System (BMS) is tested to verify its functionality. The corresponding test procedures are described in Section 6.2. Afterward, tests for the bidirectional converter are presented, followed by system-level integration testing. Finally, a brief description of the overall test setup is provided.

6.1 Battery Test Plan

In the simulation, the TLI-1550ES batteries are suitable for providing power to the rover. However, this result is based on ideal conditions, assuming the batteries perform exactly as specified as stated in the Tadiran datasheet [20]. In real-world scenarios, this ideal behavior is rarely the case. Batteries have minor imperfections from fabrication, behave differently under varying temperatures, and experience reduced capacity after a few charge–discharge cycles. These characteristics must be tested before the batteries can be verified for use in the final rover to be deployed in space. These tests are designed in accordance with the USAF SMC-S-007 [22] and SMC-S-018 [23] standards.

6.1.1 Capacity Test

According to the USAF SMC-S-007 standard [22], the battery's thermal control design must be verified through testing to ensure that temperature management and gradients remain within acceptable limits under all operational conditions. According to the USAF SMC-S-018 standard [23], the batteries should meet operational capacity requirements at worst-case temperature conditions. In this case, this would be $-50°C$ and $+80°C$.

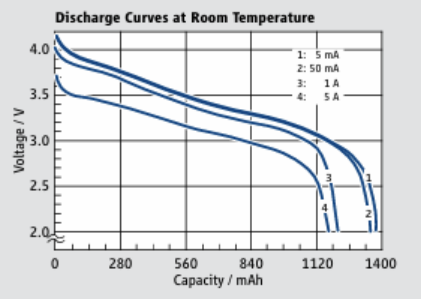

Figure 6.1: Discharge curves at different discharge currents according to the Tadiran datasheet, picture is taken from this datasheet [20].

The Tadiran datasheet [20] provides graphs with different discharge curves, see Figure 6.1. These curves should be verified at different temperatures and different C-rates, The C-rates, 4.17C and 0.83C,

are the ones used in the datasheet and what is interesting to compare against. These C-rates can also be denoted as a discharge current of 5A and 1A. The tests are conducted at three different temperatures: $-50°$C, $+20°$C and $+80°$C.

6.1.2 Capacity Endurance Test

According to the USAF SMC-S-007 standard [22], batteries should be tested on the life expectancy. When Batteries are cycled in a discharge and charging patern they wear down. To simulate this max discharge and charge patern the battery should be cycled for 14 days at the expected charging and discharging current of the mission. This shows how the SOH degrades. It can be decided if this is viable. For the Tadiran batteries, 14 days nonstop cycling means 25 times charging and discharging cycles, where the cell is charged at 0.1 A and discharged at 1.0 A. Since the test requires supervision and charging the cells takes approximately 12 hours, this test cannot be performed with the current setup and available tools. Therefore, the charging current is increased to 0.3 A. This does not provide the exact results of interest, but it gives a worst-case estimate of the long-term behavior of the cells.

6.1.3 Internal Resistance Test

This test retrieves the internal resistance of the battery. With the internal resistance, the amount of heat that the battery produces could be retrieved. With the SMC-S-007 standard [22] in mind, this parameter must be characterized to verify that the battery's thermal performance meets the requirements under all operating conditions.

To determine the internal resistance of the cell, the DC Internal Resistance (DCIR) measurement method is applied [25]. The procedure is as follows. First, the battery cell is fully charged using a battery charger. After charging, the open-circuit voltage of the cell V_{open} is measured while no current is flowing. Next, a short current pulse with a known magnitude I and a duration of approximately 200 ms is applied, flowing from the positive to the negative terminal of the cell. During this pulse, the terminal voltage of the cell, V_{load}, is measured. The observed voltage drop is caused by the internal resistance of the cell.

$$R_{\text{internal}} = \frac{V_{\text{open}} - V_{\text{load}}}{I} \tag{6.1}$$

Assuming the current is known and constant during the pulse, the internal resistance R_{internal} can be calculated using Ohm's Law, as shown in Equation 6.1. Figure 6.2a and Figure 6.2b illustrate this measurement principle. In the first figure, where no current flows through the cell, the open-circuit voltage V_{open} is measured. In the second case, when a current is drawn from the cell, a voltage drop V_{internal} occurs across the internal resistance R_{internal}. As a result, the terminal voltage decreases compared to the open-circuit condition. Under ideal conditions.

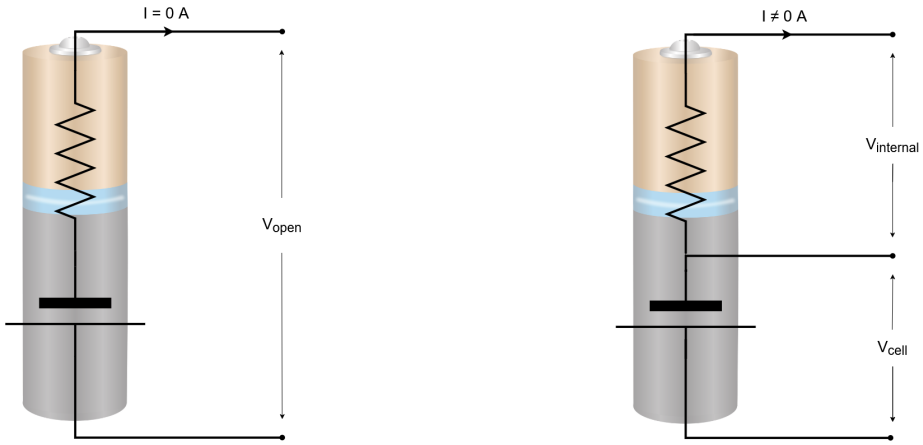

(a) (b)

Figure 6.2: (a.) The open cell voltage V_{open} is measured over the cell. (b.) The cell voltage V_{load} is measured over the cell. this consist of V_{open} and the negative voltage V_{internal}.

The open-circuit voltage V_{open} is equal to the cell voltage V_{cell} because no current flows through the cell during this measurement. Under this condition, the internal resistance of the cell does not cause a voltage drop. As a result, the voltage measured at the terminals directly corresponds to the electrochemical potential of the cell. Therefore, when the cell is in an open-circuit state, the terminal voltage represents the cell voltage, and $V_{\text{open}} = V_{\text{cell}}$.

6.1.4 Self Discharge Test

For batteries that remain installed in a vehicle for extended periods before use, additional hardware may be required to maintain their state of charge at an acceptable level. According to the USAF SMC-S-018 standard [23], it is essential to characterize the self-discharge behavior of the cells. This can be evaluated by fully charging the batteries and monitoring the decrease in state of health (SOH) or open-circuit voltage over a defined storage period. A duration of approximately 30 days is considered sufficient for this test, as typical lunar fuel-efficient transfer missions take around 30 days to reach the Moon. [16].

6.1.5 Exploring Charging Current Limits

This test is not necessarily intended to evaluate the quality of the batteries. It is more exploratory. According to the Tadiran battery datasheet [20], the maximum allowable charging current at room temperature is 100 mA. This is to guarantee a long life of the cell. For the Lunar Zebro, the cells should survive only for one lunar day in its first mission. In this test, higher charging currents and consequently a higher maximum charging power are investigated.

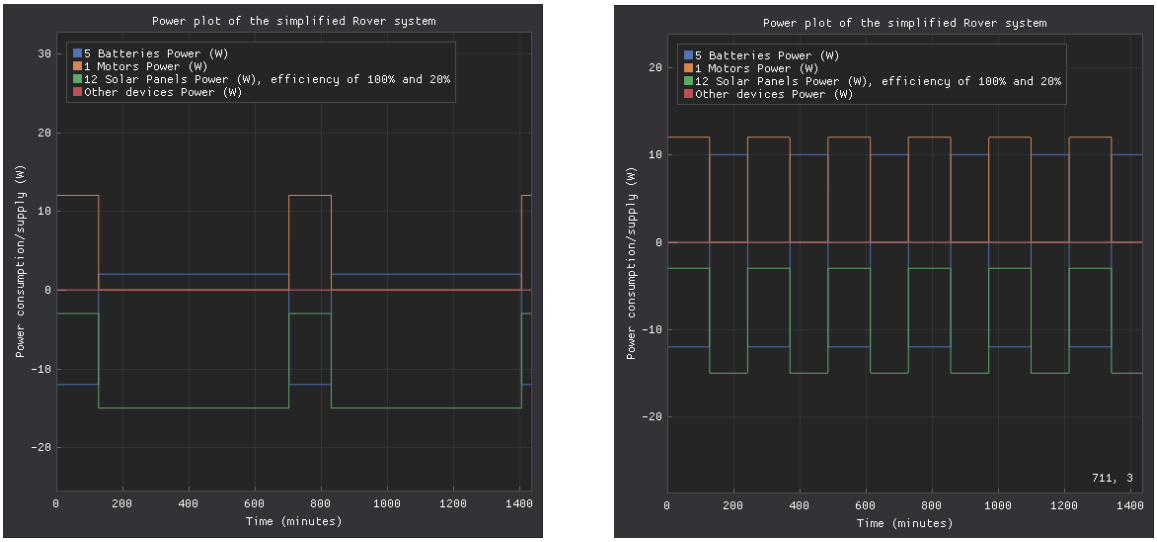

(a) (b)

Figure 6.3: (a.) Five batteries at a charging current of 0.1 A. (b.) Five batteries with increased charging current of 0.5 A.

Figure 6.3a shows the test setup in the simulator with five batteries, one motor, sufficient solar power, and a maximum charging power of $0.1\,\mathrm{A} \times 4\,\mathrm{V} = 0.4\,\mathrm{W}$ per battery. Figure 6.3b shows the same setup; however, in this case the batteries are charged with $0.5\,\mathrm{A} \times 4\,\mathrm{V} = 2\,\mathrm{W}$ per battery.

It can be observed that the rover is able to recharge its batteries more quickly and therefore achieve a higher number of walking cycles. However, according to the Tadiran datasheet [20], charging the batteries with a higher charging current causes damage. This test investigates how such damage manifests itself and whether it has a significant impact on the overall mission performance.

6.2 BMS functionality testing

According to the USAF SMC-S-018 standard [23], battery systems should include several safety and control functions to ensure reliable operation under all conditions. To verify this, the BMS will be tested on its main protection features. These are overvoltage protection, undervoltage protection, overcurrent protection, short circuit detection, cell balancing, and state-of-charge (SOC) estimation. Each of these functions will be tested to make sure the BMS can correctly detect and respond to abnormal situations, preventing damage to the cells and ensuring safe operation.

6.2.1 Overvoltage Protection Test

To verify the correct operation of the overvoltage protection, a straightforward test procedure is applied. Five fully discharged cells are placed in the battery pack. Under normal conditions, a fully charged cell reaches a voltage of 4.2 V, resulting in a total pack voltage of approximately 21 V for five cells connected in series.

A laboratory power supply is then configured with an output voltage of 23 V and a current limit of 0.1 A. Because of the imposed current limit, the supply voltage initially drops to the battery pack voltage, and the cells begin charging with a constant current of 0.1 A. As the cells continue to charge, their voltages increase accordingly.

When the voltage of any individual cell reaches the configured overvoltage protection threshold, the BMS automatically opens the circuit, causing the charging current to cease. In the present configuration, this protection threshold is set to 4.2 V per cell. Consequently, once a single cell reaches this voltage, power flow to the battery pack is interrupted.

6.2.2 Undervoltage protection Test

The undervoltage protection can be evaluated using a similar approach. In this case, a digital electronic load is used instead of a laboratory power supply and is connected to the output of the BMS. The load is preprogrammed to draw a constant current of 1 A from the battery pack. As current is drawn, the overall pack voltage gradually decreases.

Once the voltage of any individual cell reaches the configured undervoltage protection threshold of 2.1 V, the BMS disconnects the load by opening the circuit. As a result, the current flow is interrupted. This response confirms the correct operation of the undervoltage protection mechanism.

6.2.3 Overcurrent Protection Test

As described earlier in Subsection 5.1.5, the battery pack must be protected against sustained high currents. The overcurrent protection threshold is configured at 5.4 A, meaning that if a current exceeding this value flows for longer than 20 ms, the BMS will interrupt the current path.

During testing, it is undesirable to route such high currents through the batteries themselves. For this reason, connector J8 is introduced, as shown in Figures 6.4a and 6.4b. This connector allows a controlled current to be driven through the shunt resistor without passing through the battery cells. As illustrated in Figure 6.4a, the current flows exclusively through resistor R8.1. Resistor R8.2 represents an alternative footprint of the same shunt resistor but remains unsoldered, as visible in Figure 6.4b.

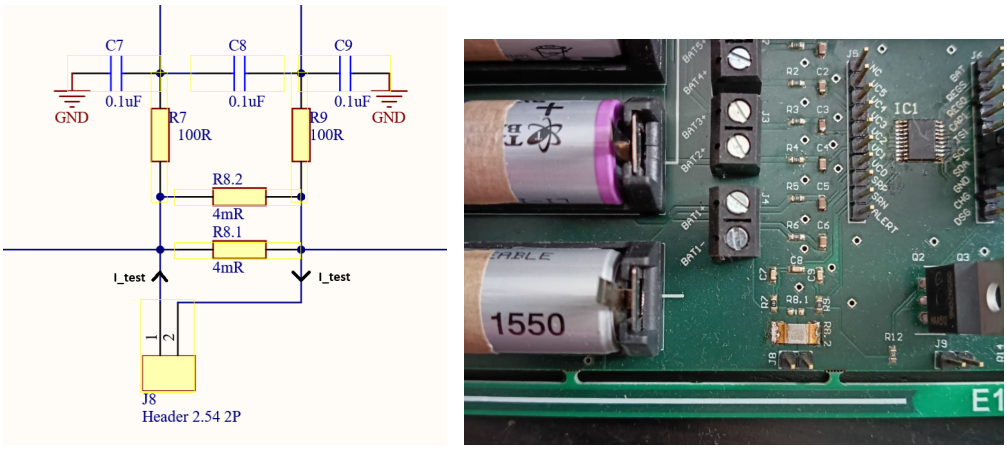

(a) (b)

Figure 6.4: (a.) Schematic of the shuntresistor in combination with the J8 connector. (b.) The shunt resistor and J8 connector on the board. Note that R8.2 is not soldered on the board, it is a different footprint for the shunt resistor.

By routing the current solely through the shunt resistor, the BQ76920 measures a current that exceeds the configured threshold while the batteries remain isolated. This approach effectively simulates an overcurrent condition and allows verification that the BMS responds as intended.

6.2.4 Short-Circuit Protection Test

The short-circuit protection is tested using the same setup as the overcurrent protection test, with the difference that the applied current is increased. The short-circuit protection threshold is set to 9.6 A for longer than 70 μs. The method used to determine this value is discussed in Subsection 5.1.5.

6.2.5 Cell Balancing Test

The cell balancing functionality can be evaluated using two separate tests: one with the cell balancing algorithm enabled and one with cell balancing disabled. After charging the battery pack in both con-

figurations, the difference in stored energy between the two packs can be determined. This comparison shows the impact of the cell balancing algorithm. In addition, by logging which cells are actively being bled through the balancing resistors and which cells remain inactive, the correct operation of the balancing algorithm can be verified.

The Tadiran cells used in this system are relatively new. As a result, it can be that the individual cell voltages may not differ by more than 20 mV while charging. The bleeding algorithm may not activate under normal conditions. In that case, the algorithm would not operate during testing and the impact of the algorithm can not be measured.

To force the algorithm to activate, four fully discharged cells and one partially discharged cell are connected to the BMS. A cell discharged by 710 mAh corresponds to approximately 33% state of charge. This cell reaches the 3.95 V threshold earlier than the other cells. Once the voltage difference exceeds 20 mV, the bleeding algorithm is triggered. This allows the remaining cells additional time to charge. In this way, a mismatch between cells is simulated, which can occur as batteries age and are used over longer periods of time.

The difference in stored energy between the battery packs with and without bleeding shows the effect of the algorithm.

6.3 Bidirectional Converter Test Plan

After the redesign and manufacturing of the bidirectional converter, a series of tests is carried out. At first, testing focuses on the simpler subsystems of the bidirectional converter, allowing its basic functionality to be verified. After that, tests are performed on the more complex parts. This stepwise approach ensures the correct operation of the individual subsystems of the converter, which reduces integration risks.

6.3.1 Voltage Readout

The bidirectional converter is equipped with an algorithm that determines the direction of power flow within the system. This decision is based on voltage measurements at the converter terminals. These terminal voltages are scaled down using resistor dividers and subsequently read by the microcontroller through its analog-to-digital converters.

6.3.2 Onboard 5V Converter

Another relatively simple system is the added onboard 5V converter, which can be read more about in Section 5.4. From the 12V bus this converter supplies power to the microcontroller. This system is added after the design of Hubers. Therefor the functionality needs to be verified. The test is performed by powering the 5V converter with 12V, connecting the microcontroller and verifying everything is still functional.

6.3.3 PWM Generation

As described in Section 5.3, generating a correct PWM signal can be challenging. This signal is used to switch the power transistors on and off, and the duty cycle of the PWM signal determines the converter output voltage. To verify correct PWM generation, tests are performed in which the voltage feedback to the microcontroller is connected to the board, while the PWM signals are intentionally not connected to the power transistors. During these tests, the PWM signal is measured and plotted. This allows the duty cycle to be evaluated and compared to the intended output voltage. In this way, it can be verified that the PWM signal is generated correctly before applying it to the power stage.

6.3.4 Bidirectional Converter Functionality Testing

The functionality of the bidirectional converter is tested by attempting to operate all subsystems together in a controlled scenario. The first test involves configuring the converter in buck mode, using a steady 18 V power source and attempting to produce a 12 V output. The objective is to verify that all parts of the converter—including the PWM control, power transistors, and feedback loops—work together as intended to regulate the output voltage.

During this test, the signals from the microcontroller are monitored to verify the correct operation of the control logic and PWM generation. This approach allows an initial functional verification of the integrated bidirectional converter without exposing the system to unnecessary risk.

6.4 Test Setup

6.4.1 Overview

To validate the functionality of the Battery Management System (BMS) and verify battery behavior under different circumstances as described before, a dedicated laboratory test setup was constructed. The complete setup is shown in Figure 6.5, and consists of the following main components:

- A laptop connected via UART, providing a serial interface for real-time monitoring, logging, and parameter adjustments.
- The STM32 Nucleo board, this is a reprogrammable stm32 chip that executes code, converts I^2C to UART and controls the BMS IC.
- A programmable laboratory power supply, used to provide a controlled charging input.
- A DC electronic load, used to apply repeatable discharge profiles, trigger over-current events, and test protection thresholds. The electronic load is also used to test individual batteries.
- The BMS PCB, which contains the BQ76920 IC, the battery pack and the circuitry to let the BMS function.
- A battery charger provides power to individual batteries, which then can be tested afterwards.

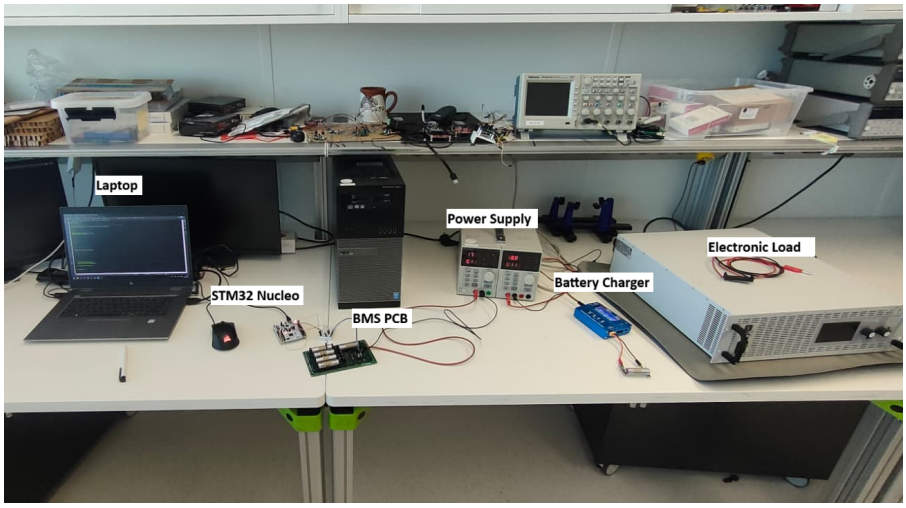

Figure 6.5: Test Setup for battery and BMS testing.

Chapter 7

Results and Discussion

In this chapter, all results of the tests from the previous chapter are presented and discussed. The structure of this chapter follows the structure of the testing chapter, Chapter6. First, the results of the battery tests are discussed, then the BMS and finally the Bidirectional converter.

7.1 Battery Validation

7.1.1 Capacity Test Results

In the first test, the capacity of the batteries is measured at different discharge currents and temperatures. The resulting discharge curves are compared with the manufacturer data provided by Tadiran [20], as shown in Figure 6.1. Tests at $-80°C$ and $+50°C$ could not be performed, as no suitable temperature chambers were available. Therefore, all capacity measurements were only done at room temperature.

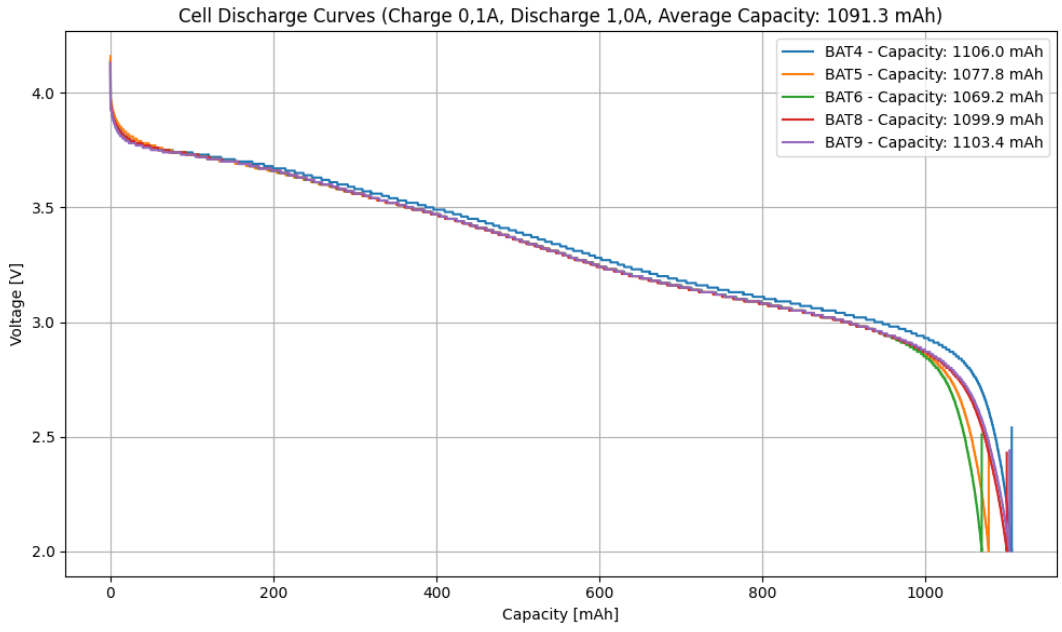

Figure 7.1: Five different tests, where a cell is charged at 0.1 A and discharged at 1 A. The average capacity of the cells in this setup is 1091.3 mAh.

Figure 7.1 shows the discharge curves of five individual cells. The cells are charged at 0.1 A and discharged at 1 A. The measured average capacity of the cells is 1091.3 mAh. When compared to the datasheet discharge curve in Figure 6.1, it can be concluded that the measured battery capacity is 9.1% lower than the datasheet value of 1200 mAh.

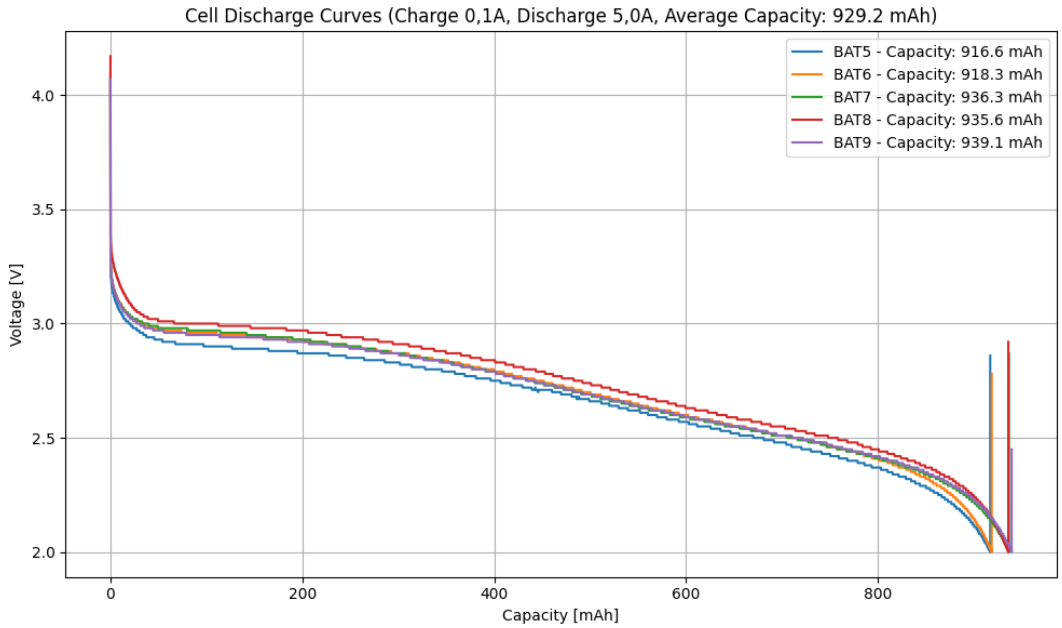

Figure 7.2: Five different tests, where a cell is charged at 0.1 A and discharged at 5 A. The average capacity of the cells in this setup is 929.2 mAh.

In addition to the 1 A discharge test, measurements were also performed at a discharge current of 5 A. Figure 7.2 shows the discharge curves of five individual cells charged at 0.1 A and discharged at 5 A. Compared to the datasheet data, the measured capacity is lower. The cells show an average capacity of 929.2 mAh, whereas the datasheet specifies a capacity of around 1160 mAh at a 5 A discharge current [20]. This corresponds to a reduction in capacity of 19.9 %.

The reduction of capacity in both tests is expected, as the datasheet values are specified under ideal conditions, whereas the measurements include additional losses from wiring, measurement equipment, and cell-to-cell variation.

7.1.2 Capacity Endurance Test Results

In Subsection 6.1.2, the importance of monitoring the long-term behavior of the cells is discussed in relation to battery pack reliability. It is calculated that the battery pack undergoes 25 charge and discharge cycles during the mission, when charged at 0.1 A and discharged at 1.0 A. As described earlier, charging the cells at 0.1 A takes too long to be fully supervised. Therefore, the charging current is increased to 0.3 A for this test. This higher charging current has a negative impact on the cells, meaning that the results represent a worst-case scenario. When charged at 0.1 A, the expected degradation would be lower.

Figure 7.3 shows the results of the cycling test. At the start of the test, corresponding to 100% state of health (SOH), the cell capacity is 1008.44 mAh. After the final cycle, the measured capacity is 806.96 mAh, which corresponds to an SOH of 80.0%. For completion, in Appendix D.0.3, all individual SOH results can be seen.

These results are unexpected when compared to values reported in the literature for similar cells under comparable operating conditions [8]. In those studies, cells typically reach an SOH of 80% after more than 1000 charge/discharge cycles, rather than after only 25 cycles. This suggests that charging the cells at a current approximately 300% higher than the recommended value has a substantial impact on the state of health.

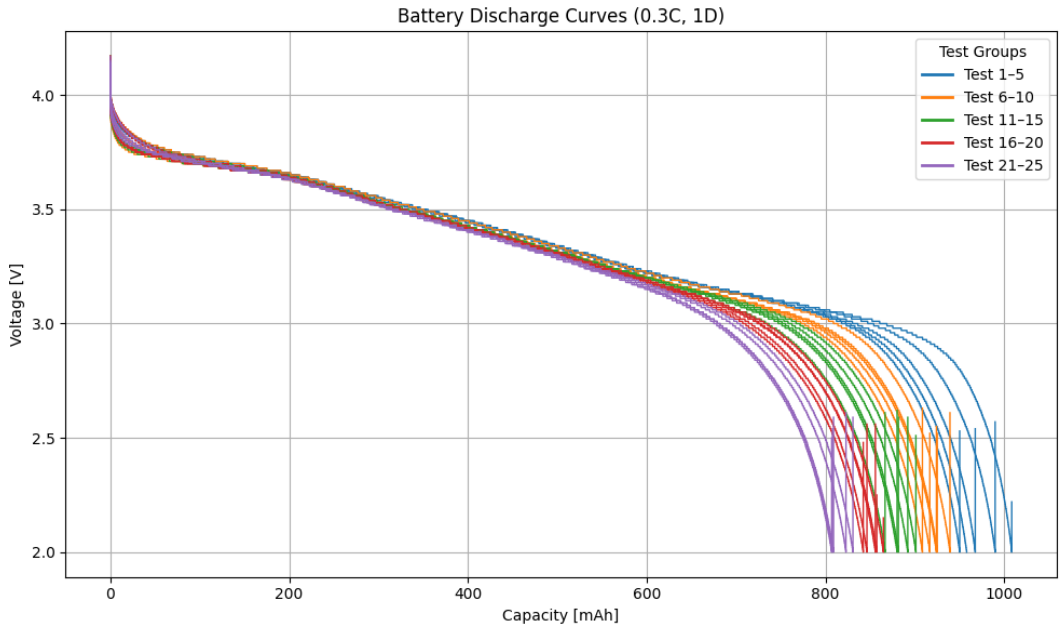

Figure 7.3: The plot shows the degradation of the SOH over several discharge cylces.

7.1.3 Internal Resistance Test Results

In Subsection 6.1.3, the DCIR measurement procedure is described. These measurements are performed at the start of the testing period and repeated at the end of the thesis. Table 7.1 shows that 9 out of 15 cells exhibit an increase in internal resistance by the end of the testing period, which is consistent with expected aging behavior. It can also be observed that the cells with the largest increase in resistance, namely BAT6, BAT9, and BAT15, were used more extensively than the other cells, with the exception of BAT1. This observation suggests a possible correlation between charging at a current of 0.5 A and a stronger increase in internal resistance.

Cell	**Initial internal resistance (mΩ)**	**Final internal resistance (mΩ)**	**Amount of tests**
BAT1	160	170	29
BAT2	150	150	3
BAT3	160	160	3
BAT4	150	160	3
BAT5	160	170	4
BAT6	150	180	8
BAT7	160	170	7
BAT8	150	170	8
BAT9	150	180	8
BAT10	150	150	3
BAT11	150	150	3
BAT12	160	160	3
BAT13	160	160	3
BAT14	160	160	3
BAT15	150	180	10

Table 7.1: Internal resistance of individual battery cells measured at the beginning and end of testing.

7.1.4 Self Discharge Results

Test D1 simulates the 30-day travel time to the Moon, during which the battery pack remains idle. In this test, a single cell is charged to 100% SOC at a current of 0.1 A. The cell is then stored at a temperature of 20 °C for a period of 30 days. After this storage period, the cell is discharged at a current of 1 A. Figure 7.4 shows the resulting discharge curve. The measured capacity of the cell is 1052.2 mAh. In Test A1, see Section 7.1.1, an average capacity of 1091.3 mAh was measured. This corresponds to a capacity reduction of 3.5% compared to the average value. This indicates that storing the cells for 30 days has zero to none influence to degradation of the capacity of the cell.

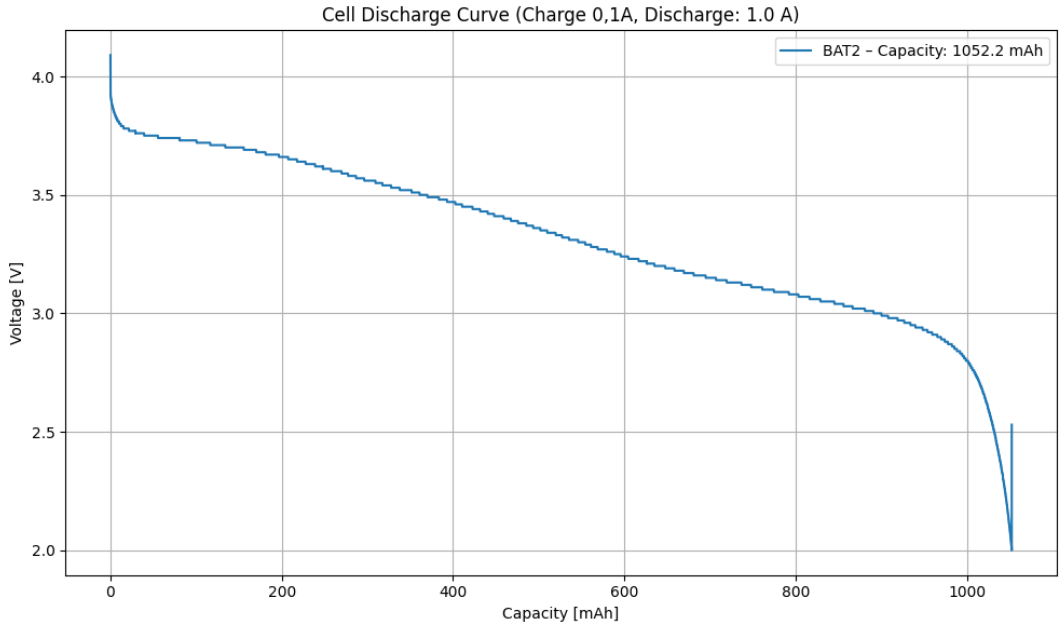

Figure 7.4: Discharge curve of a fully charged cell, that charged at 0,1 A, stored for 30 days and then discharged at 1 A.

7.1.5 Exploring Charging Current Limits

According to the datasheet, the maximum allowable charging current of the cells is 100 mA, which is specified to preserve cell lifetime. As stated in Subsection 6.1.5, the first mission lasts one lunar day. This results in a limited required lifetime for the battery pack. For this reason, the cells are also tested at charging currents beyond their specified limit.

Figure 7.5 shows the measured capacities of five individual cells charged with a current of 500 mA. The average capacity of these cells is 1023.7 mAh. In Test A1, see Section 7.1.1, cells charged at 100 mA showed a higher average capacity. The capacity of the cells charged at 500 mA is reduced by 6.2% compared to the cells charged at 100 mA.

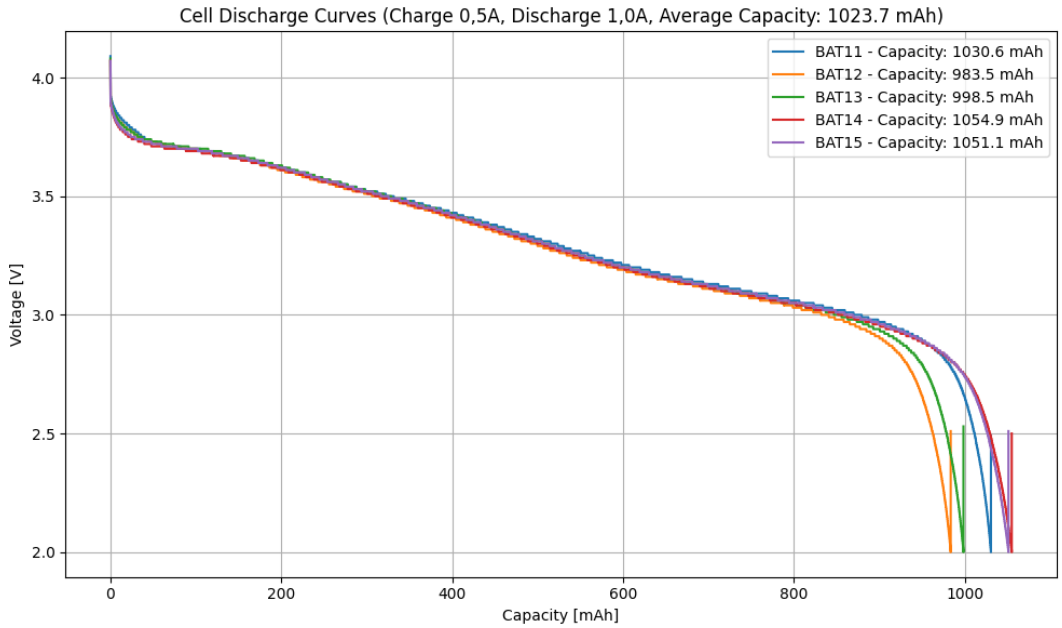

Figure 7.5: Discharge curve of fully charged cells, that charged at 0,5 A and discharged at 1 A. The average capacity of the cells is 1023.7 mAh.

Besides the capacity test, also a 30 days self discharge test is performed. Figure 7.6 Shows the discharge curve of a cell that is first charged with a current of 500 mA, then stored at a temperature of 20 °C for a period of 30 days and finally discharged at 1.0 A. The figure shows that the cell has a capacity of 1112.4 mAh. This means that the capacity of the stored battery is 1.9% higher than the average of the baseline Test A1, subsection 7.1.1. The results of this test suggests that charging the cells with higher currents does not damage the cells short term.

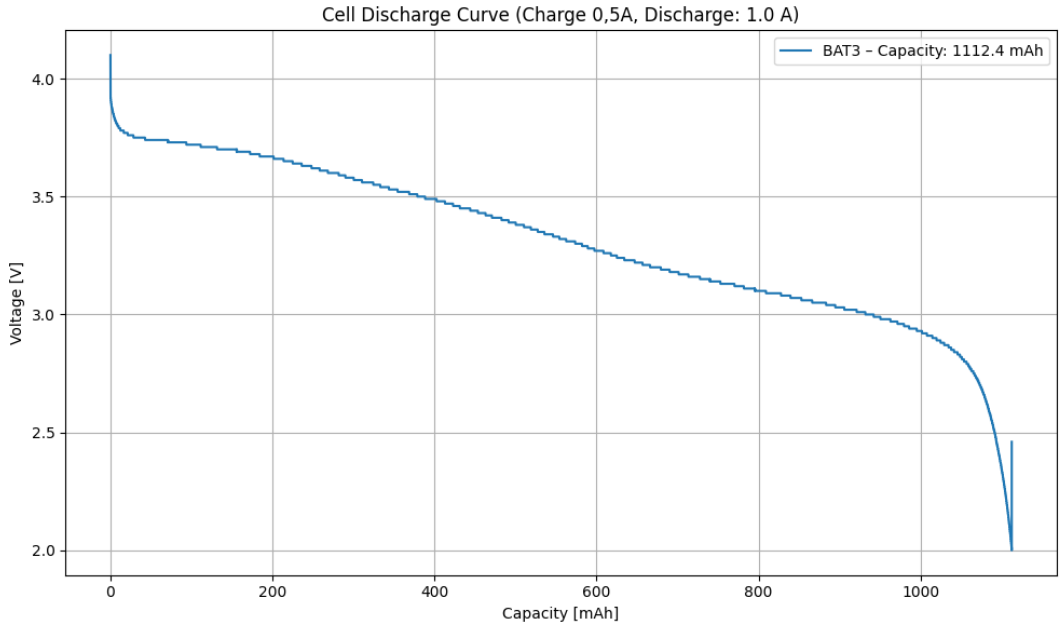

Figure 7.6: Discharge curve of a fully charged cell, that charged at 0,5 A, stored for 30 days and then discharged at 1 A.

7.2 BMS validation

7.2.1 Current Control

In Subsection 5.1.4, it is discussed that the interpretation of the I^{2}C registers *0x32–0x33*, as described in the datasheet of the BQ76920 [7], is incorrect. In Figure 7.7, the black dots represent the measured current for each decimal CC_{raw} value. These values were accurately measured using a current-limited digital power supply. The terminals of the BMS board were connected to this power supply. The voltage was set to 23 V, and the current limit was set to the desired measurement value. Since the batteries operate at a lower voltage than 23 V, they charge at the maximum allowed current. In this setup, the maximum allowed current is accurately known by reading from the power supply. The blue line shows the proposed Equation 5.2 from the BQ76920 datasheet [7]. It can be seen that the blue line does not align correctly with the measured values. The calibrated conversion Equation 5.4, shown in yellow, aligns correctly.

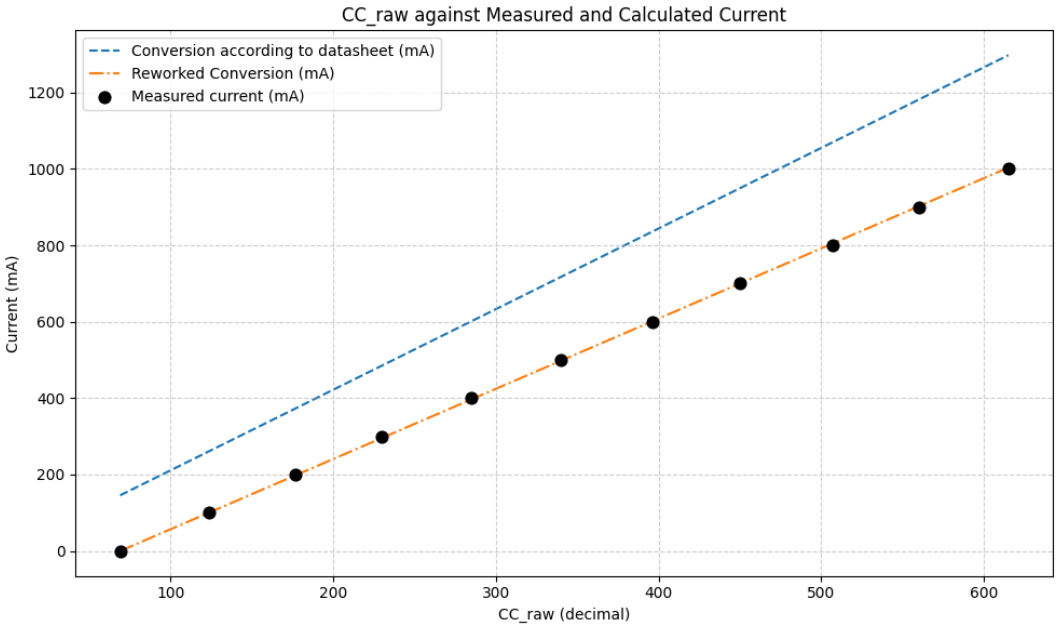

Figure 7.7: The proposed and re-calibrated current control equations.

7.2.2 Overvoltage protection

To verify the correct operation of the overvoltage protection, the overvoltage protection test described in Subsection 6.2.1 is performed. Figure 7.13 shows the individual cell voltages during charging of the battery pack. At $t = 33996$ s, cell BAT7 reaches the 4.2 V threshold. At this point, the BMS interrupts the charging current. After the current is cut off, the cell voltages settle and drop slightly, which is expected behavior.

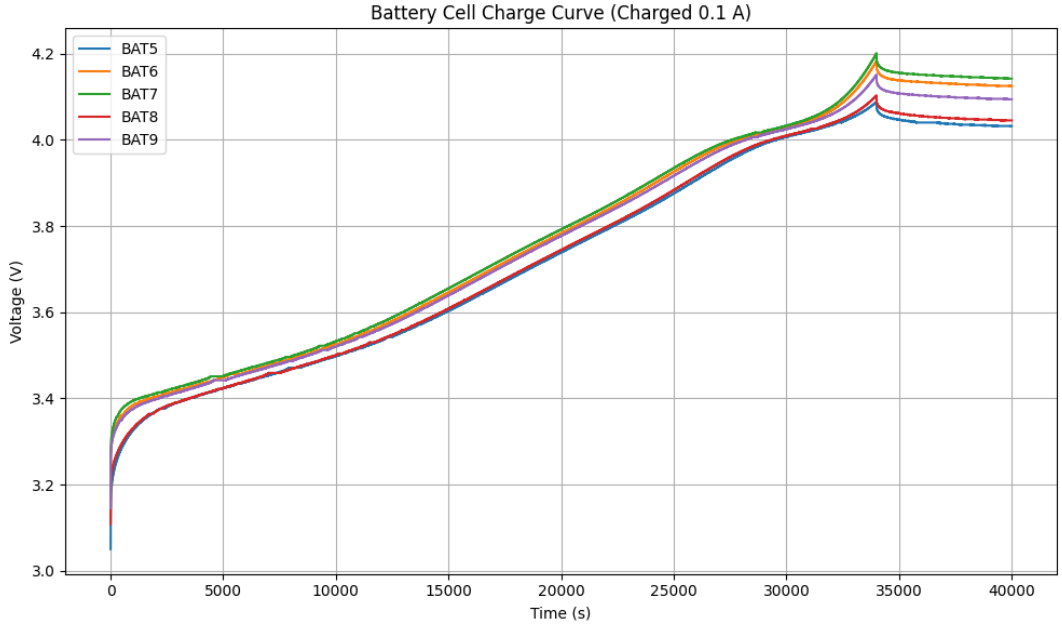

Figure 7.8: Battery pack charged with with BMS. When Cell BAT7 reaches the 4.2 V threshold the systems overvoltage protection kicks in.

In addition to the voltage measurements, the UART logs are used to verify system behavior. The BQ76920 reports its status over the I^2C interface to the microcontroller, which forwards the data to a laptop via UART. Figure 7.9 shows a piece of these logs. When the overvoltage threshold is reached, an *OV Fault* message is reported. Both the voltage measurements in Figure 7.13 and the UART log in Figure 7.9 confirm the correct operation of the overvoltage protection.

```
1  System Status (0x00): 0x80
2  System CTRL1 (0x04): 0x10
3  System CTRL2 (0x05): 0x41
4  4.134 V, 4.189 V, 4.200 V, 4.144 V, 4.180 V, 0.100 A, 16
5  System Status (0x00): 0x80
6  System CTRL1 (0x04): 0x10
7  System CTRL2 (0x05): 0x41
8  4.134 V, 4.190 V, 4.200 V, 4.145 V, 4.180 V, 0.100 A, 16
9  System Status (0x00): 0x80
10 System CTRL1 (0x04): 0x10
11 System CTRL2 (0x05): 0x41
12 4.134 V, 4.190 V, 4.201 V, 4.145 V, 4.181 V, 0.099 A, 16
13 System Status (0x00): 0x84
14 OV fault
15 System CTRL1 (0x04): 0x10
16 System CTRL2 (0x05): 0x40
17 4.085 V, 4.140 V, 4.150 V, 4.095 V, 4.131 V, -0.009 A, 00
```

Figure 7.9: Short section of the UART log, showing on line 14 the OV Fault code.

7.2.3 Undervoltage protection

The results of the undervoltage protection test described in Subsection 6.2.2 are presented in this subsection. Figure 7.10 shows the battery pack voltage measured by the electronic load. At $t = 3556$, a sudden voltage drop is visible. This occurs when the BMS opens the circuit after one of the cells drops

below the undervoltage threshold of 2.1 V. Figure 7.11 shows the individual cell voltages during the same test. Cell BAT8 is the first to reach the 2.1 V threshold, which triggers the undervoltage protection.

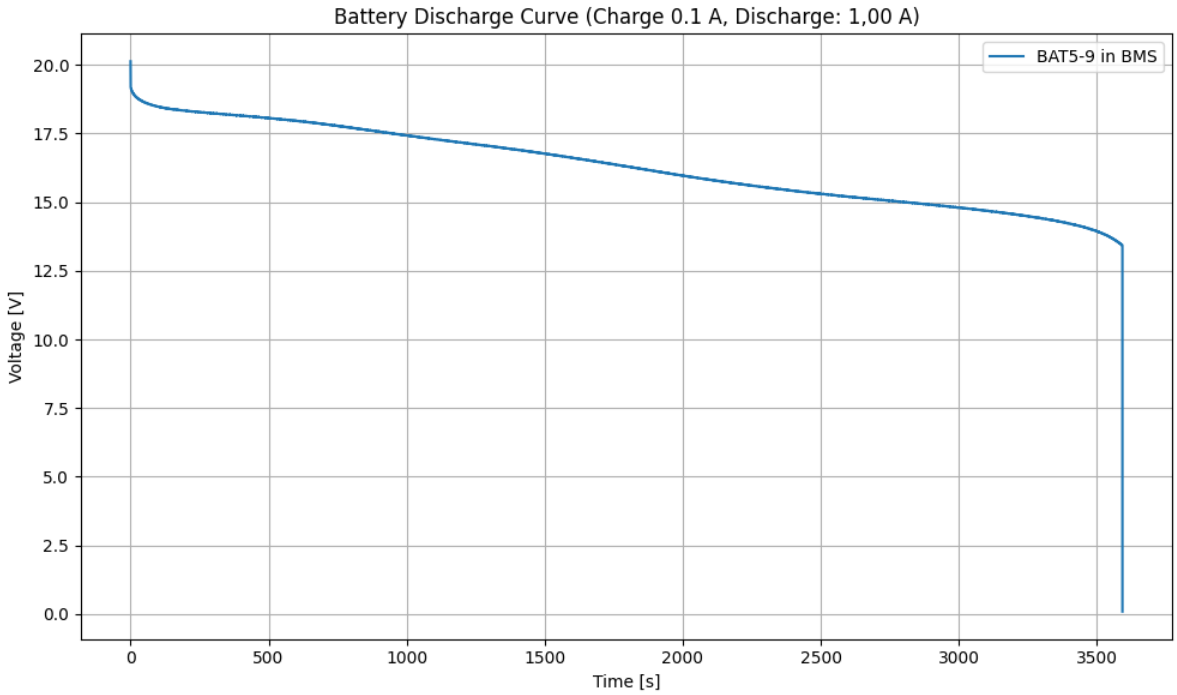

Figure 7.10: Voltage measured over time at the output of the BMS during discharge at 1 A.

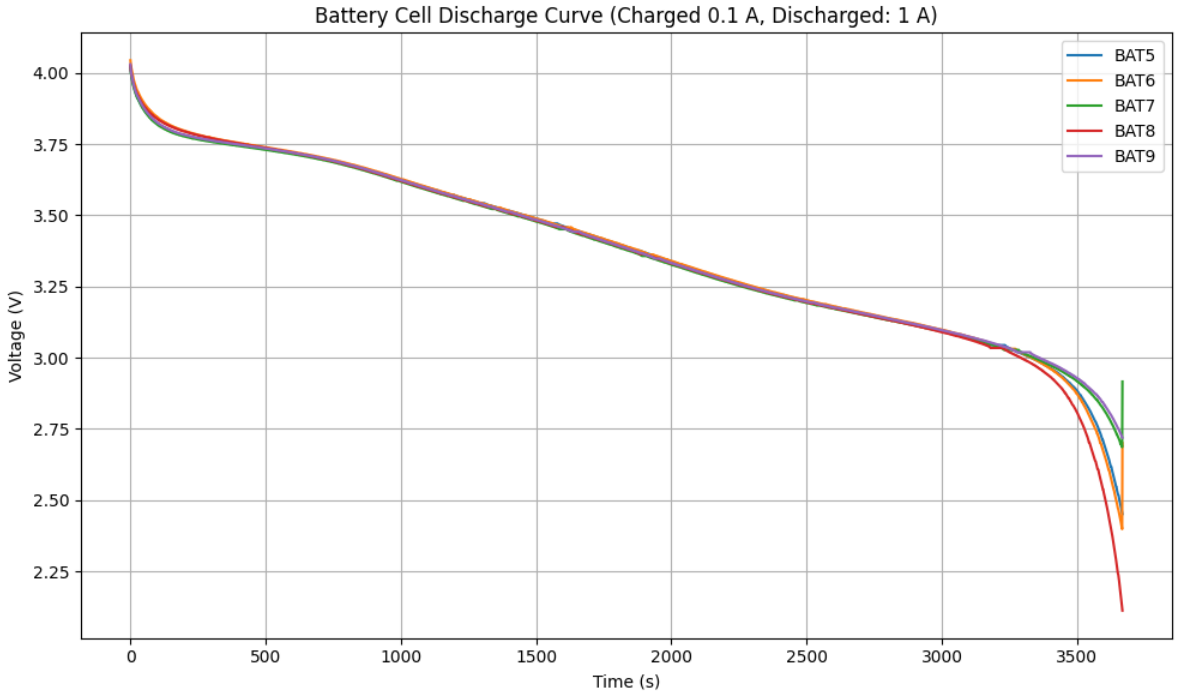

Figure 7.11: Voltage measured over time at the output of every cell.

In addition to the voltage measurements, the UART logs are used to verify the system behavior.

The BQ76920 reports its status over the I^2C interface to the microcontroller, which forwards the data to a laptop via UART. Figure 7.12 shows a section of these logs. Once the 2.1 V threshold is reached, an *UV Fault* message is reported. Both figures and the log confirms the correct behaviour when a cell reaches the undervoltage benchmark.

```
1  System Status (0x00): 0x80
2  System CTRL1 (0x04): 0x10
3  System CTRL2 (0x05): 0x42
4  2.460 V, 2.404 V, 2.689 V, 2.130 V, 2.722 V,   1 .018 A, 00
5  System Status (0x00): 0x80
6  System CTRL1 (0x04): 0x10
7  System CTRL2 (0x05): 0x42
8  2.456 V, 2.398 V, 2.686 V, 2.121 V, 2.721 V,   1 .020 A, 00
9  System Status (0x00): 0x80
10 System CTRL1 (0x04): 0x10
11 System CTRL2 (0x05): 0x42
12 2.451 V, 2.700 V, 2.916 V, 2.112 V, 2.719 V,   1 .018 A, 00
13 System Status (0x00): 0x88
14 UV fault
15 System CTRL1 (0x04): 0x10
16 System CTRL2 (0x05): 0x42
17 2.916 V, 2.901 V, 2.987 V, 2.788 V, 2.994 V,   0 .003 A, 00
```

Figure 7.12: Short section of the UART log, showing on line 14 the UV Fault code.

7.2.4 Overcurrent protection

As described in Subsection 6.2.3, the overcurrent protection is tested by bypassing the rest of the circuit and forcing a current only through the shunt resistor on the board. This causes the on-chip ADC to measure a current as if it were flowing through the battery pack, while in reality the current flows solely through the shunt resistor, thereby protecting the batteries. Due to the low update rate of the UART connection, the exact reaction time of the protection mechanism cannot be measured with this setup. The test therefore only verifies whether the correct fault code is triggered at the expected current level. Table 7.2 shows the fault code results for a 0.5 s current pulse. It can be seen that from 5.4 A onward, the BQ76920 raises the *OCD fault* flag. In Appendix D.0.1, another example is shown where the *OCD fault* flag is raised.

Current	**Fault Code**
5.0 A	-
5.1 A	-
5.2 A	-
5.3 A	-
5.4 A	OCD fault
5.5 A	OCD fault
5.6 A	OCD fault

Table 7.2: Different current levels that flow through the shunt resistor to force a fault flag from the BQ76920 chip. From 5.4 A the *OCD fault* is raised.

7.2.5 Shortcircuit protection

The short-circuit protection test is performed in the same way as the overcurrent protection test described in Subsection 7.2.4. The only difference is that a higher current is applied, which bypasses the rest of the circuit and flows only through the shunt resistor. As described in Subsection 6.2.4, the short-circuit protection is configured to trigger at a current of 9.6 A. As in the overcurrent test, the reaction time

cannot be measured due to the low UART update rate. The test is therefore limited to verifying the raised fault flag. Table 7.3 shows that from a current of 9.6 A onward, the *SCD fault* flag is raised instead of the *OCD fault* flag. In Appendix D.0.1, another example is shown where the *SCD fault* flag is raised.

Current	**Fault Code**
9.1 A	OCD fault
9.2 A	OCD fault
9.3 A	OCD fault
9.4 A	OCD fault
9.5 A	OCD fault
9.6 A	SCD fault
9.7 A	SCD fault

Table 7.3: Different current levels that flow through the shunt resistor to force a fault flag from the BQ76920 chip. From 9.6 A the *SCD fault* is raised.

7.2.6 Cell Balancing

Cell Balancing At Nominal Charging Current (0.1 A)

In Subsection 6.2.5, the test used to measure the impact of the bleeding algorithm is described. Two tests are performed. In the first test, the battery pack is charged via the BMS with the bleeding algorithm disabled. In the second test, the same setup is used, but the bleeding algorithm is enabled.

For the first test, Figure 7.13 shows the complete charging curve of the battery pack containing cells BAT5 up to BAT9. Figure 7.14 shows a detailed view of the final charging stage. It can be seen that all cells continue charging without intervention from the BMS. Cell 7 reaches the 4.2 V threshold first, after which the BMS interrupts the charging process, while the remaining cells could still have charged further.

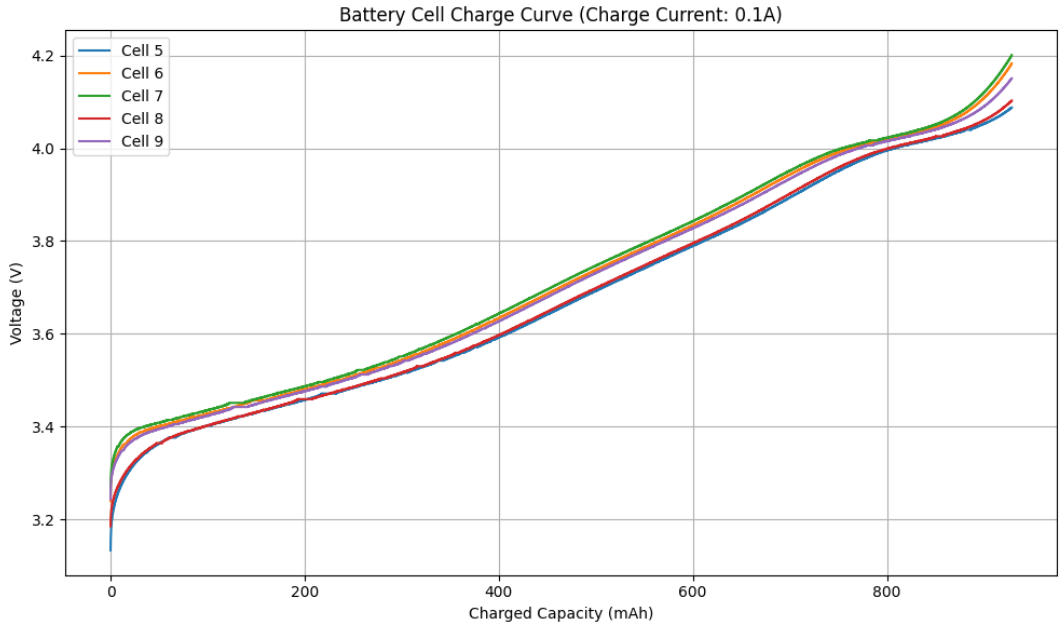

Figure 7.13: Battery pack charged with a current of 0.1 A trough BMS, without the cell balancing algorithm.

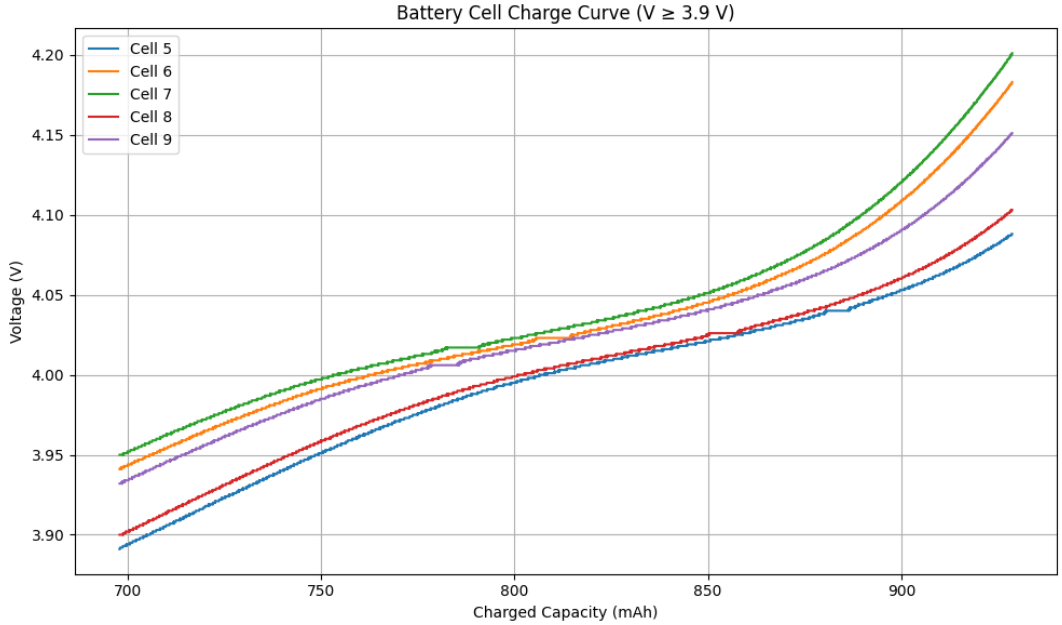

Figure 7.14: Battery pack charged with BMS, without the cell balancing algorithm, zoomed in on where the cell-balancing would have been active.

In the second test, the setup remains unchanged, except that the bleeding algorithm described in Subsection 5.1.3 is enabled. The resulting charging curve is shown in Figure 7.15. Once a cell reaches 4.0 V and exceeds the lowest cell voltage by more than 20 mV, the slope of its charging curve is reduced. Figure 7.16 shows a zoomed-in view of this behavior. It can be seen that, due to the algorithm, higher-voltage cells charge less compared to lower-voltage cells. For completeness, the discharge curves of battery packs charged with and without the bleeding algorithm are provided in Appendix D.0.2.

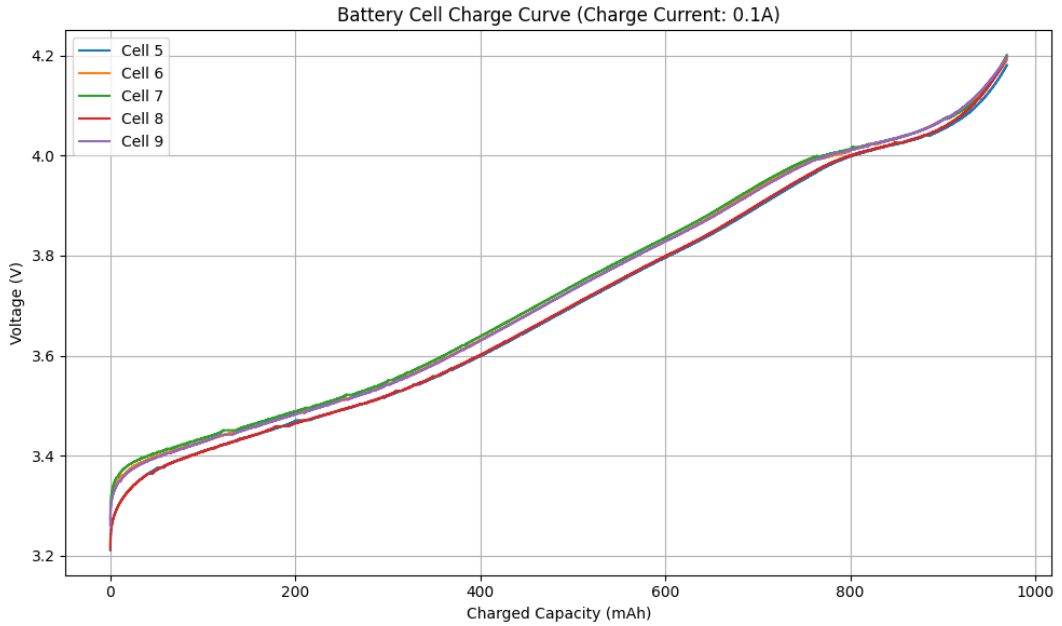

Figure 7.15: Battery pack charged with a current of 0.1 A trough BMS, with cell balancing enabled.

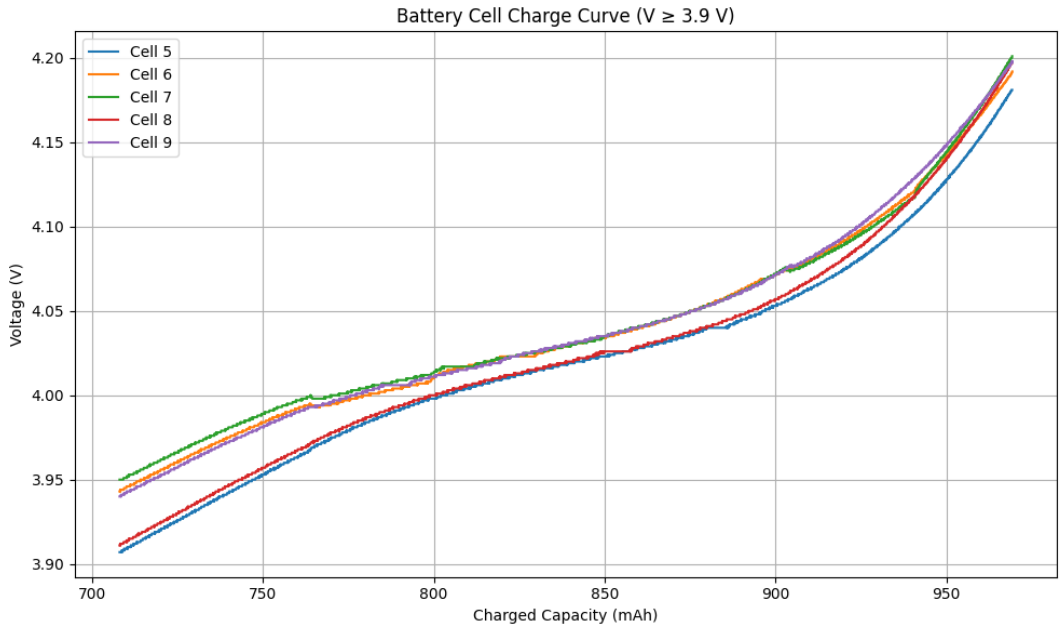

Figure 7.16: Battery pack charged with BMS, with cell balancing enabled, zoomed in the region where the algorithm is active.

Cell Voltage Convergence After Balancing (0.1 A)

The measurements show that when the battery pack is charged with the bleeding algorithm enabled, the cell voltages become more evenly balanced, see Figure 7.17. After this initial charge, the pack was discharged and then charged again under the same conditions. During this second charge cycle, the cell voltages remained close to each other. As a result, the bleeding algorithm was enabled but never activated.

This indicates that the bleeding algorithm improves the voltage balance of the battery pack, reducing the need for further balancing in subsequent charge cycles.

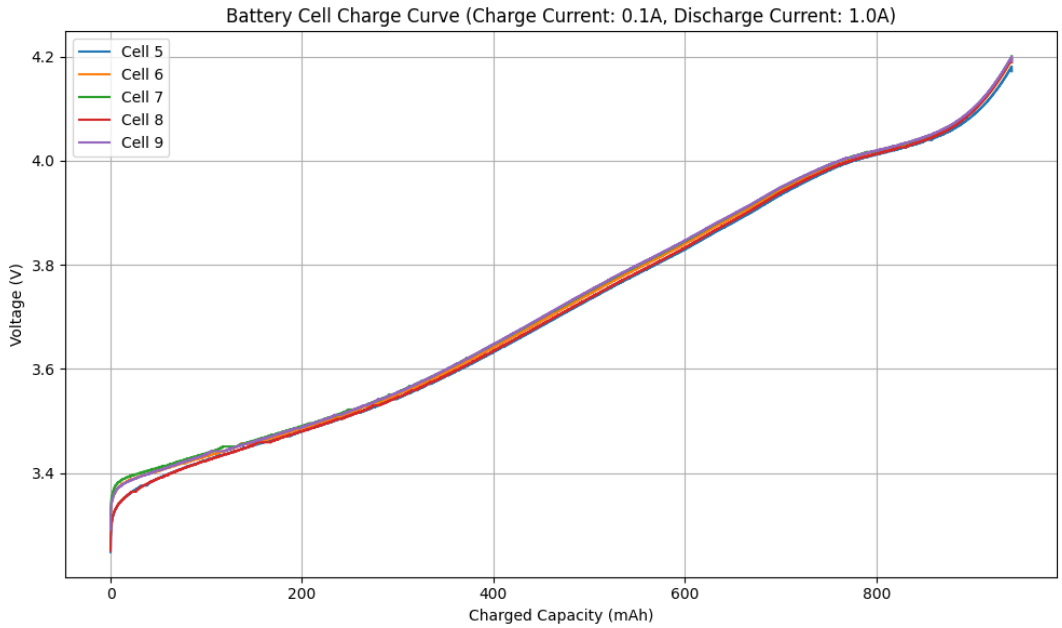

Figure 7.17: Charging the battery pack via the BMS, it can be seen that the bleeding algorithm never needs to activate due to the voltages being very close.

Cell Balancing at Increased Charging Current (0.5 A)

As described in Subsection 6.1.5, exceeding the specified charging current can increase the active operation time of the rover on the Moon. The influence of the bleeding algorithm at these higher charging currents is therefore also investigated, as described in Subsection 6.2.5. The same two tests are performed to evaluate the behavior of the algorithm at increased charging currents.

In the first test, the battery pack is charged at 0.5 A with the bleeding algorithm disabled. Figure 7.18 shows the voltage behavior of the individual cells in the battery pack. Figure 7.19 shows a zoomed-in view of the region where the bleeding algorithm would normally become active.

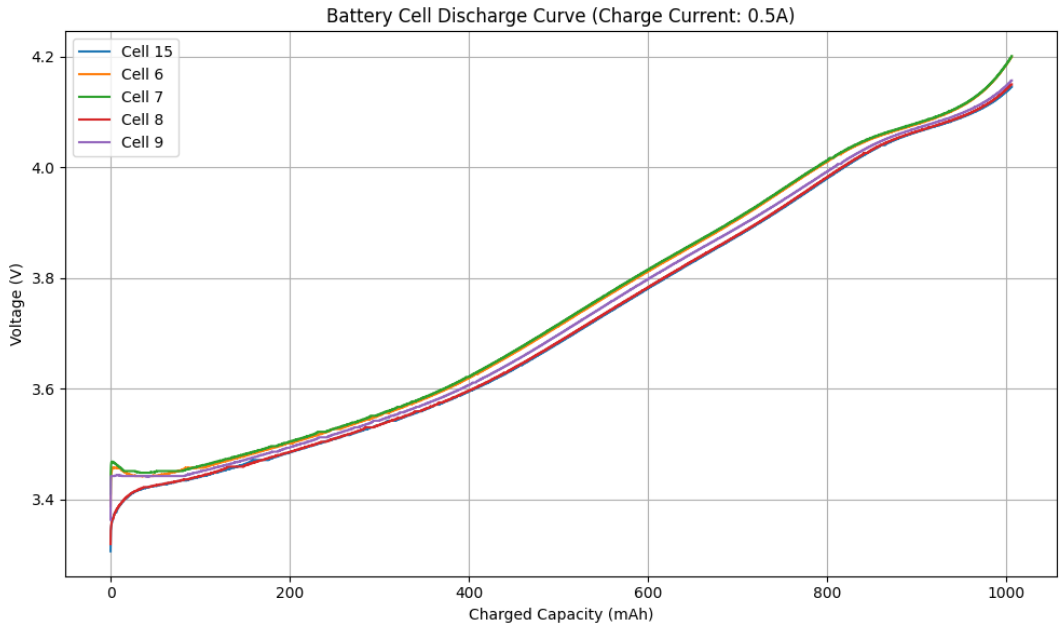

Figure 7.18: Battery pack charged with a current of 0.5 A trough BMS, with cell balancing disabled.

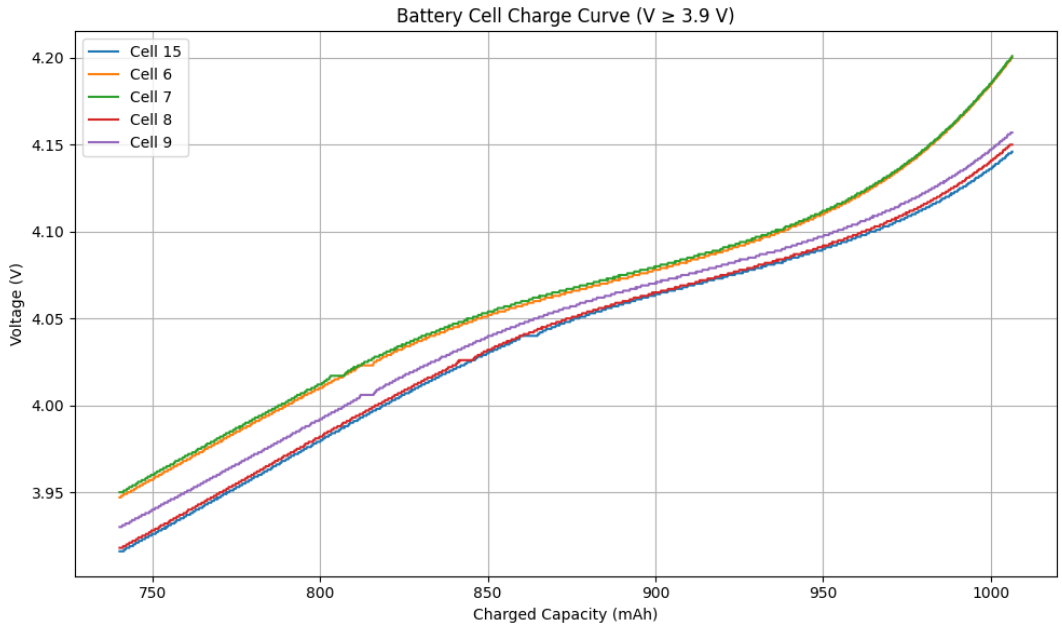

Figure 7.19: Battery pack charged zoomed-in view in the algorithms active region, with cell balancing disabled.

In the second test, the battery pack is again charged at 0.5 A, but this time with the bleeding algorithm enabled. Figure 7.20 shows the voltage behavior of the cells during this test. Figure 7.21 shows a zoomed-in view of the region where the bleeding algorithm is active. When comparing the results of both tests, no clear difference in cell voltage behavior can be observed. At a charging current of 0.5 A, the bleeding algorithm has little to no visible influence on the charging curves. This behavior can be explained by the maximum bleeding current of 70 mA per cell, which is small compared to the applied charging current of 0.5 A.

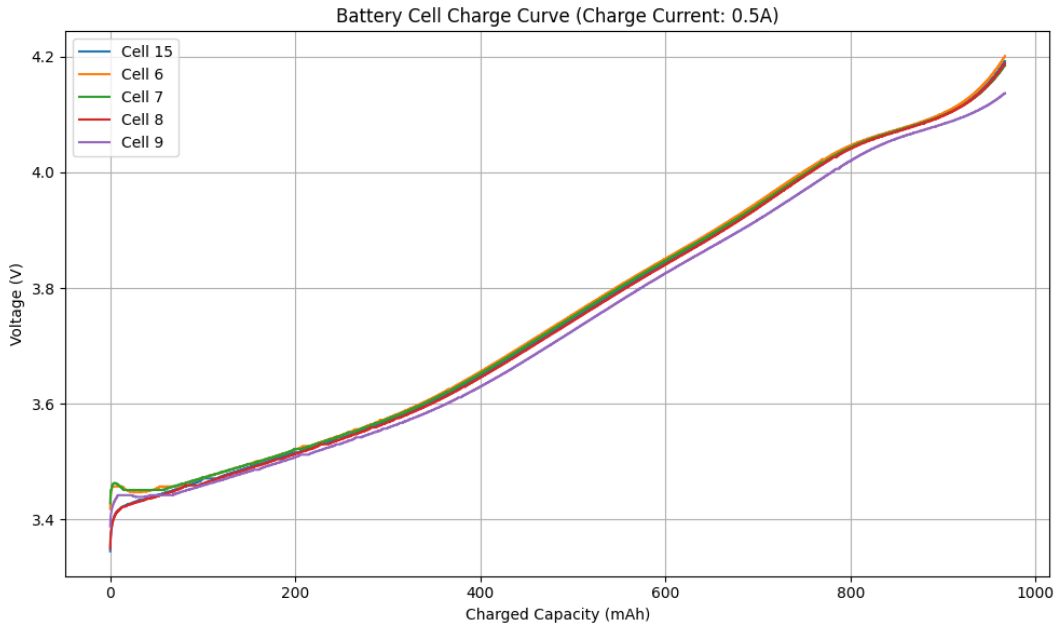

Figure 7.20: Battery pack charged with a current of 0.5 A trough BMS, with cell balancing disabled.

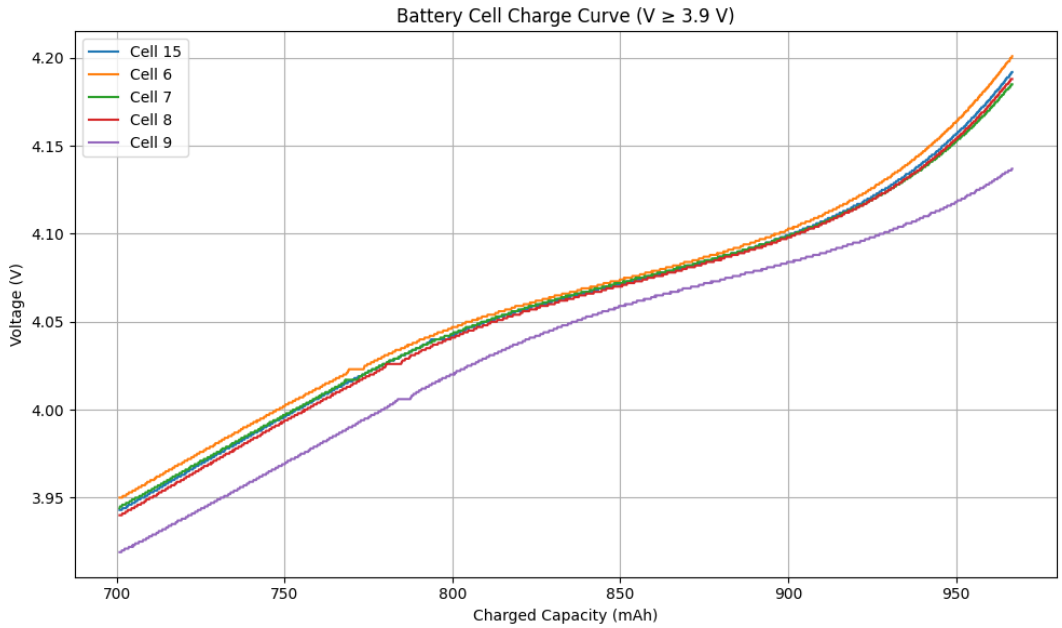

Figure 7.21: Battery pack charged zoomed-in view in the algorithms active region, with cell balancing enabled.

Cell Balancing at Design-Selected Charging Currents (0.5 A into 0.1 A)

The results of the cell balancing algorithm at a charging current of 0.5 A are limited. As discussed in Subsection 7.2.6, the maximum bleeding current of 70 mA is too low to noticeably affect the charging behavior at this current level. In this subsection, an alternative charging strategy is proposed that combines the advantages of both high and low charging currents.

In this approach, the battery pack is initially charged at 0.5 A until the cells reach the voltage region where the balancing algorithm becomes active. Once a predefined threshold voltage is reached, in this case 3.9 V, the charging current is reduced to 0.1 A. Figure 7.22 shows the complete charging curve of the battery pack. Up to 3.9 V, the cells are charged at 0.5 A. When the current is reduced to 0.1 A, a small voltage drop is observed, which is expected. From this point onward, as shown in Figure 7.23, the bleeding algorithm effectively reduces the voltage differences between the cells.

These results indicate that a combined charging strategy can achieve faster charging times while still allowing effective cell balancing near the upper voltage range.

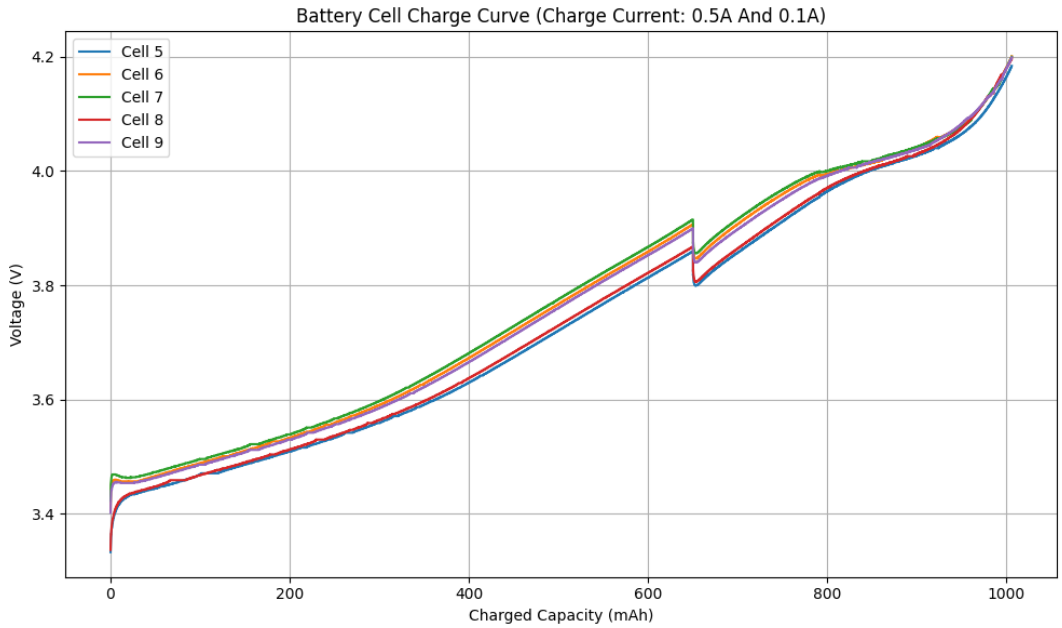

Figure 7.22: Battery pack charged with a strategic current of first 0.5 A and then 0.1A through the BMS, with cell balancing enabled.

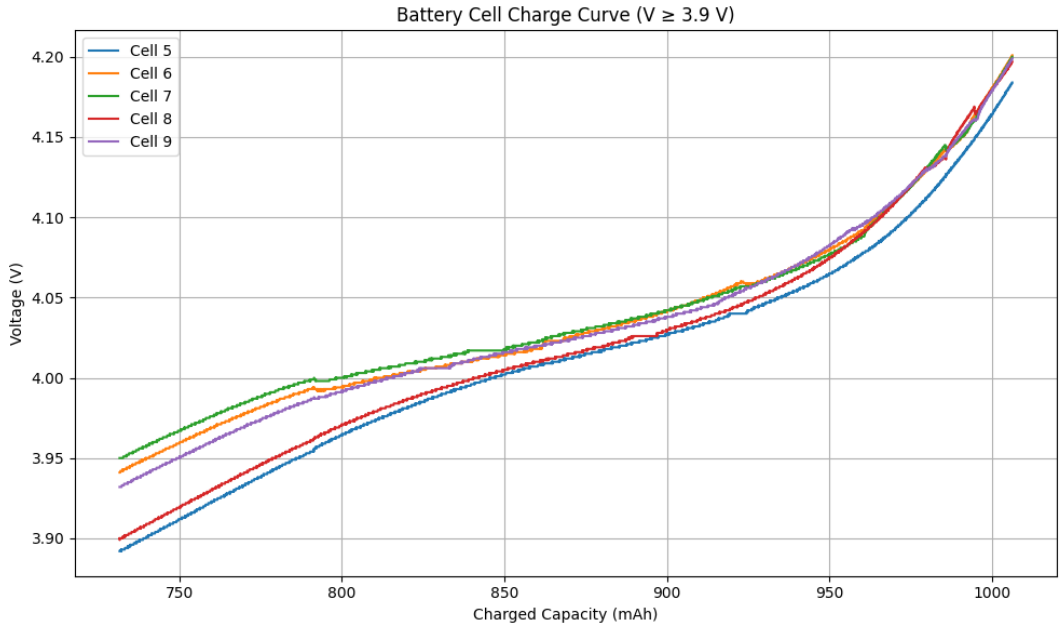

Figure 7.23: Zoomed-in view of the battery pack charged with a strategic current of first 0.5 A and then 0.1A through the BMS, with cell balancing enabled.

Similar to the behavior described in Subsubsection 7.2.6, voltage convergence between the cells is also observed when using the combined charging strategy. After completing the charging test shown in Figure 7.22, the battery pack is discharged at a current of 1.0 A. The same charging strategy is then applied for a second cycle.

During this second charging cycle, the cell voltages remain closely aligned, as also observed in Subsubsection 7.2.6. The bleeding algorithm is enabled but does not activate. Figure 7.24 shows the

charging curves of the individual cells during this second cycle. Compared to the first charging cycle, the voltage spread between the cells is reduced. In the zoomed-in view shown in Figure 7.25, the cells charging above 4.0 V do not exceed a voltage difference of 20 mV. As a result, the bleeding algorithm is not triggered.

This indicates that the combined charging strategy effectively improves cell voltage balance after the initial charge, reducing the need for active balancing in subsequent charge cycles.

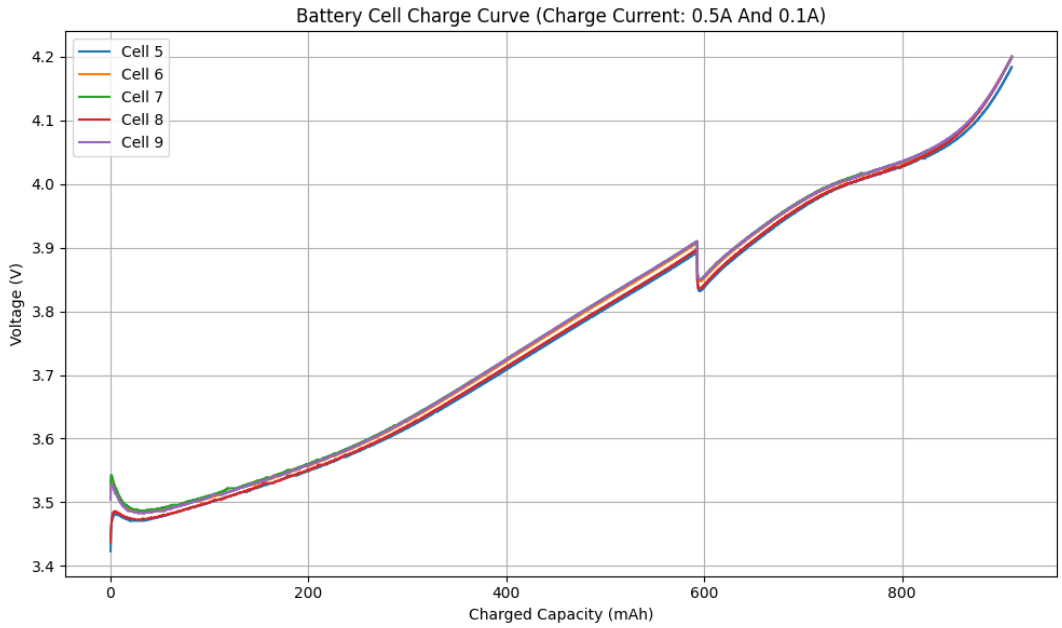

Figure 7.24: Second Charging cycle of Battery pack charged with a strategic current of first 0.5 A and then 0.1A trough the BMS, with cell balancing enabled.

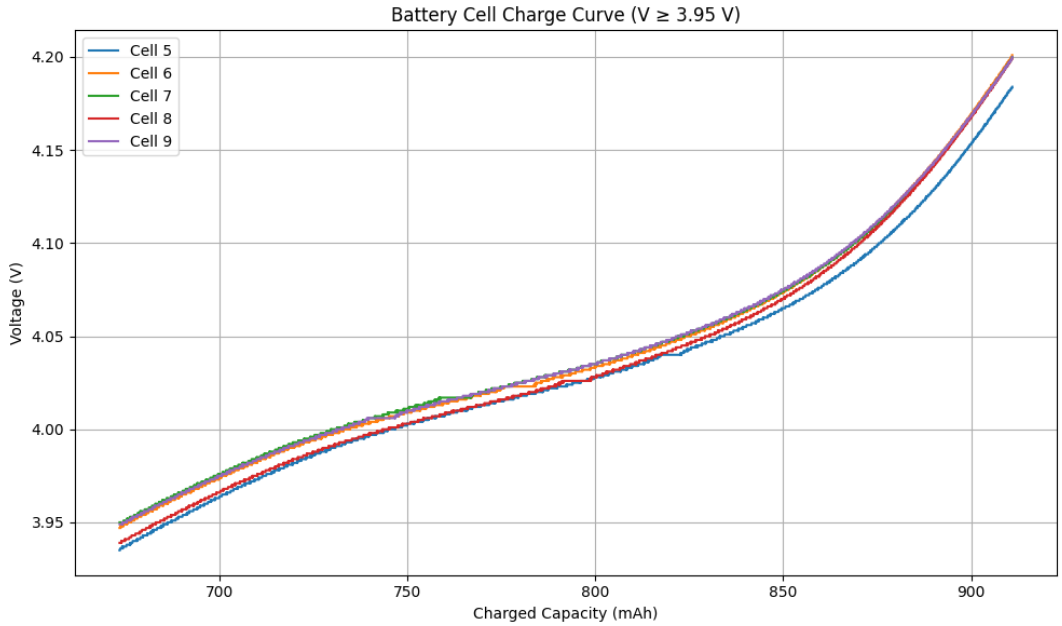

Figure 7.25: Zoomed-in view of Second Charging cycle of the battery pack charged with a strategic current of first 0.5 A and then 0.1A trough the BMS, with cell balancing enabled

7.3 Bidirectional Converter and System Integration

At the outset of this thesis, it was assumed that integrating the bidirectional converter with the BMS and the board developed by Hubers [6] would be relatively straightforward. However, during implementation, it became clear that this integration posed more challenges than expected, requiring additional effort and design iterations. As a result, the outcomes presented in this section reflect the progress that could be achieved within the available timeframe, rather than a fully finalized system.

7.3.1 Voltage Readout

To verify the correct operation of the voltage readout, a series of functional tests was performed. During these tests, known voltage conditions were applied to the converter terminals. The voltages measured by the microcontroller were monitored and compared against the expected values. The resulting power flow direction determined by the algorithm was then observed and verified. In all tested scenarios, the microcontroller correctly identified the measured terminal voltages.

7.3.2 Onboard 5V converter

As mentioned previously, another relatively simple subsystem is the onboard 5 V converter. This converter supplies power to the microcontroller from the 12 V bus. During the test, the microcontroller is powered from a 12 bus via the converter. The whole system functioned as it was expected. Therefore it can be said that this onboard converter is functional.

7.3.3 PWM Generation

In Subsection 6.3.3, the pulse-width modulation (PWM) functionality of the bidirectional converter is verified. Both buck and boost operating modes are tested to confirm correct duty cycle generation. Figure 7.26 shows the PWM signal corresponding to buck operation, where the battery voltage $V_{\text{bat}} = 18$ V is stepped down to the bus voltage $V_{\text{bus}} = 12$ V. The measured duty cycle matches the theoretical value derived for buck operation, confirming correct PWM behaviour in this mode.

$$V_{\text{bus}} = D \cdot V_{\text{bat}} \tag{7.1}$$

$$D = \frac{V_{\text{bus}}}{V_{\text{bat}}} = \frac{12}{18} = 0.67 \tag{7.2}$$

Similarly, Figure 7.27 presents the PWM signal for boost operation, in which the converter raises the bus voltage $V_{\text{bus}} = 12$ V to the battery voltage $V_{\text{bat}} = 18$ V. The observed duty cycle corresponds to the expected value for boost operation. Together, these results demonstrate that the bidirectional converter generates the correct PWM duty cycles when switching between buck and boost modes, validating the implemented control logic and duty cycle calculation.

$$V_{\text{bat}} = \frac{V_{\text{bus}}}{1 - D} \tag{7.3}$$

$$D = 1 - \frac{V_{\text{bus}}}{V_{\text{bat}}} = 1 - \frac{12}{18} = 0.33 \tag{7.4}$$

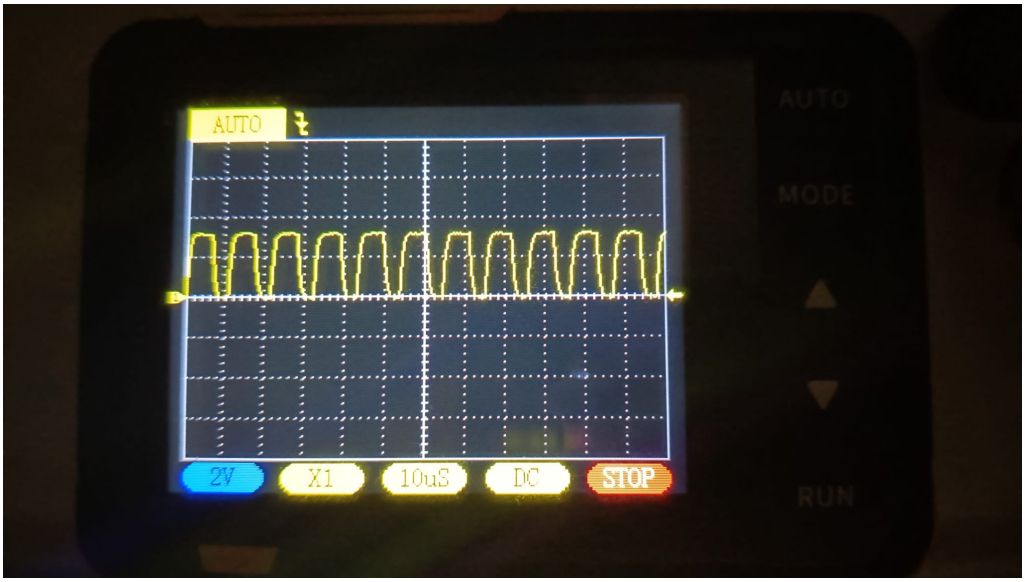

Figure 7.26: When bucking from $V_{bat} = 18$ V to $V_{bus} = 12$ V, the PWM duty cycle is 60%

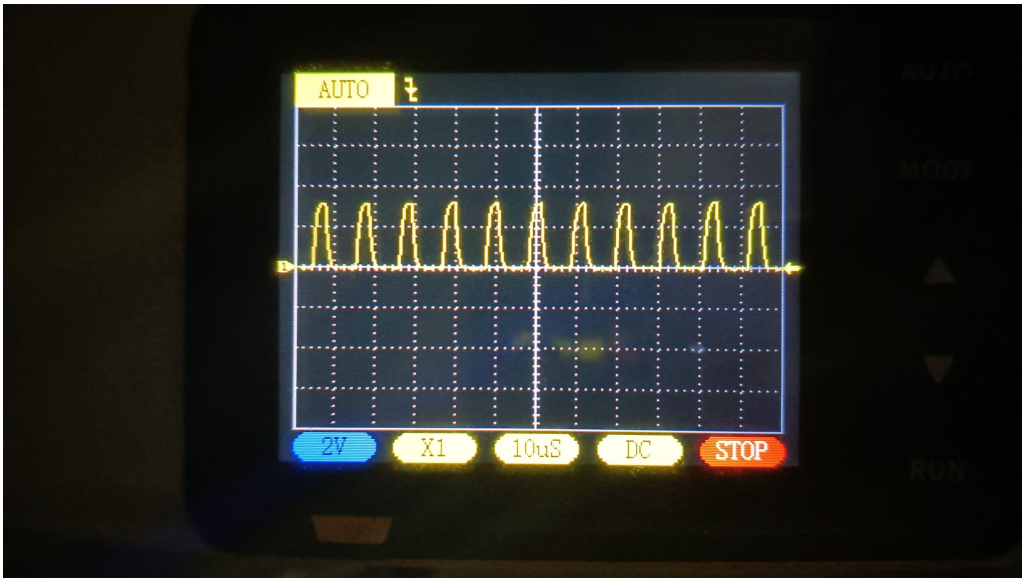

Figure 7.27: When boosting from $V_{bus} = 12$ V to $V_{bat} = 18$ V, the PWM duty cycle is 30%.

7.3.4 Bidirectional Converter Functionality

The integrated functionality test of the bidirectional converter, as described in the testing procedure 6.3.4, was performed using an 18 V input source in buck mode to produce 12 V output. During this test, the converter did not operate as intended and failed to produce an output voltage.

At this stage, the cause of the malfunction is unclear. Potential factors include residual shorts on the PCB, incomplete or incorrect firmware or potential unnoticed damage that could have been created during previous testing. Due to time constraints, further investigation was not possible. Despite this, the test provides useful insight into the current limitations of the converter design and highlights areas requiring additional attention in future iterations.

Chapter 8

Conclusion

The Lunar Zebro Rover seems to be functioning as one big system. A closer examination reveals that the rover consists of different subsystems, each with its own power requirements. To ensure the reliable operation of these subsystems, the rover is equipped with a dedicated Electrical Power System. T This system is responsible for distributing electrical power throughout the rover, while continuously monitoring the remaining energy stored in the battery pack. The EPS also manages the charging and discharging processes to maintain stable and efficient operation under varying load conditions. While continuously monitoring the safe operating condition of each cell.

Before this work, the battery cells intended for the Lunar Zebro rover had not yet been verified for their suitability for the mission. In this thesis, these cells are tested and evaluated to determine whether they can reliably be used in the battery pack. This validation makes it possible to state with more confidence that the battery pack will be able to survive the lunar mission. In addition, a better understanding of the cell behavior makes the performance of the battery pack more predictable, which increases the chance of mission success.

The approach followed in this thesis is based on systems engineering. Working in this way helps to identify and mitigate potential mission-ending failures at an early stage. The lunar environment is harsh and significantly different from that on Earth. By defining clear requirements, these challenging conditions are categorized, making it possible to design the system with them in mind.

This thesis aimed to design, validate, and integrate a reliable BMS and battery pack into the previously designed EPS. It is written in such a way that, after completion, the Lunar Zebro team can build on the findings presented here and further iterate on the development of the EPS.

8.1 Reliable BMS Design and Validation

In this Section the first research question is concluded. The question is stated as: How can a reliable battery management system be designed and validated for the Lunar Zebro rover operating in the lunar environment?

Reliability is supported by several factors. First, the use of TLI-1550ES batteries contributes significantly to it. These cells have been thoroughly tested and shown to be reliable for the entire lunar mission. They also operate across a wide temperature range, which is crucial for the extreme conditions on the Moon. In addition to the batteries themselves, the BQ76920 battery management IC adds to the Rover's reliability. This chip includes features such as a CRC byte, overvoltage (OV), undervoltage (UV), overcurrent discharge (OCD) and short circuit discharge (SCD) protection, as well as an accurate current sensor and the ability to bleed individual cells.

The reliable system is designed to be modular, meaning each subsection has its own PCB. Although the final Rover will not use this modular approach, it is very useful for testing. It makes debugging simpler and allows easy replacement if something stops working.

8.2 Battery Behaviour During the Mission

The second research question will be answered in this section. The question is stated as: How does the battery pack behave under different operating conditions over the full duration of the first Lunar Zebro mission?

The battery pack behaves differently under various conditions. Wherever possible, tests were carried out for all expected situations. These tests provide a complete understanding of how the cells perform. By simulating the entire system, it was checked whether the battery pack can supply enough power for the system to operate. The simulation confirmed that the TLI-1550ES is the best choice for the battery pack out of all the Tadiran options. Besides simulations, physical tests were also done to study battery characterization, capacity, internal resistance, self-discharge, and charging currents beyond the datasheet limits.

All these tests together showed that the TLI-1550ES is a suitable battery for the mission. During the trip to the Moon, the battery is barely damaged. With heavy use, the state of health (SOH) of the cells drops to 80% only when charged at more than three times the recommended current. This suggests that at a lower charging current of 0.1 A, the SOH will remain at least 80%, likely closer to 96–99%. In a setup with 15 TLI-1550ES batteries, charging at the maximum allowed current for five and a half minutes would power the rover for one minute. This demonstrates that the battery pack is well-suited to meet the demands of the mission.

8.3 Integration into the EPS

The final research question is stated as: How can the newly designed BMS and validated battery pack be integrated into the existing EPS of the Lunar Zebro rover?

Previous versions of the EPS were functional but lacked a battery management system (BMS) and a validated battery pack. The earlier EPS design was cramped, leaving little space for debugging. The advantage of that design was that it fit directly into the rover. However, The BMS was created with modularity in mind. Instead of being integrated into the existing EPS design, it is made as a separate module that can be added to the system. Because of this, the updated EPS does not change much from the previous version, aside from adding the new components. It also makes the subcomponents of the existing EPS modular and easier to work with. For example, the previously designed bidirectional converter is now its own modular component. This modular approach not only makes debugging easier for anyone working on this component, but also helps future team members maintain the EPS. Each component can be removed, modified, and reinstalled without affecting the entire system. Once prototyping is complete, everything can be reassembled into a final version for the Rover.

Now that all subcomponents of the EPS are modular, the microcontroller can control not only the bidirectional converter but also the BMS at the same time. The BMS and bidirectional converter can work together through a single microcontroller to manage the current flow properly. This allows the newly designed BMS to be integrated into the existing EPS. In the future, adding extra parts to the EPS should be easier because of this modular approach.

8.4 Overall Contribution to Lunar Zebro

This section highlights the contributions of this thesis to the Lunar Zebro Project. The Rover now has a validated battery pack and a BMS that helps protect the batteries and other subsystems. These additions improve the overall reliability of the Rover and help prepare it for possible faults. The Energy Power Budget simulator provides useful insights for team members, helping them understand how their subsystems impact the energy budget. This information can support informed design decisions. The modular redesign of the EPS makes prototyping easier by simplifying debugging and component replacement. Additionally, requirements for the EPS and other subsystems were established in collaboration with the system engineers, helping to guide future development.

8.5 Limitations and Future work

In addition to the results presented in this thesis, there are several areas that remain to be addressed in future work. Due to limited measurement equipment, the TLI-1550ES battery cells could not be tested in a thermal vacuum under the extreme temperatures expected on the lunar surface. Similarly, radiation testing was not possible. Since the Rover is still under development, battery tests were limited to laboratory conditions. These additional tests should be carried out in future phases of the project.

The full integration of the BMS within the EPS is also not yet complete. This is mainly due to issues with the bidirectional converter. Debugging and finalizing this component fall outside the scope of this thesis, but represent an important next step for continued development.

Bibliography

[1] ABRA Electronics. *638354 170 RPM Econ Gear Motor [Product page].* https://abra-electronics.com/robotics-actobotics-servocity/motion-en/dc-gear-motors-brushed/econ-spur-gear-motors/638354-170-rpm-econ-gear-motor.html. Accessed: 2025-10-01. n.d.

[2] AZUR SPACE Solar Power GmbH. *30% Triple Junction GaAs Solar Cell Assembly: Type TJ Solar Cell Assembly 3G30A*. DB 0003401-01-01. Heilbronn, Germany, 2016.

[3] R. C. Baumann. "Radiation-induced soft errors in advanced semiconductor technologies". In: *IEEE Transactions on Device and Materials Reliability* 5.3 (2005), pp. 305–316. DOI: 10.1109/TDMR.2005.853449.

[4] Franklin Josue Ticona Coaquira et al. "Model-Based Design and Testbed for CubeSat Attitude Determination and Control System with Magnetic Actuation". In: *Applied Sciences* 14.14 (2024), p. 6065. DOI: 10.3390/app14146065. URL: https://www.mdpi.com/2076-3417/14/14/6065.

[5] Martijn Hubers, Mladen Gagic, and Aditya Shekhar. "Lunar Rover Power Electronic System". In: *Proceedings of the IECON 2023 – 49th Annual Conference of the IEEE Industrial Electronics Society*. IEEE, 2023. DOI: 10.1109/IECON51785.2023.10312700. URL: https://doi.org/10.1109/IECON51785.2023.10312700.

[6] Martijn D. Hubers. "Design and Implementation of the Power Electronic System for the Lunar Zebro Rover". MSc thesis. Delft, The Netherlands: Delft University of Technology, 2023. URL: http://repository.tudelft.nl/.

[7] Texas Instruments Incorporated. *BQ769x0 3-Series to 15-Series Cell Battery Monitor Family for Li-Ion and Li-Phosphate Applications (Data Sheet)*. https://www.ti.com/lit/ds/symlink/bq76940.pdf. Rev. I; features CRC in digital interface. 2022.

[8] Samppa Jenu et al. "State of health estimation of cycle aged large format lithium-ion cells based on partial charging". In: *Journal of Energy Storage* 46 (2022), p. 103855. DOI: 10.1016/j.est.2021.103855.

[9] NASA Jet Propulsion Laboratory. *Risk-Aware Planetary Rover Operation: Autonomous Terrain Classification and Path Planning*. Tech. rep. Jet Propulsion Laboratory, California Institute of Technology, 2016. URL: https://ntrs.nasa.gov/citations/20160008261.

[10] Musong L. Katche et al. "A Comprehensive Review of Maximum Power Point Tracking (MPPT) Techniques Used in Solar PV Systems". In: *Energies* 16.5 (2023), p. 2206. DOI: 10.3390/en16052206.

[11] Chunlai Li, Xiaodong Zhang, Lihua Meng, et al. "Nature of the lunar far-side samples returned by the Chang'e-6 mission". In: *Science* 384.6692 (2024), pp. 1123–1127. DOI: 10.1126/science.adt1093. URL: https://www.science.org/doi/10.1126/science.adt1093.

[12] Wei Li, Peng Zhang, and Hong Chen. "Recent advances in fast-charging lithium-ion batteries: Mechanism, materials, and future opportunities". In: *Chemical Engineering Journal* 490 (2025), p. 150726. DOI: 10.1016/j.cej.2025.150726. URL: https://doi.org/10.1016/j.cej.2025.150726.

[13] Paul Madle. *STM32H7 Radiation Test Report*. Version 01. Licensed under CC BY-SA 4.0. Open Source Satellite, 2021. URL: https://www.opensourcesatellite.org/.

[14] Sara Fouad Mohamed et al. "Design and Implementation of an ADCS for a CubeSat". In: *Journal of Engineering Research* 7.2 (2023), Article 28. DOI: 10.21608/ERJENG.2023.197719.1160. URL: https://digitalcommons.aaru.edu.jo/erjeng/vol7/iss2/28.

[15] NASA. *Artemis – Why We Are Going to the Moon*. Accessed: 2025-10-27. 2025. URL: https://www.nasa.gov/humans-in-space/artemis.

[16] NASA. *How long does it take to get to the Moon?* Accessed: 29 October 2025. 2022. URL: https://moon.nasa.gov/resources/367/how-long-does-it-take-to-get-to-the-moon/.

[17] NASA. *Moon facts*. Accessed: 2025-10-27. 2024. URL: https://science.nasa.gov/moon/facts/.

[18] Dongxu Ouyang et al. "Investigation of a commercial lithium-ion battery under overcharge and over-discharge failure conditions". In: *RSC Advances* 8.60 (2018), pp. 33407–33418. DOI: 10.1039/C8RA05564E.

[19] STMicroelectronics. *STM32 Nucleo-64 Boards (NUCLEO-xxxxCx, NUCLEO-xxxxRx, NUCLEO-xxxxRx-P, NUCLEO-xxxxRx-Q): Data Brief*. Tech. rep. DB2196 Rev. 21. STMicroelectronics, Jan. 2025. URL: https://www.st.com/resource/en/data_brief/db2196.pdf.

[20] Tadiran Batteries Ltd. *TLI-1550ES Rechargeable Lithium-Thionyl Chloride Cell Datasheet*. Tadiran Batteries Ltd. Kiryat Ekron, Israel, 2023. URL: https://www.tadiranbat.com.

[21] J. M. Tejeda et al. "The complete set of thermo-mechanical-radiation methods, simulations and results for a swarm of nanorovers deployed on the Moon's surface (Lunar Zebro Mission)". In: *Advances in Astronautics Science and Technology* 5 (2022), 317–334. DOI: 10.1007/s42423-022-00115-7. URL: https://link.springer.com/article/10.1007/s42423-022-00115-7.

[22] U.S. Air Force Space and Missile Systems Center. *SMC-S-007: Electrical Power Systems – Batteries, Cells, and Battery Management*. Tech. rep. Available via program document repository. El Segundo, CA, USA: Space and Missile Systems Center, 2020.

[23] U.S. Air Force Space and Missile Systems Center. *SMC-S-018: Lithium-Ion Battery Safety and Abuse Test Requirements*. Tech. rep. El Segundo, CA, USA: Space and Missile Systems Center, 2021.

[24] Rui Zhang and Jie Chen. "A review of improvements on electric vehicle battery technologies". In: *Heliyon* 10.2 (2024), e18377. DOI: 10.1016/j.heliyon.2024.e18377. URL: https://doi.org/10.1016/j.heliyon.2024.e18377.

[25] Shuhong Zhao et al. "A measurement method for determination of DC internal resistance of batteries and supercapacitors". In: *Electrochemistry Communications* 12.2 (2010), pp. 242–245. DOI: 10.1016/j.elecom.2009.12.004. URL: https://doi.org/10.1016/j.elecom.2009.12.004.

Appendices

Appendix A

Simulator

A.1 Energy plots of the simulated batteries from Tadiran

In this section, the corresponding energy plots are presented that correspond with the figures from section 4.2. The figures can facilitate as a supporting figure to verify the claims made in that section.

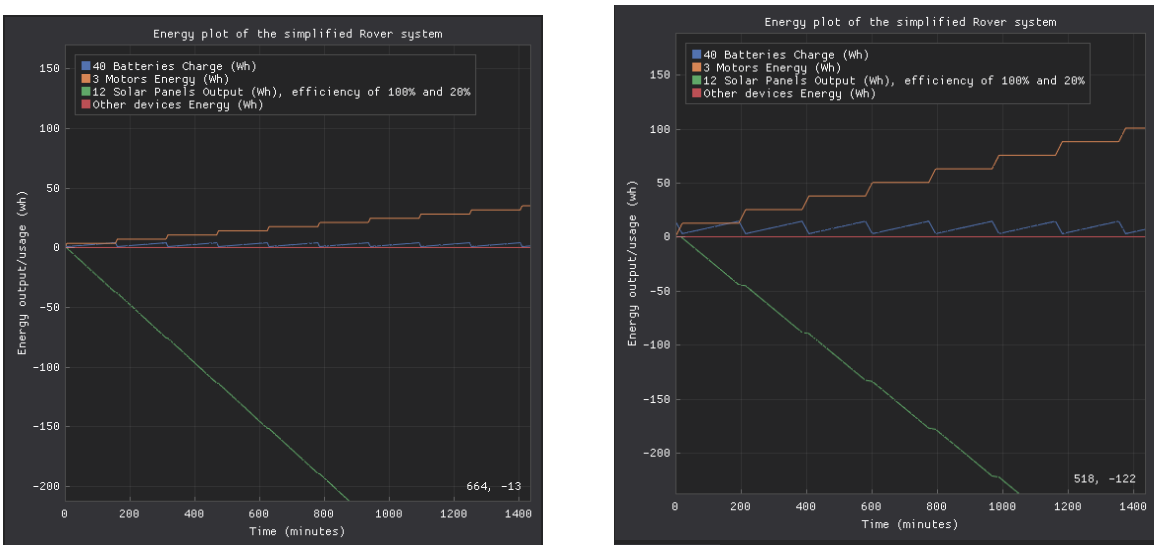

(a) (b)

Figure A.1: (a.) 40 TLI-1020A batteries in the energy budget simulator showing a charge-to-walk ratio of 25.93 minutes to 1 minute (b.) 40 TLI-1550A batteries in the energy budget simulator showing a charge-to-walk ratio of 4.12 minutes to 1 minute.

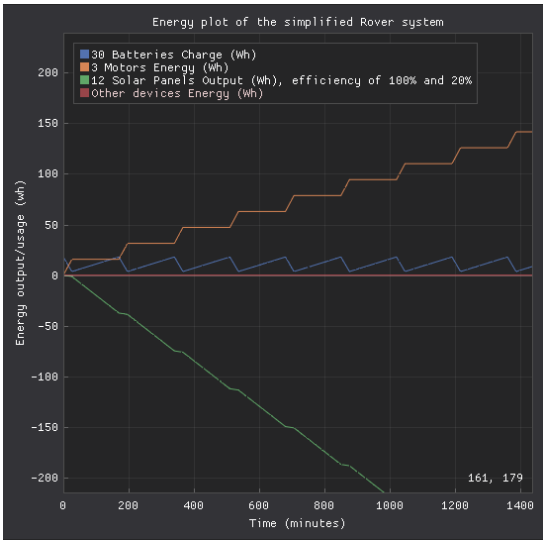

(a)

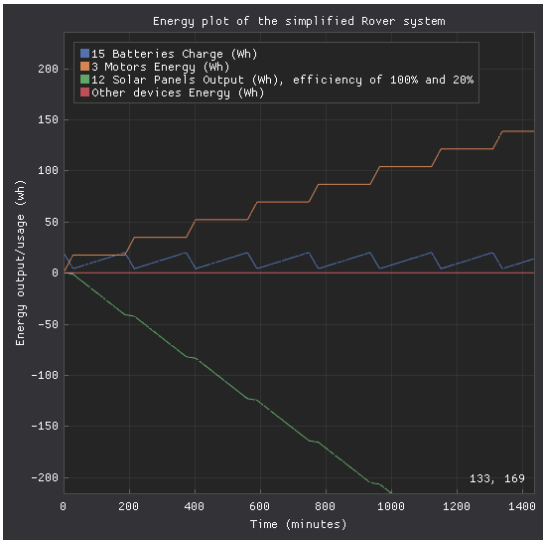

(b)

Figure A.2: (a.) 30 TLI-1530A batteries in the energy budget simulator showing a charge-to-walk ratio of 5.50 minutes to 1 minute. (b.) 15 TLI-1550A batteries in the energy budget simulator showing a charge-to-walk ratio of 5.50 minutes to 1 minute.

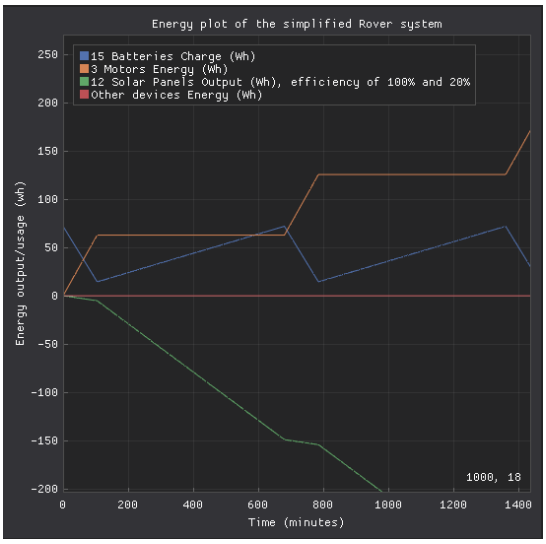

(a)

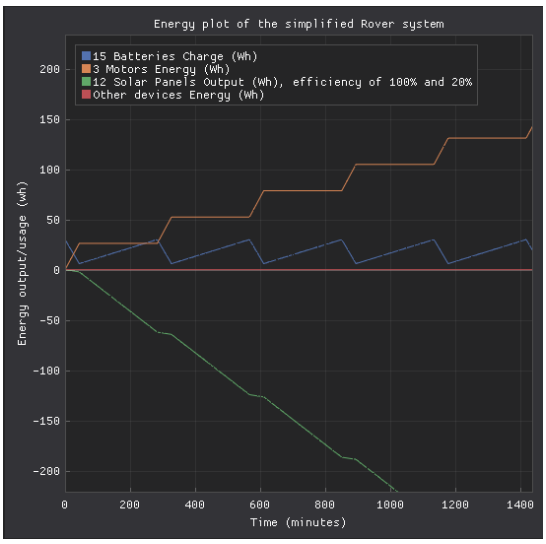

(b)

Figure A.3: a.) 15 TLI-1550ES batteries in the energy budget simulator showing a charge-to-walk ratio of 5.50 minutes to 1 minute. (b.)15 TLI-1550HT batteries in the energy budget simulator showing a charge-to-walk ratio of 5.50 minutes to 1 minute.

A.2 PV Panel

The rover uses predetermined TJ Solar Cell 3G30A panels [2], which have a characteristic IV-curve and a maximum power point (MPP). Typically, a Maximum Power Point Tracker (MPPT) is used to operate at the MPP. as said in section 5.2, this was assumed sufficient for Lunar Zebro, but further analysis showed that a Selective Power Point Tracker (SPPT) would be more appropriate. This topic is discussed in here, as implementing the SPPT is beyond the scope of this thesis.

The datasheet of the TJ Solar Cell 3G30A [2] does not provide a full IV-curve, but instead lists only the minimum and maximum power points. Equation A.1 shows the general behavior of a PV solar cell:

$$I = I_{ph} - I_0 \left[\exp\left(\frac{V + IR_s}{nV_T} \right) - 1 \right] - \frac{V + IR_s}{R_{sh}} \tag{A.1}$$

Where I is the PV array output current (A), V is the PV array output voltage (V), I_{ph} is the photocurrent generated by sunlight (A), I_0 is the diode reverse saturation current (A), R_s is the series resistance (Ω), R_{sh} is the shunt resistance (Ω), n is the diode ideality factor, and V_T is the thermal voltage, given by kT/q, where k is the Boltzmann constant, T is the cell temperature (K), and q is the electron charge.

It is clear that many parameters in this equation are uncertain or unavailable for the chosen panel. However, detailed modelling is not required for developing the MPPT. What matters is the general shape of the IV-curve, and from Equation A.1 it can be seen that the PV panel follows an exponential-like behavior. By fitting a simplified exponential model to the available datasheet points, the overall behavior of the panel can be approximated well enough for MPPT purposes. Equation A.2 shows the simplified model used:

$$I = 2.65 - \exp\left(\frac{V - 0.52}{0.015} \right) \tag{A.2}$$

The simplified model does not attempt to capture every physical effect, but it provides a practical and consistent representation of the panel's expected IV-curve, which is sufficient for MPPT algorithm development. The datapoints from the datasheet of TJ Solar Cell 3G30A [2], the simplified model of the IV curve and the power can be seen in Figure A.4.

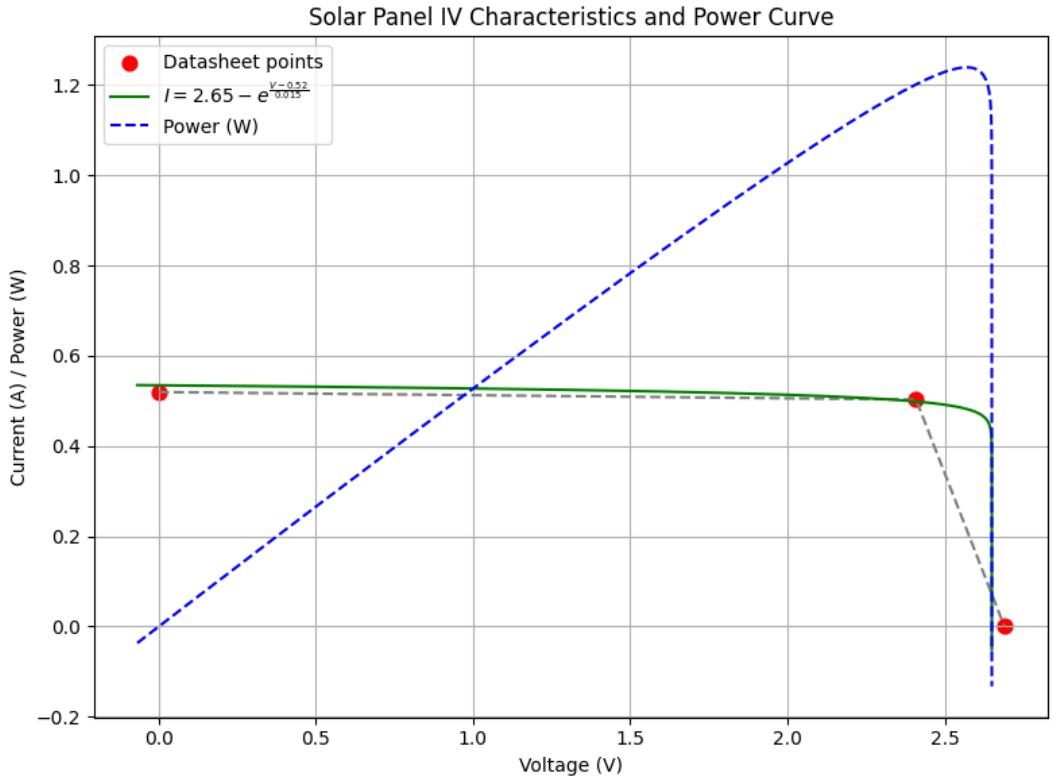

Figure A.4: simplefied IV model to simulate the behaviour of the solar cell

In addition to developing a model for the solar panel, the maximum power point tracking (MPPT) algorithm was further investigated. From here, it was established that for this EPS a Selective power

point tracking (SPPT) algorithm was needed. Figure A.5 shows the altered MPPT algorithm. The added green state makes this algorithm the SPPT.

The need for an SPPT arises from the specific power requirements of the Lunar Zebro rover. In most battery systems, the power delivered by the solar panels is lower than or equal to the maximum charging power of the batteries. In such systems, there is no need to supply less power than the panels can produce.

For Lunar Zebro, the situation is different. Besides charging the batteries, other subsystems also require power. The Tadiran batteries in particular have a low maximum charging current, which limits the charging power to only a small fraction of the total system demand. Therefore, the solar panels must adjust their output to match the instantaneous power required by the system.

If the system demands more power than the panels can provide, the batteries supply the additional energy. Conversely, if the system requires less power than the panels can deliver, the panels must reduce their output accordingly. This selective adjustment is the main function of the SPPT.

During the course of the thesis, it was concluded that a more in-depth analysis and development of the MPPT algorithm would exceed the scope of this work. Therefore, no further development of the solar panel subsystem was pursued, and this aspect is left for future work. The created simulated tool and modeling tool of the panels can be found in the Lunar zebro Git.

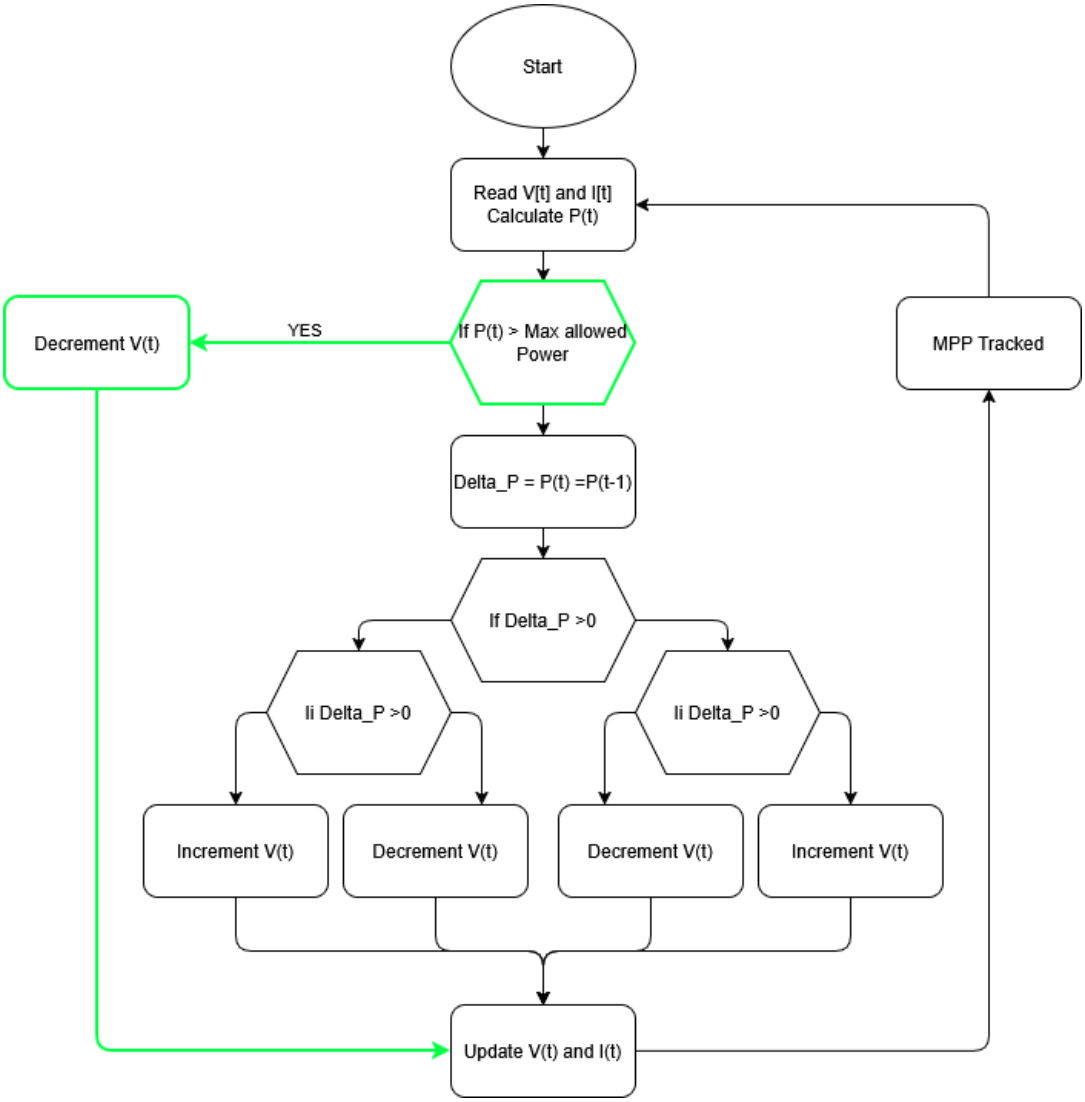

Figure A.5: SPPT algorithm and MPPT algorithm (without the added green state) in state machine, As noted by Katche et al. [10],

Appendix B

Additional Detailed Design

B.1 CRC Checksum Formula Function

As said in subsection 5.1.2 the HAL_CRC_Calculate does not provide the correct CRC byte. The function presented here is used to calculate the CRC that needs to be sent over to the BMS IC.

```
uint8_t BQ76920_CalcCRC(uint8_t reg, uint8_t data)
{
    uint8_t crc = 0x00;
    uint8_t bytes[3] = {BQ76920_ADDR, reg, data }; // device address for write

    for (uint8_t i = 0; i < 3; i++)
    {
        crc ^= bytes[i];
        for (uint8_t b = 0; b < 8; b++)
        {
            if (crc & 0x80)
                crc = (crc << 1) ^ 0x07;
            else
                crc <<= 1;
        }
    }

    return crc;
}
```

B.2 Buck-Boost Mode $V_{\text{bat}} \approx V_{\text{bus}}$

The buck-boost operating mode represents the transition region between pure buck and pure boost operation and occurs when the battery voltage is approximately equal to the bus voltage, i.e., $V_{\text{bat}} \approx V_{\text{bus}}$. In this region, neither a clear step-down nor a clear step-up of the voltage is required. The converter operates by alternately storing and releasing energy in the inductor, while maintaining an approximately equal voltage level on both sides.

As said in subsection 5.3.1, in the context of the rover EPS, this operating mode is generally not required. When V_{bat} and V_{bus} are equal, there is no need for voltage conversion and direct power from the solar panels would be sufficient. Another reason is that the BMS will already have shut off the cells when the battery pack is near 12 V, which directly changes the behavior of the converter to boost mode, because that needs to be prevented. If there is no possibility to boost, the rover will shut off until it is possible to boost. Using the converter in this state would introduce energy losses and reduce overall efficiency. Therefore, when both voltage levels are sufficiently close, the bidirectional converter can be disabled and the battery can be disconnected from the bus.

However, the buck-boost region is relevant from a control and stability perspective. During transient conditions, such as load changes or voltage fluctuations, the converter may operate in buck-boost mode, ensuring stable behavior.

Appendix C

Pitfalls and Warnings

In this chapter, some pitfalls and warnings encountered during the thesis are discussed so that in the future, these can be prevented.

C.1 Battery Short

One avoidable issue in this design is the placement of the battery terminals. Figure C.1 shows a burn mark on the BAT5+ terminal. These terminals are intended to connect cells that do not fit in the PCB battery holders and are linked to the holder terminals. Each battery has a thin metallic strip soldered on top. If a cell is inserted incorrectly, this strip can touch the terminal, causing a short circuit, as happened briefly with cell 5 and left the burn mark. In future designs, it is recommended to reposition these terminals to prevent such accidents.

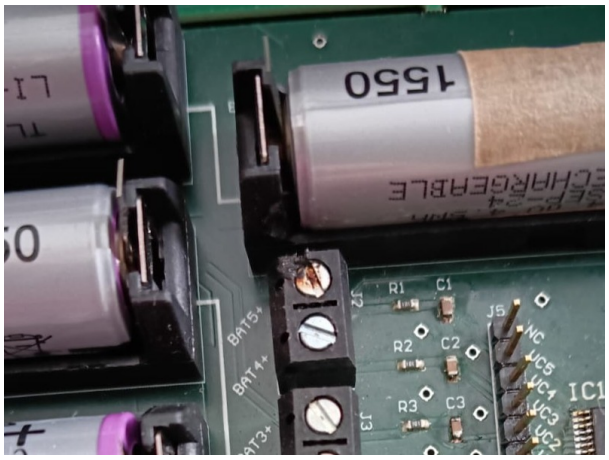

Figure C.1: Burn mark at terminal BAT5+ from metallic strip of the battery.

C.2 Bleeding Algorithm

In Subsection 5.1.3, the final bleeding algorithm is discussed. This section describes the earlier, incorrect version of the algorithm, shown in Figure C.2. This is shown because in the datasheet of the BQ76920 [7] it is vaguely described how to create this bleeding algorithm. This is done so that every developer has the freedom to implement their own algorithm. But to prevent future team members from falling into this pitfall, the wrongly designed algorithm is shown here.

In this algorithm, the voltage of each cell is measured. A cell starts bleeding when its voltage exceeds 3.95 V and differs by more than 20 mV from the lowest cell voltage in the pack. This is similar to

the final algorithm shown in Figure 5.2. The main difference is that this version does not check whether the BMS is in charging mode.

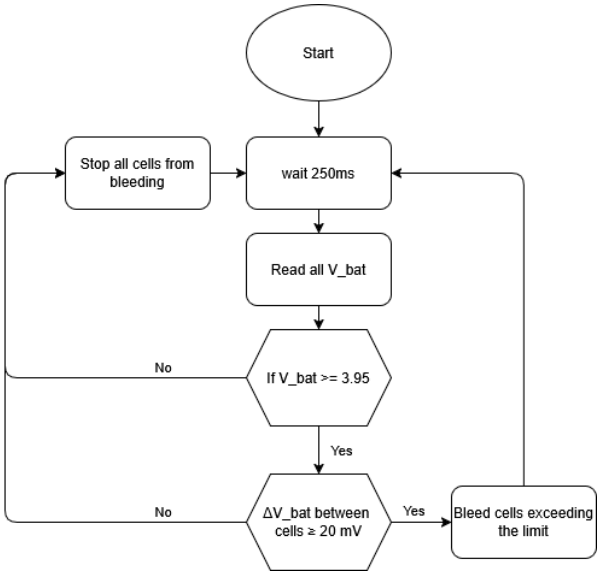

Figure C.2: First Bleeding algorithm, with the pitfall of bleeding cells without the BMS charging.

During initial testing, this was not an issue. The board was only active during charging tests and was turned off afterwards. In a realistic scenario, however, the system continuously switches between charging and discharging. Therefore, the charging state must be taken into account.

Figure C.3 illustrates this issue. The figure shows a zoomed-in section of a charging curve. The algorithm is active, which can be seen from the voltage dips of higher-voltage cells. However, cells 3 and 5 consistently show a lower voltage. This occurs because the bleeding algorithm remains active while the BMS is idle. As a result, these cells are discharged further when they should not be. To prevent this, in the upgraded algorithm bleeding is enabled only when the BMS is in charging mode.

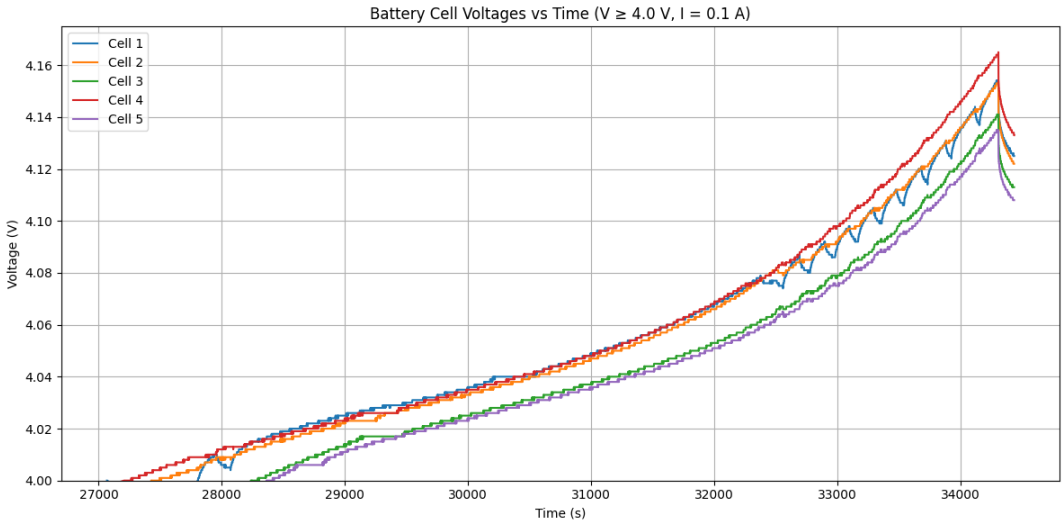

Figure C.3: Here we can see the first bleeding algorithm, which did not work correctly.

Appendix D

Additional Results

In this chapter, various additional results are presented. Some of these originate from tests that were conducted incorrectly. While these results do not directly contribute to the research questions of this thesis, they may prove useful for future work and are therefore included in the appendix. Other results are supplementary; although they do not influence the conclusions drawn in the main results chapter, they are included to provide a more complete overview of the data.

D.0.1 Digital load test, RSNS bit Misread, OCD/SCD false positive

In this section additional results are shown on how the *OCD fault* and *SCD fault* flags are raised. In Subsection 7.2.4 and 7.2.5 the results of the original test can be seen. During the initial tests, a fully charged battery pack was connected to the digital load through the BMS. When an output current of 5 A was applied for the first time, SCD and OCD faults were immediately triggered. The BMS reported a short-circuit condition as soon as the load was enabled.

Initially, it was assumed that the activation of the load caused an inrush current, resulting in a current peak that exceeded the configured delay time of 20 ms. However, further investigation using an oscilloscope showed that this was not the case. No significant current peak was observed during load activation.

After debugging it was discovered that bit 7 of the `PROTECT1` (0x06) register was not configured correctly. This bit was set to `0` instead of `1`. As a result, the effective OCD and SCD voltage thresholds were halved, causing the protection mechanisms to trigger at lower currents than intended.

The following output shows the data received via the UART interface. The first five values correspond to the individual cell voltages, followed by the measured current and the cell bleeding status represented in hexadecimal format. It can be observed that the SCD protection is triggered first.

```
1  4.040 V, 4.047 V, 4.036 V, 4.035 V, 4.038 V, -0.001 A, 00
2  System Status (0x00): 0x80
3  System CTRL1 (0x04): 0x10
4  System CTRL2 (0x05): 0x42
5  4.040 V, 4.047 V, 4.036 V, 4.035 V, 4.038 V, -0.003 A, 00
6  System Status (0x00): 0x80
7  System CTRL1 (0x04): 0x10
8  System CTRL2 (0x05): 0x42
9  4.040 V, 4.047 V, 4.036 V, 4.035 V, 4.038 V, -0.000 A, 00
10 System Status (0x00): 0x80
11 System CTRL1 (0x04): 0x10
12 System CTRL2 (0x05): 0x42
13 4.040 V, 4.047 V, 4.036 V, 4.035 V, 4.038 V, -0.001 A, 00
14 System Status (0x00): 0x80
```

```
System CTRL1 (0x04): 0x10
System CTRL2 (0x05): 0x42
4.040 V, 4.047 V, 4.036 V, 4.035 V, 4.038 V, -0.000 A, 00
System Status (0x00): 0x80
System CTRL1 (0x04): 0x10
System CTRL2 (0x05): 0x42
4.040 V, 4.047 V, 4.036 V, 4.035 V, 4.038 V, 0.003 A, 00
System Status (0x00): 0x82
SCD fault
System CTRL1 (0x04): 0x90
System CTRL2 (0x05): 0x40
4.040 V, 4.047 V, 4.035 V, 4.035 V, 4.038 V, 0.001 A, 00
```

After correcting the SCD threshold to 9.58 A, it was observed that the OCD protection was triggered instead, as shown in the UART output below. Once this configuration error was resolved, the digital load could be used without further issues. Following this fix, the SCD and OCD protections were tested individually, as described in Subsection 7.2.5. This issue in the firmware also demonstrated that the test setup is capable of reliably triggering the protection mechanisms at lower current thresholds.

```
3.965 V, 3.970 V, 3.965 V, 3.962 V, 3.968 V, -0.001 A, 00
System Status (0x00): 0x80
System CTRL1 (0x04): 0x10
System CTRL2 (0x05): 0x42
3.965 V, 3.971 V, 3.965 V, 3.962 V, 3.968 V, -0.000 A, 00
System Status (0x00): 0x80
System CTRL1 (0x04): 0x10
System CTRL2 (0x05): 0x42
3.965 V, 3.971 V, 3.965 V, 3.962 V, 3.968 V, -0.005 A, 00
System Status (0x00): 0x80
System CTRL1 (0x04): 0x10
System CTRL2 (0x05): 0x42
3.965 V, 3.971 V, 3.965 V, 3.962 V, 3.968 V, -0.007 A, 00
System Status (0x00): 0x80
System CTRL1 (0x04): 0x10
System CTRL2 (0x05): 0x42
3.965 V, 3.971 V, 3.965 V, 3.962 V, 3.968 V, -0.003 A, 00
System Status (0x00): 0x80
System CTRL1 (0x04): 0x10
System CTRL2 (0x05): 0x42
3.965 V, 3.970 V, 3.965 V, 3.962 V, 3.671 V, -0.185 A, 00
System Status (0x00): 0x81
OCD fault
System CTRL1 (0x04): 0x90
System CTRL2 (0x05): 0x40
3.965 V, 3.970 V, 3.965 V, 3.962 V, 3.967 V, -0.003 A, 00
```

D.0.2 Cell Balancing

Discharge Curves of Battery pack Charged With Bleeding Algorithm.

In Subsection 7.2.6 it is shown what the influence of the bleeding algorithm is on charging the battery pack via the BMS. Figure D.1 and Figure D.2 show the discharge curves after the battery pack is charged. For now no further conclusions can be taken from these plots, but for completeness these figures are shown here in the Appendix.

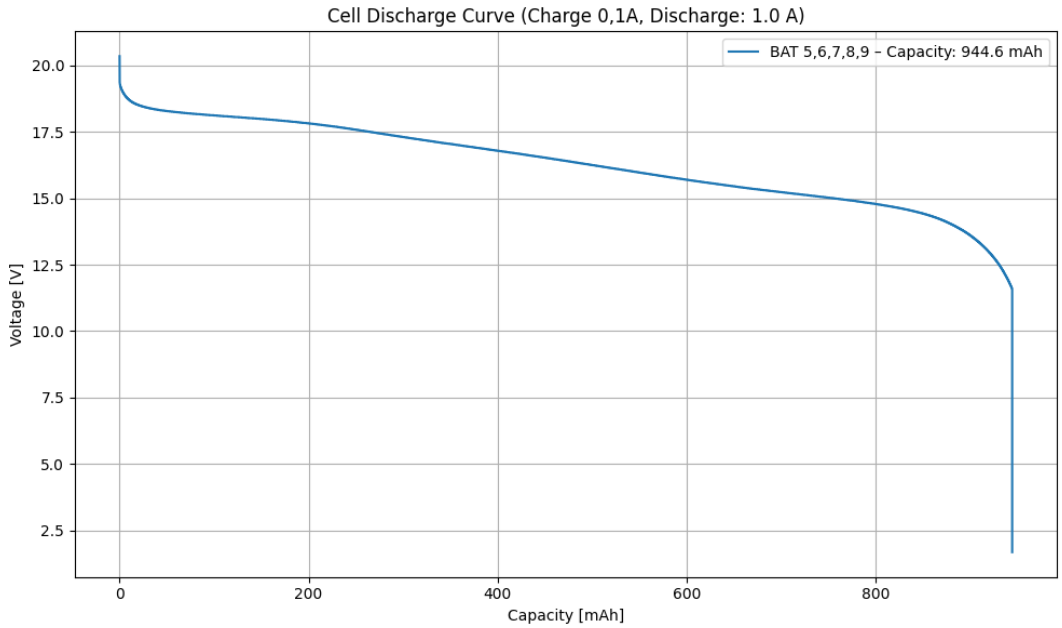

Figure D.1: Discharge curve of the whole battery pack, after being charged with the cell balancing algorithm.

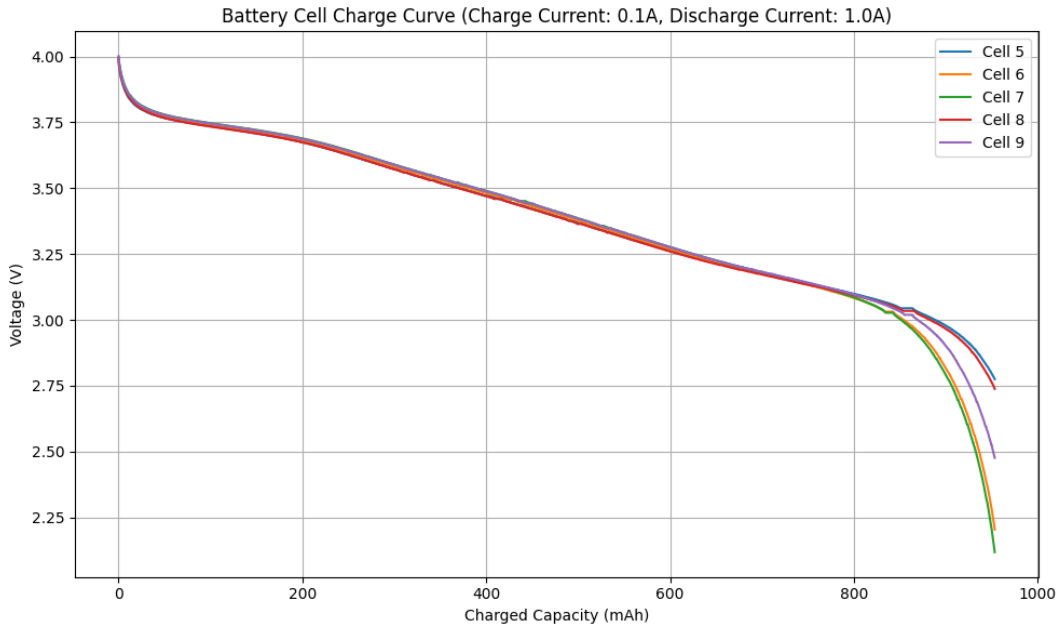

Figure D.2: Discharge curve of the individual cells of the battery pack, after being charged with the cell balancing algorithm.

Discharge Curves of Battery Pack Charged Without Bleeding Algorithm.

Subsection 7.2.6 illustrates the effect of the bleeding algorithm on charging the battery pack via the BMS. Figures D.3 and D.4 present the corresponding discharge curves after charging. While no additional conclusions can be drawn from these plots at this stage, they are included here in the Appendix for completeness.

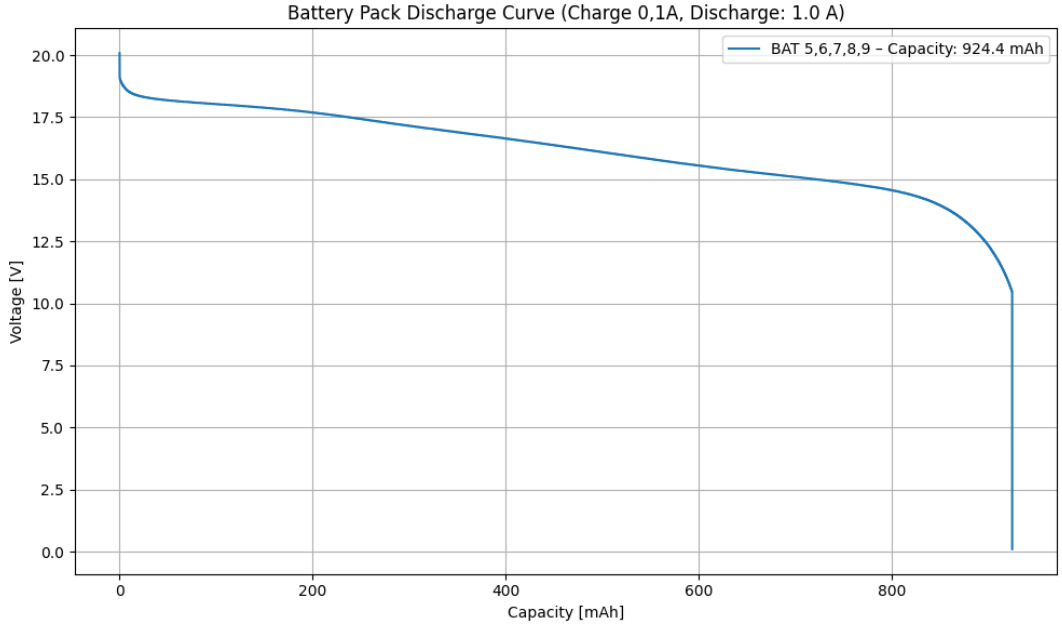

Figure D.3: Discharge curve of the whole battery pack, after being charged without the cell balancing algorithm.

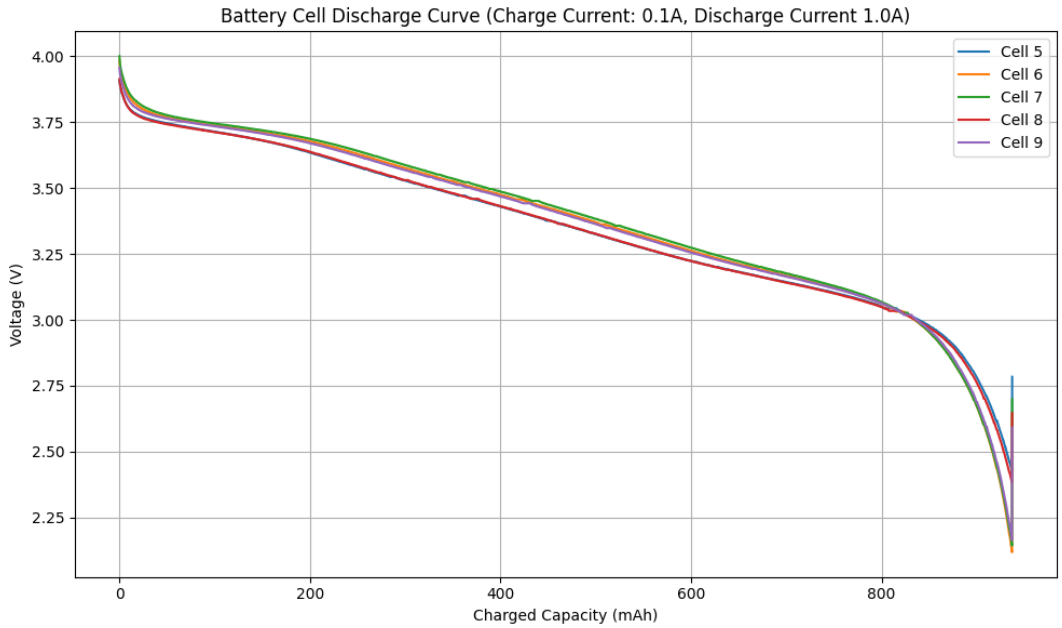

Figure D.4: Discharge curve of the individual cells of the battery pack, after being charged without the cell balancing algorithm.

D.0.3 Endurance Test Results (Tabulated Data)

Figure 7.3 shows the plot of the discharge cycles of the cell that is used for the capacity endurance test. This figure shows the degradation of SOH over several discharge cycles. In the Table D.1, the degradation of the SOH per run can be seen.

Test	**Capacity (mAh)**	**SOH (%)**
1	1008.44	100.00
2	989.86	98.16
3	967.62	95.95
4	958.02	95.00
5	950.18	94.22
6	939.31	93.14
7	925.09	91.73
8	924.14	91.64
9	916.76	90.91
10	908.50	90.09
11	901.19	89.36
12	892.10	88.46
13	881.59	87.42
14	880.17	87.28
15	866.71	85.95
16	864.83	85.76
17	857.44	85.03
18	855.87	84.87
19	846.44	83.94
20	842.30	83.53
21	830.75	82.38
22	823.03	81.61
23	807.88	80.11
24	809.04	80.23
25	806.96	80.02

Table D.1: Endurance Test Results Corresponding to Figure 7.3

Appendix E

PCB

E.1 BMS

In this section, the schematics of the BMS PCB can be seen. The PCB is manufactured in Subsection 5.5.1. The naming in the schematic corresponds with the naming of the components on the board. This schematic can be seen in the Altium git of the Lunar Zebro team and is added for completeness to this thesis.

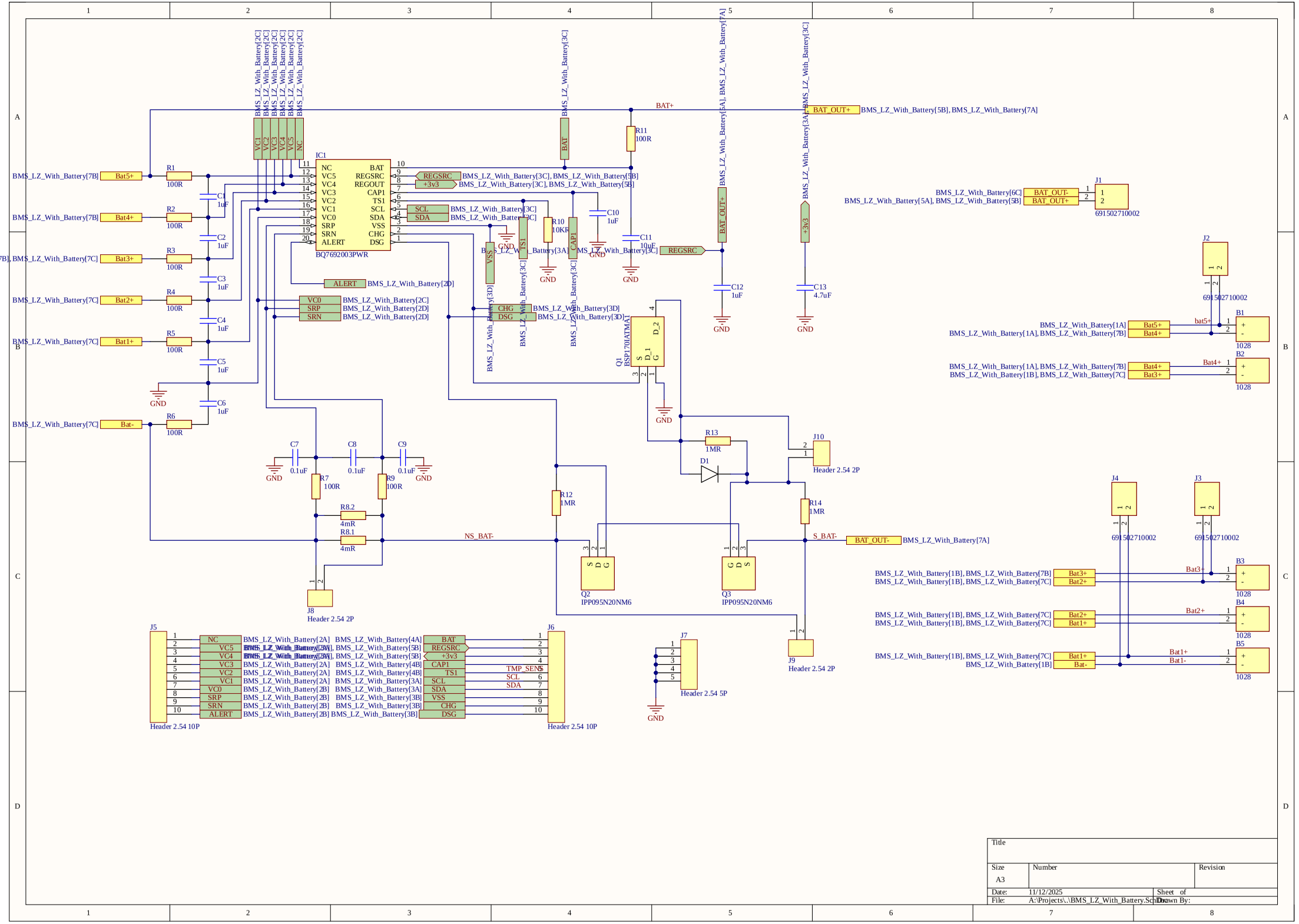
IC1
BQ7692003PWR
NC
VC5
VC4
VC3
VC2
VC1
VC0
SRP
SRN
ALERT
BAT
REGSRC
REGOUT
CAP1
TS1
SCL
SDA
VSS
CHG
DSG
BAT+
BAT_OUT+
BMS_LZ_With_Battery[5B], BMS_LZ_With_Battery[7A]
R11 100R
R1 100R
R2 100R
R3 100R
R4 100R
R5 100R
R6 100R
C1 1uF
C2 1uF
C3 1uF
C4 1uF
C5 1uF
C6 1uF
Bat5+
Bat4+
Bat3+
Bat2+
Bat1+
Bat-
GND
C7 0.1uF
C8 0.1uF
C9 0.1uF
R7 100R
R9 100R
R8.2 4mR
R8.1 4mR
NS_BAT-
R10 10KR
C10 1uF
C11 10uF
C12 1uF
C13 4.7uF
+3v3
REGSRC
ALERT
R12 1MR
R13 1MR
R14 1MR
D1
Q1 BSP170ATMA1
Q2 IPP095N20NM6
Q3 IPP095N20NM6
S_BAT-
BAT_OUT-
BMS_LZ_With_Battery[7A]
J1
691502710002
J2
691502710002
J3
691502710002
J4
691502710002
J8 Header 2.54 2P
J9 Header 2.54 2P
J10 Header 2.54 2P
J5 Header 2.54 10P
J6 Header 2.54 10P
J7 Header 2.54 5P
B1 1028
B2 1028
B3 1028
B4 1028
B5 1028
TMP_SENS
SCL
SDA
Title
Size A3
Number
Revision
Date: 11/12/2025
Sheet of
File: A:\Projects\..\BMS_LZ_With_Battery.SchDoc
Drawn By:

E.2 Bidirectional converter

In this section, the schematics of the bidirectional converter PCB can be seen. The PCB is manufactured in Subsection 5.5.2. The naming in the schematic corresponds with the naming of the components on the board. The first page is the top level schematic, followed by the bidirectional convert design and finished with the 5v converter startup circuit. This schematic can be seen in the Altium git of the Lunar Zebro team and is added for completeness to this thesis.

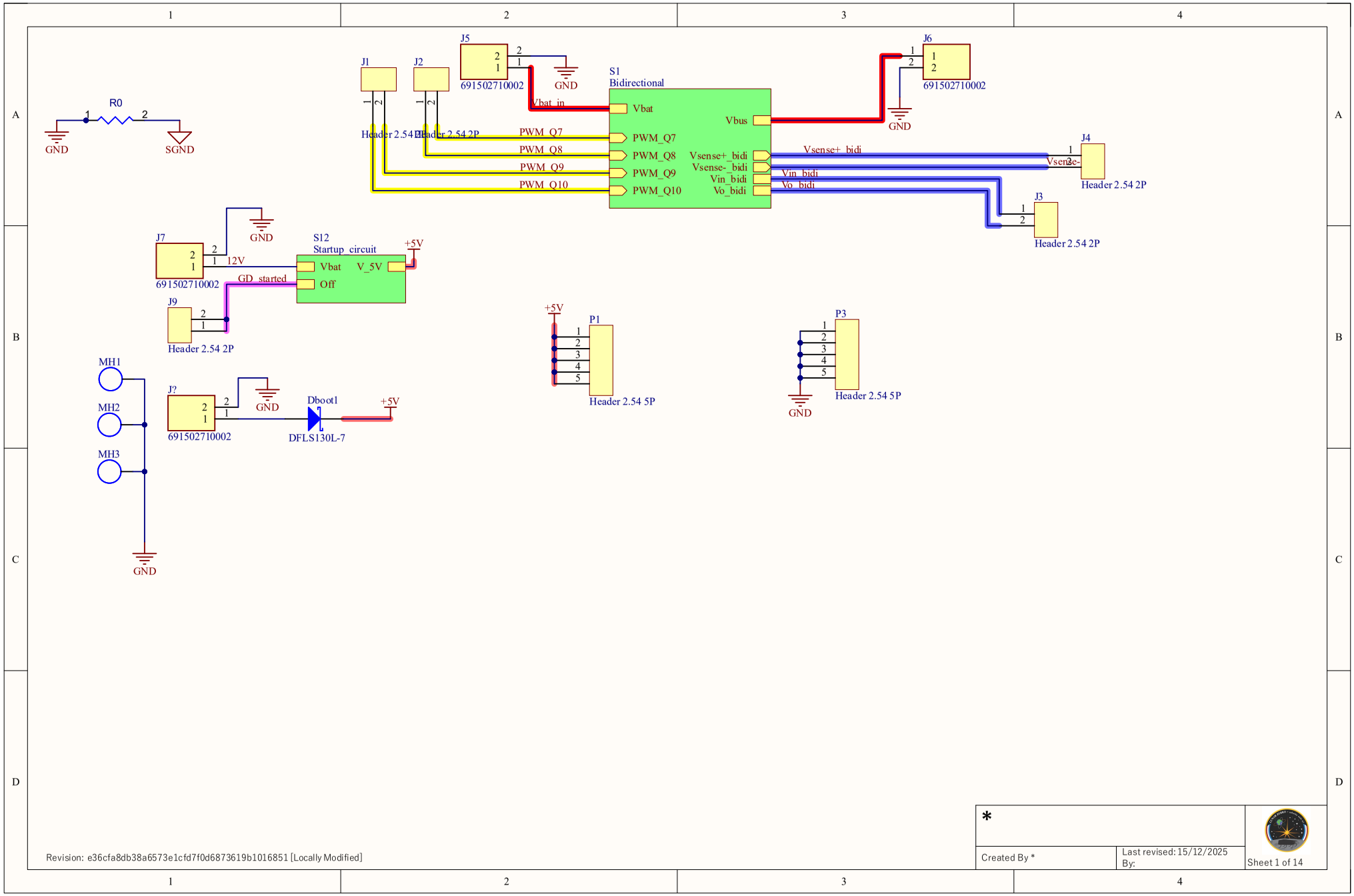

Revision: e36cfa8db38a6573e1cfd7f0d6873619b1016851 [Locally Modified]

*		
Created By *	Last revised: 15/12/2025 By:	Sheet 1 of 14

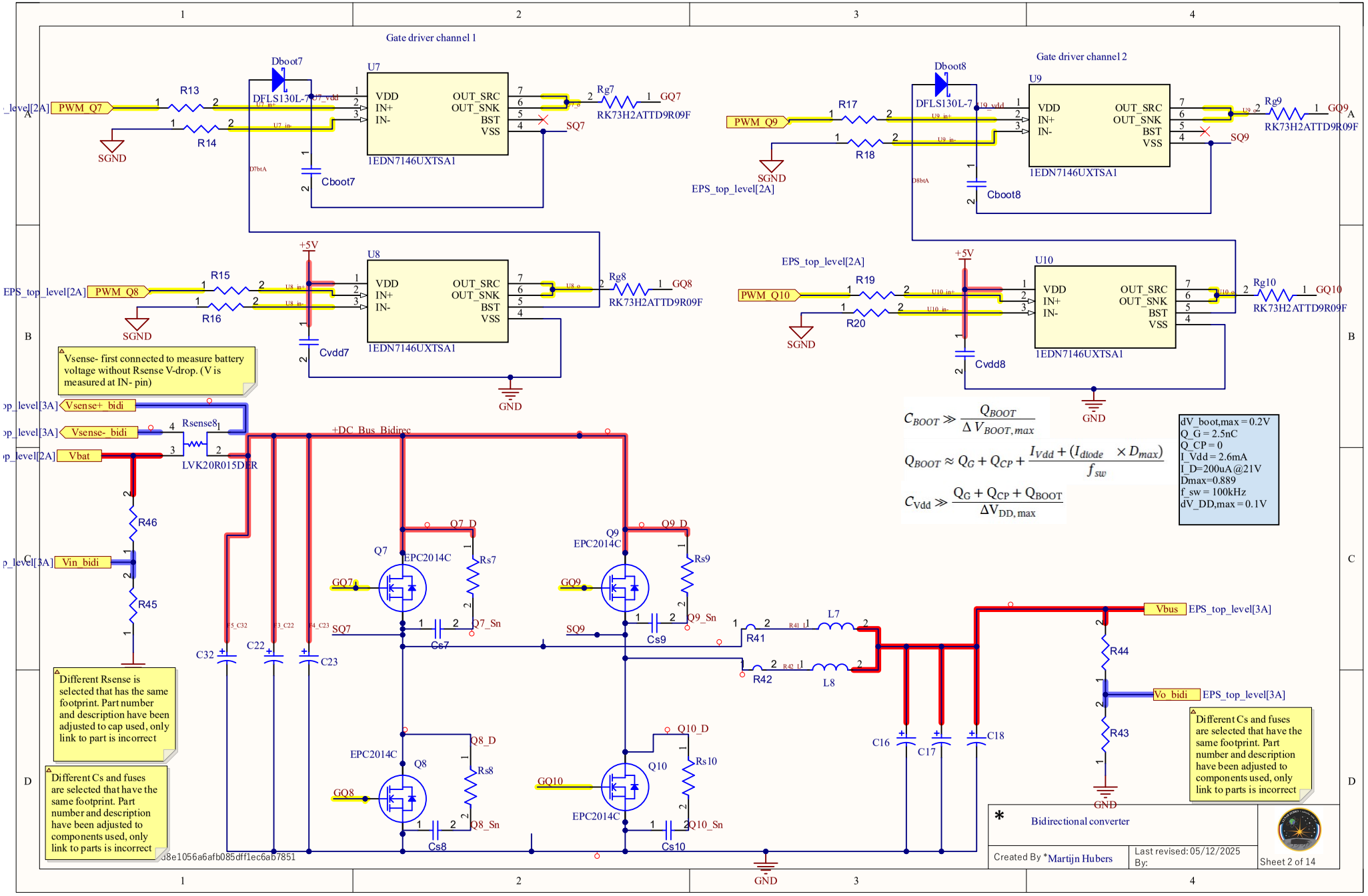
Gate driver channel 1
Gate driver channel 2
PWM_Q7
PWM_Q8
PWM_Q9
PWM_Q10
R13
R14
R15
R16
R17
R18
R19
R20
Dboot7
Dboot8
DFLS130L-7
U7
U8
U9
U10
VDD
IN+
IN-
OUT_SRC
OUT_SNK
BST
VSS
1EDN7146UXTSA1
Cboot7
Cboot8
Cvdd7
Cvdd8
+5V
SGND
GND
Rg7
Rg8
Rg9
Rg10
RK73H2ATTD9R09F
GQ7
GQ8
GQ9
GQ10
SQ7
SQ9
EPS_top_level[2A]
Vsense- first connected to measure battery voltage without Rsense V-drop. (V is measured at IN- pin)
Vsense+_bidi
Vsense-_bidi
Vbat
Vin_bidi
Rsense8
LVK20R015DER
R46
R45
+DC_Bus_Bidirec
Q7
Q8
Q9
Q10
EPC2014C
Q7_D
Q8_D
Q9_D
Q10_D
Rs7
Rs8
Rs9
Rs10
Q7_Sn
Q8_Sn
Q9_Sn
Q10_Sn
Cs7
Cs8
Cs9
Cs10
C32
C22
C23
L7
L8
R41
R42
C16
C17
C18
Vbus
EPS_top_level[3A]
R44
R43
Vo_bidi
Different Rsense is selected that has the same footprint. Part number and description have been adjusted to cap used, only link to part is incorrect
Different Cs and fuses are selected that have the same footprint. Part number and description have been adjusted to components used, only link to parts is incorrect
Different Cs and fuses are selected that have the same footprint. Part number and description have been adjusted to components used, only link to parts is incorrect
$C_{BOOT} \gg \frac{Q_{BOOT}}{\Delta V_{BOOT,max}}$
$Q_{BOOT} \approx Q_G + Q_{CP} + \frac{I_{Vdd} + (I_{diode} \times D_{max})}{f_{sw}}$
$C_{Vdd} \gg \frac{Q_G + Q_{CP} + Q_{BOOT}}{\Delta V_{DD,max}}$
dV_boot,max = 0.2V
Q_G = 2.5nC
Q_CP = 0
I_Vdd = 2.6mA
I_D=200uA@21V
Dmax=0.889
f_sw = 100kHz
dV_DD,max = 0.1V
* Bidirectional converter
Created By *Martijn Hubers
Last revised: 05/12/2025
By:
Sheet 2 of 14

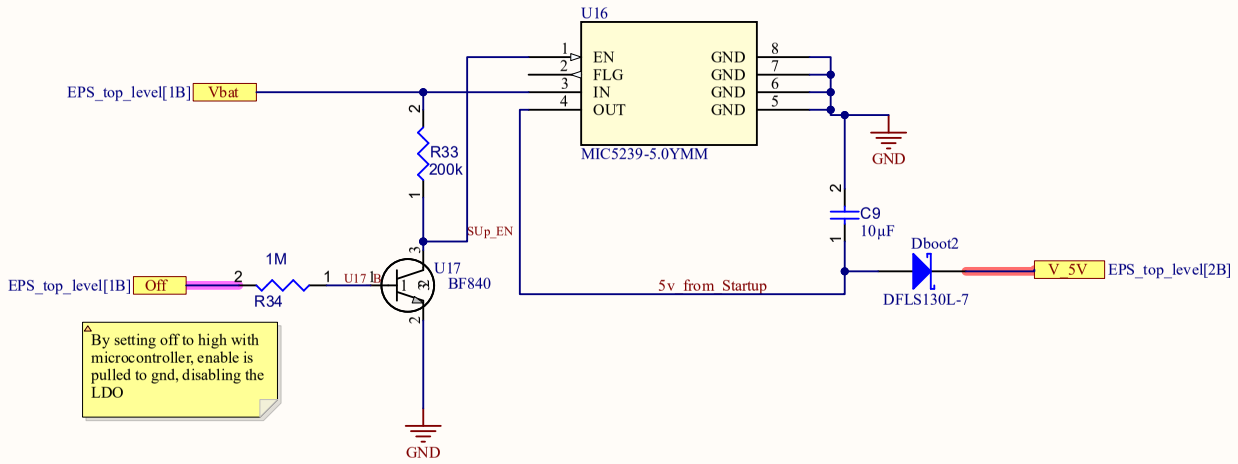

Revision: 8952a44e0292ae6e1f8520f1a9a70983e308defb [Locally Modified]

*		
Created By *	Last revised: 15/12/2025 By:	Sheet 3 of 14